Alma Mater Studiorum – Università di Bologna

DOTTORATO DI RICERCA IN

DATA SCIENCE AND COMPUTATION

Ciclo 35

Settore Concorsuale: 03/D1 – CHIMICA E TECNOLOGIE FARMACEUTICHE, TOSSICOLOGICHE, E NUTRACEUTICO – ALIMENTARI

Settore Scientifico Disciplinare: CHIM/08 – CHIMICA FARMACEUTICA

EXPLOITING MOLECULAR SIMULATIONS AS AN ATOMIC-LEVEL MICROSCOPE TO ELUCIDATE CLINICALLY RELEVANT CATION CHLORIDE COTRANSPORTERS

Presentata da: Manuel José Ruiz Munevar

Coordinatore Dottorato

Daniele Bonacorsi

Supervisore

Marco De Vivo

Advisor

Andrea Cavalli

Esame Finale Anno 2024

Table of Contents

Acknowledgements

First and foremost, I owe a profound debt of gratitude to my parents. Your unwavering support and encouragement have been the bedrock upon which I built my aspirations. Without you, this journey would not have been possible. Gracias infinitas!

To Marco De Vivo and Pietro Vidossich, your invaluable guidance and enlightening discussions have been instrumental in shaping my PhD journey. I am deeply appreciative of the opportunities and insights you've shared with me, making the challenges more surmountable.

To my dear friends Sebastian, Ziggy, Uma, Jacopo, David, Maria Antonietta, Adam, Joe, and Gianfranco: your company and support have transformed this academic pursuit into a memorable adventure. Living in the Italian Riviera was made all the more enriching thanks to each one of you. You've amplified the joys and cushioned the setbacks, and for that, I am eternally grateful.

Lastly, Janna, words cannot capture the depth of my gratitude. Your unwavering support has been nothing short of extraordinary. Given the chance to relive this journey, I would choose this path with you by my side, time and time again.

Preface

Before we formally begin, I would like to give you a bit of an overview of the document you are about to read, along with adding a bit of context to how it came to be. This story started during my studies for my B.Sc. in Microbiology at the Universidad de los Andes in Bogotá, Colombia, back in 2016. That year, I was taking two courses, Evolution and Fundamentals of Physical Chemistry, that put me on the path that led here, to a Ph.D. in Data Science and Computation focused on computational chemistry at the Alma Mater Studiorum - Università di Bologna.

In fact, it was a period of two weeks that defined the following eight years of my life, up to today. The first step in this chain of events was a recommended reading from Evolution's Prof. Daniel Cadena. In short, it was a historical review on the evolutionary arm's race between newts and snakes[1]. Newts produce and excrete tetrodotoxin (TTX, a powerful neurotoxin – also found in fugu fish, making it a peculiarly dangerous delicacy) on their skin, whereas snakes feed on newts. The snakes will then become poisoned and die due to TTX's paralytical effect. Well, most snakes will die. A few would have mutations that rendered them resistant to the toxin's effect, leading to a population of snakes unaffected by TTX. Then, most newts would be eaten, except for those with mutations that led to higher TTX toxicity; and the arm's race begins! This is of course an extremely simplified account of an extremely complex topic that spans hundreds of publications. In the last handful of pages of this historical review they explain TTX's mechanism of action, and it blew my mind. TTX acts like a cork to sodium channels and blocks sodium from being transported through the membrane, a phenomenon that is essential for signal transmission from the brain to the rest of the body. Without functioning sodium transport muscles become paralyzed.

The second step also took place in the Evolution course. We were asked to pick a phenotypical trait and then argue if it was either an adaptation or an exaptation, through a short presentation. As a microbiologist, who also felt that proving that a trait was an exaptation was significantly more difficult, I decided to talk about bacterial antibiotic resistance – a clear adaptation (in most cases). That same week, the Guardian had published an article about super-gonorrhea[2] – gonorrhea presenting high levels of resistance to multiple antibiotics, which could then potentially leave an infected person with an incurable disease. The stage was set! The presentation would be on gonorrhea's antibiotic resistance. Whilst preparing the presentation, I ran into a tidbit of information that would change my life – at that time completely unbeknownst to me. It turns out, gonorrhea resists antibiotics due to the

overexpression of the efflux pump MtrCDE[3]. This efflux pump would simply extrude the antibiotic from gonorrhea's periplasm, never letting the drug into the cytoplasm to carry out its mission.

These two chunks of information sparked an idea in my mind that would torment me for the next 2 years. If TTX is able to bind to a sodium channel, blocking sodium's passage, surely there must be some molecule that could potentially block gonorrhea's efflux pump eliminating its antibiotic resistance mechanism, and turning an incurable disease into an easily treatable sexually transmitted infection. But how could someone go about finding such a molecule with such a specific function? Where would a second year Microbiology student even start?

We have arrived to the last step, in this meaningful two week-long chain of events. During the second week, Prof. Gian Pietro Miscione decided to cancel a Fundamentals of Physical Chemistry lesson, and instead invited a student from his research group COBO – Computational Bio-Organic Chemistry, to tell us about the research that they were conducting. My mind was blown, but in a significantly grander magnitude than ever before. The now Dr. Sebastian Franco Ulloa, then an undergraduate student of Physics and Chemistry, gave us a talk about molecular dynamics and virtual screening. In few words, a technology that allowed us to simulate proteins at the atomic level, to better observe and understand the nature around us, which to me sounded like something out of science fiction. I could not believe this technology existed. Also, virtual screening? My god. It made so much sense. Understanding the 3D structure of a pharmaceutical target, and their motions, would allow for a rationally designed molecule to perfectly bind to its target and completely inhibit it. The solution to the idea I had the previous week had been placed right in front of me in a silver platter. I could use computational chemistry to find an inhibitor to gonorrhea's efflux pump and rid the world of super-gonorrhea!

After Sebastian's talk I went straight to Prof. Gian Pietro Miscione and asked if we could meet and discuss my idea. In the end, I ended up doing my thesis under his guidance: "Computational search for inhibitors of the efflux pump MtrCDE from *Neisseria gonorrhoeae*". During the development of this work, I met Dr. Marco de Vivo in a conference in Bogotá. We had some interesting discussions, after which he suggested I apply for a Ph.D. position in his research group at the Italian Istitute of Technology, and now here we are, seven years later. With me sitting here, having the privilege of writing a Ph.D. thesis on computational chemistry sitting at the Italian riviera, on a topic I have been in love and in sheer awe of. A topic that still somehow feels like science fiction to me.

I have the honor of presenting the research work I have been carrying out for the past four years, under Dr. Marco de Vivo's tutelage, in the Molecular Modeling and Drug Discovery research group. We have focused our efforts on investigating ion transporters associated with serious and relevant neuropathologies through computational methods. In Chapter 1 we will give a biological overview of cation chloride cotransporters (CCC), with a focus on NKCC1. In Chapter 2, we will give an overview of the main computational tools that we used as a magnifying glass to elucidate the function of members from the CCC family. Chapter 3 will show our findings and novel understanding of specific features of the CCC member KCC1. Chapter 4 represents our greatest achievement, which is a comprehensive research project that encompasses the use of several state-of-the-art computational techniques, that helped us elucidate the transport mechanism of CCC member NKCC1, along with several other previously unknown or not fully understood functional features. To close, Chapter 5 will conclude this work with some final remarks.

Thank you for joining me in this adventure!

Abstract

The cation chloride cotransporters (CCCs) represent a vital family of ion transporters, with several members implicated in significant neurological disorders. Specifically, conditions such as cerebrospinal fluid accumulation, epilepsy, Down's syndrome, Asperger's syndrome, and certain cancers have been attributed to various CCCs. This thesis delves into these pharmacological targets using advanced computational methodologies. I primarily employed GPU-accelerated all-atom molecular dynamics simulations, deep learning-based collective variables, enhanced sampling methods, and custom Python scripts for comprehensive simulation analyses. Our research predominantly centered on KCC1 and NKCC1 transporters. For KCC1, I examined its equilibrium dynamics in the presence/absence of an inhibitor and assessed the functional implications of different ion loading states. In contrast, our work on NKCC1 revealed its unique alternating access mechanism, termed the rocking-bundle mechanism. I identified a previously unobserved occluded state and demonstrated the transporter's potential for water permeability under specific conditions. Furthermore, I confirmed the actual water flow through its permeable states. In essence, this thesis leverages cutting-edge computational techniques to deepen our understanding of the CCCs, a family of ion transporters with profound clinical significance.

Chapter 1:

An overview of cation chloride cotransporters

1.1. Cation-coupled chloride cotransporters: from structure to function and modulation

Cation-chloride cotransporters (CCCs) are proteins (~130 kDa) of the subfamily of solute carrier transporters 12 that modulate transport of sodium and/or potassium cations (Na^+, K^+) and chloride anions (Cl-) across the cell membrane (**Figure 1.A**). In humans, there are seven known electroneutral CCCs: the Na^+- Cl^- cotransporter NCC, the Na^+-K^+-Cl^- cotransporters NKCC1 and NKCC2, and the K^+-Cl^- cotransporters KCC1, KCC2, KCC3, and KCC4 (**Figure 1.B**)[4]. NCC and NKCC2 are expressed predominantly in the kidney[5]. NKCC1, KCC1, KCC3, and KCC4 are expressed throughout the body. KCC2 is expressed specifically in neurons[6]. CCCs are involved in physiological processes including salt absorption and secretion, cell volume regulation, and intracellular Cl- concentration setting[4,7]. As such, CCCs are primarily implicated in blood pressure regulation, cardiovascular and brain physiopathology, and diuresis, and are also associated with hearing and tumoral diseases (**Figure 1.C, D**).

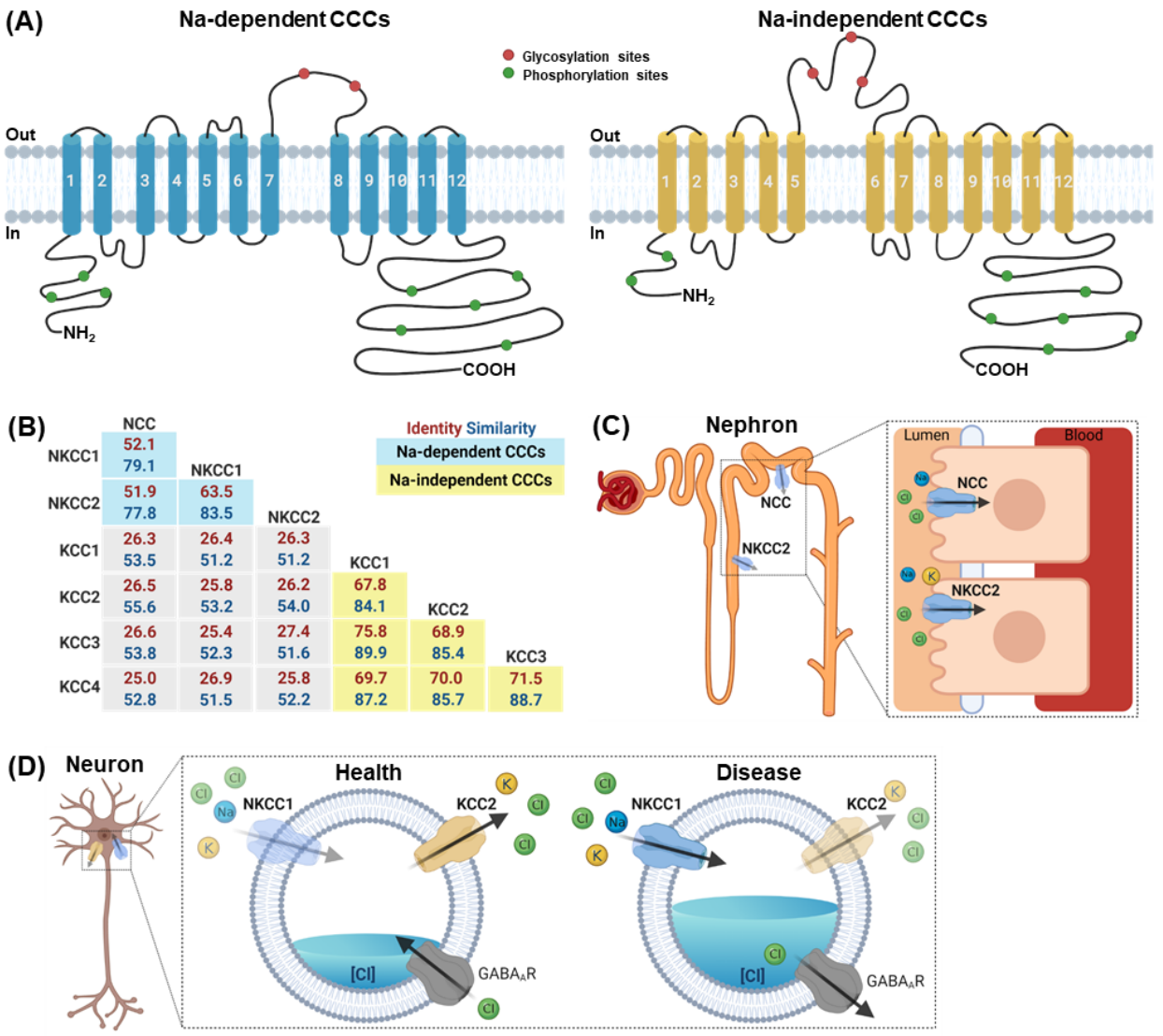

Figure 1. CCC structures and functions. **(A)** Schematic representation of CCC topology based on LeuT homology amino acid sequence alignments and structural studies. CCCs are characterized by 12 helices in the TM domain and a large extracellular (EC) domain. The EC domain is formed mainly by a large loop between TM7 and TM8 for Na^+-dependent CCCs, and TM5 and TM6 for Na^+-independent CCCs. An N-terminal (NT) domain and a large C-terminal (CT) domain are located intracellularly for all CCCs. Within the extra and intra cellular domains, there are key residues that can modulate the activity of the transporter via phosphorylation (green dots) or glycosylation (red dots). **(B)** Homologies (expressed as percentage of identity – residues that match between two protein amino acid sequences, and similarity – residues with similar physico-chemical properties) among the protein amino-acid sequences of human Na^+-dependent CCCs (NCC isoform 1, NKCC1 isoform 1, NKCC2 isoform a) and human Na^+-independent CCCs (KCC1 isoform 1, KCC2 isoform 1 or a, KCC3 isoform 1 or a, KCC4 isoform 1). The sequence alignment was performed using pairwise sequence alignment with LALIGN software (EMBL-EBI). **(C)** Schematic representation of the functional role of Na^+-Cl^- importer NCC and Na^+-K^+-Cl^- importer NKCC2 in a kidney nephron. **(D)** Schematic representation of the functional role of Na^+-dependent Na^+-K^+-Cl^- importer NKCC1 and Na^+-independent K^+-Cl^- exporter KCC2 in a neuronal cell in health and diseases. Arrows indicate the direction of the ionic flux. All representations were created with BioRender.com.

1.1.1. Structure-function relationships

CCCs mainly form homodimers although multimeric states have been described in functional assays for N(K)CCs and KCCs[8–10]. Monomers for each of the CCC family members are characterized by a well-conserved transmembrane (TM) domain formed by twelve TM helices, one N-glycosylated extracellular (EC) domain, and on the cytosolic side, the amino-terminal (NT) and the large carboxy-terminal (CT) domains (**Figure 1.A**). All SLC12-CCC members share the same TM protein fold of the leucine transporter (LeuT[11], chapter 1.1.2 and **Figure 2**). The EC domain is characterized by a connecting loop between TM7 and TM8 in Na^+-dependent CCCs, whereas Na^+-independent CCCs have a longer loop between TM5 and TM6. The NT and EC domains are variable in amino acid length, much shorter than the CT domain, and poorly conserved among the CCC members. The extracellular domains contain glycosylation sites, whereas the intracellular domains contain phosphorylation sites to modulate CCC function[12] (**Figure 1.A**). Molecular heterogeneity is also provided by multiple CCC isoforms generated by alternative splicing and promoter usage[13].

Many functional and mutagenesis studies have detected and measured ion/ligand binding and ion transport[14], indicating that variation of residues in the TM domains or truncation of the CT domain can compromise ion affinity and transport activity[15,16]. In particular, the CT domain plays a key role in CCC assembly[8,9,17–19], as demonstrated by cell and chemical biology studies on NCC oligomerization in glycosylated monomers and multimers. For example, mistargeting to the plasma membrane is a possible cause of degradation of NCC chimeras formed by co-expression of wild-type (WT)-NCC and CT domain mutant subunits[19]. Moreover, in the prokaryotic CCC homolog, the CT domain dimer interface shows small and hydrophilic buried areas that can be disrupted by point mutations and regulate dimerization[17]. The complex structure of CCCs allows the formation of discrete ion-binding sites nested within the TM domains, although ion selectivity and stoichiometry can differ among NCC, NKCCs, and KCCs[20]. Ion translocation occurs via the alternating access model, which involves switching between an inward-open (IO) ↔ outward-open (OO) conformational state that exposes the ion-binding sites to either side of the membrane[21,22] (**Figure 2.A**).

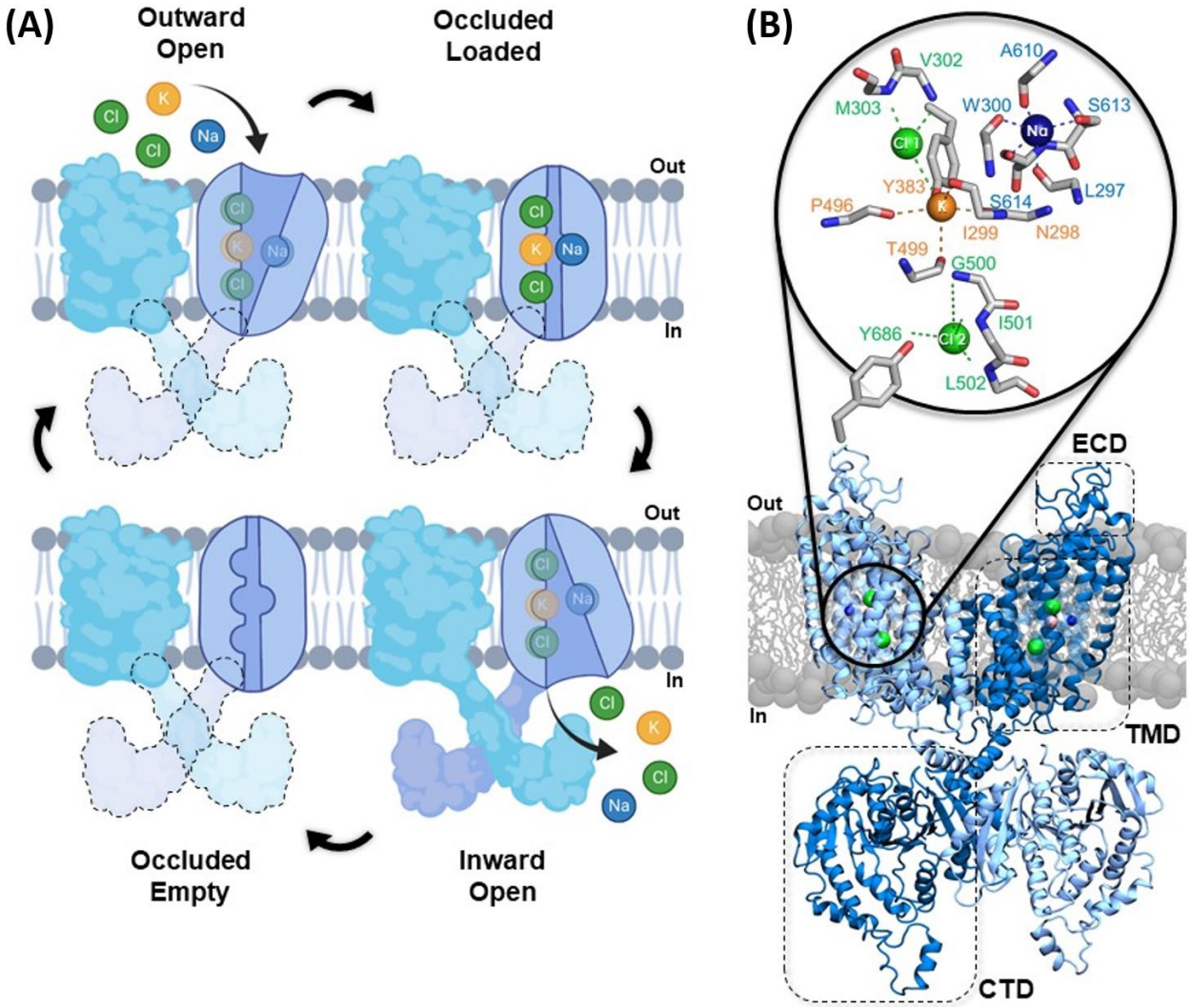

Figure 2. Mechanism for ion transportation in CCCs. **(A)** Schematic representation of the different states that Na^+-dependent CCCs adopt to transfer ions across the cell membrane. The CT domain is shown for completeness of information, although represented as transparent for states in which its exact conformation and position are not known, yet. Similar mechanism of ion transport (although in the opposite direction) has been hypothesized for Na^+-independent CCCs. Representation was created with BioRender.com. **(B)** Model of NKCC1 structure obtained by merging the TM domain of *h*NKCC1 (PDB code: 6PZT), with bound ions (Cl^- ions are in green, K^+ in orange, and Na^+ in blue), and the CT domain of the *Dr*NKCC1 (PDB code: 6NPL), all solved by cryo-EM. Each monomer is formed by EC-TM-CT domains. In this figure, one monomer is depicted in light blue (left) and the other in dark blue (right). In this representation, the right monomer is in front of the left monomer, which remains behind in the domain swap configuration." The magnified area shows the residues (in *h*NKCC1) that form the ionic binding sites. We performed the merging using the software Visual Molecular Dynamics (VMD).

1.1.2. Mechanism for ion transport

CCC ion transporters are characterized by a structural topology that was first described for LeuT (in both outward-open OO and inward-open IO states, substrate free[23]), a bacterial (*Aquifex aeolicus*) amino acid/Na^+ symporter and member of the amino acid-polyamine-organocation (APC) transporter superfamily[11]. A number of APC transporters, all adopting a similar LeuT fold, have been solved: the Na^+/hydantoin transporter, Mhp1[24], amino acid antiporter, AdiC[25], Na^+/betaine symporter, BetP[26], Na^+-independent amino acid transporter, ApcT[27], Na^+/galactose symporter, vSGLT[28], carnitine transporter, CaiT[29], and sialic acid transporter, SiaT[30]. The LeuT fold is characterized by a pseudo two-fold symmetry with two five-helix repeats (TM1-5 and TM6-10) orientated in an inverted architecture along the vertical axis, with a central binding cavity for Na^+ ions and leucine. Importantly, knowledge of the structure-function relationship of LeuT guided mutagenesis, cell-based assays, and *in vitro* studies with radiolabelled substrates of CCCs[11,23]. The LeuT transporter functions through the rocking bundle alternating-access mechanism, which diversifies transporters from channels. This involves multistate isomerization with OO, ligand bound/occluded, and IO states. These allow the substrate to cross the membrane[31]. A similar mechanism has been hypothesized also for CCCs. For example, in Na^+-dependent CCCs, the access model starts with ions that first bind extracellularly in an OO (empty) state of the transporter. This triggers an initial conformational state change of the transporter toward a loaded occluded state. Then, the transporter gradually moves into the IO conformation. This OO → IO conformational state transition releases the ions into the cell, with the transporter then returning to an OO conformation. In this latter conformation, the transporter is ready to restart the stepwise mechanism for ion internalization (**Figure 2.A, B**). For all CCCs, what remains unclear is the exact dynamic mechanism and trigger for state interconversion.

1.1.3. Structural insights from CCC cryo-EM structures

Six CCC members have been resolved with cryo-EM (i.e., NKCC1, NCC and KCC1-4[32–39]), confirming the dimeric organization of CCCs, except mouse (*m)*KCC4 resolved as a monomer[40]. The first high-resolution structures of zebrafish *(Danio rerio, Dr)* NKCC1[32] and human (*h)*KCC1[33] were reported in 2019. In 2020-2021, six independent studies reported new structures of *h*NKCC1, *m*KCC2 and *h*KCC2-4 transporters, alone or in complex with inhibitors[32–38,40] (Table 1 from our review[41] and chapter 1.1.5). These structural data confirmed the predicted LeuT structural fold with a large ordered and glycosylated loop in the EC domain and two cytosolic domains (NT and CT) with numerous phosphorylation sites. Moreover, these data revealed that TM11 and TM12 form the dimerization interface through an inverted V-shaped structure (helix-turn-helix), while the TM12-scissor helix

connects the TM with the CT domain. The dimerization seems also to be aided by cell membrane lipids at the interface region[38].

The specific conformation of the resolved transporters is crucial to determine the structural features that modulate the IO ↔ OO conformational state switch. This is central to understand the mechanism of ion permeation in CCCs. In particular, some of the solved IO conformation structures of the CCC dimers (i.e., *Dr*NKCC1, *h*KCC1, *m*KCC2, *h*KCC2a-b, *h*KCC3a-b, *h*KCC4a[32,35–38]) showed the CT dimeric domain in the full-length molecular assembly for the first time. These structures also revealed that the CT domain of one protomer is located under the TM domain of the other protomer, creating a domain-swap configuration that stabilizes the dimerization. For *h*KCC2 and *h*KCC3-4, the dimeric structures of the CT domains are also stabilized by hydrophobic interactions among the scissor helix and other structural CT features[36]. Although resembling the architecture of the dimeric prokaryotic CCC domain structure[17], the CT domain in *Dr*NKCC1 is slightly tilted with respect to the TM region when observed perpendicular to the membrane. Moreover, in *h*KCC2 and *h*KCC3, the CT domain is rotated clockwise by 70° as seen from the intracellular side, compared to *Dr*NKCC1[37]. The CT domain of *h*KCC2-4 weakly interacts with the TM domain (at the junction between TM12 and the scissor helix) through hydrogen bonds[36].

An NT domain peptide was also resolved in the *m*KCC2, *h*KCC2a-b, *h*KCC3b, *h*KCC4a structures, where it sterically closes the cytosolic vestibule and blocks transport activity[36–38]. Deletion or mutation of the NT domains in KCC2b and KCC3b enhances transport activity[36–38], which supports the role of the NT domain as an auto-inhibitory element. This closed (auto-inhibitory) state is well characterized in the KCC2a and KCC4a structures, where the NT domain peptide is bound mainly through hydrogen bond interactions with TM1a, TM5, TM6b and TM8. Notably, residues in the central portion of the NT domain are conserved among KCCs, suggesting a similar auto-inhibitory mechanism[36,38]. Comparison of the full-length *Dr*NKCC1 structure with the NT domain truncated structure indicates only minor structural adjustments between the TM and CT domains, with the proteins maintaining a similar overall conformation[32].

Finally, the EC domain was resolved in all recent cryo-EM structures. In the first *h*KCC1 structure (solved in the IO conformation), the two EC domains interact with one another, forming a dimeric closing cap toward the extracellular side. This seals the cavity formed by the TM domains[33]. In *m*KCC2, *m*KCC4 and *h*KCC2a, the extracellular gate is sealed by salt-bridge Lys(Arg)-Glu(Asp) interactions formed between residues along the TM7-TM8 linker,TM1, TM3, and TM10 domains interface[36,38,40].

Based on homology modeling and sequence alignment[4], NCC and NKCC2, whose structures are not yet solved, are expected to have the same structural architecture of the two EC domains and overall dimeric closing cap mechanism.

1.1.4. Ion-binding sites

Of the new CCC structures solved in the IO conformation, some contained ions inside the TM domain[32,33,36,37,40] (Table 1 from our review[41] and **Figure 2.B**). Such ion-binding sites were also tested through molecular dynamics (MD) simulations even based on structures originally solved without ions[32,38]. Overall, this confirmed previous homology modeling sequence alignment and biochemical studies, which suggested plausible ion-binding sites at the TM domain[4,14]. These ion-binding sites are surrounded by TM3 and the two discontinuous helices TM1 and TM6, connected by two flexible and conserved Gly residues as linkers (e.g., G301, TM1a-TM1b and G500, TM6a-TM6b, in *h*NKCC1)[34,38]. In NKCC1, the binding sites can be loaded from the extracellular gates through three potential entryways (one each for Na^+, K^+, and Cl^- ions). In NKCC1 IO structures, the gates have been captured either occluded (sealed via salt bridges) or open, suggesting a key role of TM1, TM3, TM5, TM6 and TM8 in extracellular-gating modulation[32,34]. Three exit pathways to the cytoplasm were proposed (possibly, one each for Na^+, K^+, and Cl^- ions)[34]. A key gating role is also played by hydrogen bonds involving R294 on TM1 and Q435 on TM5 of *h*NKCC1. This residue, conserved in all Na^+-dependent CCCs, is proposed to stabilize the open state of the intracellular gate[34,38]. The mechanism for ion permeation implies that Na^+ binds first, followed by one Cl^- ion, then the K^+ ion, and finally a second Cl^- ion[21]. Ions would then be released into the intracellular side in the same order, likely allowing the passage of some water molecules[38,42]. Nevertheless, this still needs to be proved since current structures lack the resolution to clearly detect bound water molecules in the ion pathway.

The new CCC structures revealed that Na^+ coordination is mediated by conserved Ser residues on TM8 (S538-S539 in *Dr*NKCC1, S613-S614 in *h*NKCC1)[32,34]. Notably, these serines (and/or threonines) are highly conserved among CCC transporters, with a similar TM fold and in line with what has been observed in LeuT and neurotransmitter/sodium symporter (NSS) family homolog structures[11,23,31]. Interestingly, in KCC — which activity does not require Na^+ — the conserved Ser residues in TM8 are replaced by one Cys and one Gly[32].

In the *Dr*NKCC1 structure, the K^+ ion binds to residues on the discontinuous helices TM1 (N220 and I221), TM6 (T420 and P417), and to a highly conserved Tyr along TM3 (Y305 in *Dr*NKCC1 and Y383 in *h*NKCC1)[32,34,38], confirming previous studies[16]. Interestingly, Y383 is conserved in NKCCs

and KCCs but not in NCC, strengthening the notion that it may be required for K^+ transport. In addition, kinetic experiments in NKCC2 suggested the involvement of P254 and A267 in TM3 and T235 in TM2 in K^+ binding[8,43]. In *h*KCC1 (Y216), *h*KCC2a (Y218), and *h*KCC4a (Y216) structures, a Tyr residue contributes to specific K^+-binding[33,36,38]. Mutations of Y216, T432, Y589, S430 reduce or abolish KCC1 function[33]. Notably, K^+ transport activity is reduced by mutation of residues R140, K485, and F486, which disrupts the EC-TM domain interaction network in *m*KCC4. This is because this region is involved in the loading of K^+ between TM1, TM3, and TM6 (and Cl^- between TM6 and TM10)[40].

Finally, the *Dr*NKCC1 cryo-EM structure and MD simulations suggested two Cl^- binding sites (Cl1 and Cl2) above and below the K^+ binding site, in a region between TM1, TM6, and TM10. In MD simulations, Cl^- ions transiently bind to such solvent-accessible sites of the transporter[32,38]. Simulations of *Dr*NKCC1 suggested that the K^+ ion is also involved in Cl^- coordination, with Y454 (in Cl1) and Y611 (in Cl2). Mutations of any of these residues reduce or abolish the Cl^- transport[32]. In KCC1, Cl^- in Cl1 is coordinated by G134, V135, I136, S430, and the K^+ ion, whereas Cl^- in Cl2 is coordinated by G433, I434, M435, Y589[33]. Although Cl^- in Cl1 was not resolved in *m*KCC4, mutation of Y466, which is equivalent to Y454 in *Dr*NKCC1, reduces the transport activity[40]. Interestingly, KCC4 transport activity is decreased by mutation of the CCC-conserved residues Y589 in TM10 and Y216 in TM3, which coordinate Cl^- and K^+, respectively[40].

1.1.5. Small-molecule binding to, and protein amino acid sequence mutations in, CCCs linked to human disorders

The recently resolved CCCs are all in IO conformations only, but KCC1 and NKCC1 also resolved in OO conformation. Moreover, the KCC3 structure was resolved in complex with the inhibitor DIOA (Dihydroindenyl-oxy acetic acid), KCC1 was resolved in complex with the inhibitor VU0463271, whereas NKCC1 was resolved in complex with the inhibitor bumetanide (the chemical structure of the inhibitors can be seen in **Appendix Figure SI 10.A** and **SI 10.B**, respectively). The KCC3-DIOA complex showed that DIOA interacts with specific residues in the TM10-11 loop (R617) and TM12 (K664) in the central cleft between the two monomers of KCC3[37] (**Figure 3.A**). Interestingly, these residues are conserved in KCCs but not in NKCCs. The KCC1-VU0463271 complex was resolved in the OO conformation[35]. Here the drug fits a pocket formed by TM1b, TM6a, TM3 and TM10, a shared binding site of bumetanide in NKCC1[44]. In particular, VU0463271 hampers the salt bridge between R140 and E222 involved in the outer gate closure. Moreover, the Y216 residue

(critically involved in K^+ binding) interacts with VU0463271 through one hydrogen bond with the phenyl-3-pyridazinyl group. This creates a steric hindrance along the ion-permeation pathway. The fact that VU0463271-KCC1 is the only CCC structure solved in the OO conformation, together with the fact that the KCC1 IO conformation was solved without VU0463271, suggest that VU0463271 may stabilize the OO conformation of KCC1. Comparing the KCC1 IO and OO states, one can detect the positional shift of TM3, TM4, TM8, TM9, TM10, which regulates the extracellular gate (for the entry of Cl^- and K^+ to the binding sites, in proximity to TM1 and TM6) and occlusion of the intracellular gate. However, the solution of the KCC1-VU0463271 complex was obtained without K^+ in the buffer. Thus, the question of substrate/inhibitor competition for binding remains unresolved. Moreover, in cell line–based experiments, the potency of VU0463271 decreases when the uptake of thallium or rubidium (K^+ congeners - chemical species that share similar physico-chemical properties) increases[45]. VU0463271 also interacts with the conserved M215 residue located on TM3 adjacent to Y216, whose mutation decreases VU0463271 binding affinity by ~65 fold. Importantly, mutation of this residue in NKCC1 (M382) decreases the binding affinity of a loop-diuretic inhibitor bumetanide, suggesting a similar binding site for the respective targets of VU0463271 and bumetanide, namely *h*KCC1 and *h*NKCC1[16]. As for bumetanide, mutations in NKCC1 located on one side of TM3 (Y383, M382, A379, N376, A375, F372, G369, I368) decrease loop-diuretic inhibitor and ion affinity. Moreover, the A483C mutant in *r*NKCC1 (A493 in *h*NKCC1), part of the flexible and discontinuous helix TM6a and close to the Cl^--binding site, shows a 6-fold increase in bumetanide affinity with little or no change in ion affinities[46]. Studies indicating small-molecule binding sites are key to structure-based drug discovery programs to design new therapeutic approaches for the pathologies associated with mutations in CCC transporters (**Figure 3.B**).

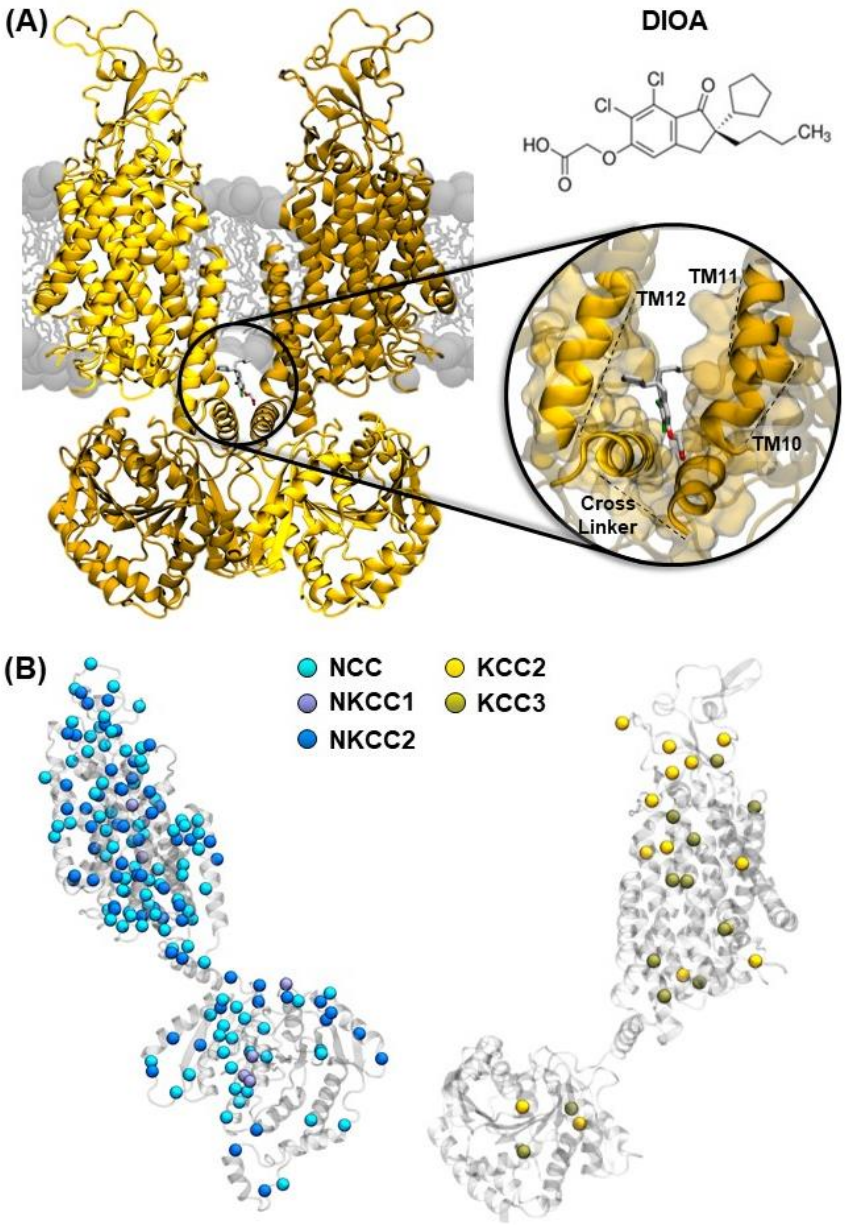

Figure 3. Binding site in KCC3 for the small-molecule DIOA, and human disorders linked to CCCs. **(A)** Representation of the TM domain and the CT domain of *h*KCC3, with the inhibitor DIOA bound in the central cleft, and solved by cryo-EM (PDB code: 6M22). The magnified area shows the DIOA binding-site in the dimeric interface, formed by TM11, TM12, and the cross-linker helices of both monomers. **(B)** *Left.* TM domain of *h*NKCC1 (PDB code: 6PZT) and CT domain of *Dr*NKCC1 (PDB code: 6NPL). Spheres represent residues that are associated to human pathologies, when mutated. Light, medium and dark blue represent residues identified in NCC, NKCC1, and NKCC2, respectively. To map mutations from *h*NCC and *h*NKCC2 on *h*NKCC1 TM domain structure, sequence alignments were performed using BLAST. The position of the mutated residues were extrapolated from their original sequence and aligned to NKCC1 sequence and structure. This same procedure was followed to map mutations from human NCC, NKCC1 and NKCC2 on *Dr*NKCC1 CT domain structure. *Right.* TM and CT domains of *h*KCC3 (PDB code: 7D90). Light and dark yellow spheres represent pathological mutations identified in *h*KCC2 and *h*KCC3, respectively. The *h*KCC2 protein sequence

was aligned to *h*KCC3 sequence and mutations for both *h*KCC2 and *h*KCC3 were mapped onto the superimposed structure.

1.1.6. Modulation of CCC activity by post-translational modifications

There are key phosphorylation residues in the NT and CT domains that modulate transporter expression, trafficking, activity, and oligomer/cluster formation in lipid rafts[47–51] (Table 2 from our review[41]). The structure determination of both wild-type and dephosphorylation-mimic cryo-EM KCC3b structures allowed the identification of mutations that mimic the effect of (de)phosphorylation. In KCC3b, T997 phosphorylation might be involved in maintaining the IO conformation by stabilizing the TM10-11 loop[37]. Such (de)phosphorylation events in CCCs often involve the "With No Lysine" (WNK) Ser–Thr kinases. For example, WNK1 and WNK3 activate NCC, increasing its expression, whereas WNK4 inhibits NCC function[52,53]. Interestingly, GABAergic transmission is modulated by increased WNK1 phosphorylation, which promotes NKCC1 phosphorylation/activation and KCC2 phosphorylation/ inactivation in neurons[50,54]. Moreover, WNK1 and WNK3 also activate NKCC2 through phosphorylation at NT domain residues[55,56]. Mutations of T96, T101, and T111 residues inhibit NKCC2 phosphorylation and activity in low Cl^- hypotonic stress, which normally activates NKCC2[55]. In *h*KCC3, key residues in the NT and CT domains are highly phosphorylated in isotonic conditions via WNK1 and WNK3, which lead to physiological inactivation of the transporter[48,57,58]. Mutation of these Thr residues to Ala resulted in constitutively active cotransport, suggesting that preventing phosphorylation may increase the activity[48]. Finally, the WNK kinases can also affect CCC regulation via the downstream kinase Ste20-related proline-alanine-rich kinase (SPAK)/oxidative stress response 1 (OSR1) and the protein kinases A and C (PKA and PKC)[51,56–61]. These additional players can form direct contacts with CCCs. This is the case for a 92-residue motif on the SPAK/OSR1 CT domain, which interacts with the NT domain of NKCC1 or the CT domain in KCC3 (and the motif RFXV in WNK1 and WKNK4)[57,60]. Interestingly, WNK3 activation by the WNK3-SPAK complex (or alone) enhances *h*NKCC1 activity through phosphorylation of T212 and T217 in concert with inhibitory KCC3 phosphorylation[57].

The glycosylation sites in CCCs are conserved EC domain residues in the loop between TM7 and TM8, in NCC and NKCCs, and in the loop between TM5 and TM6, in KCCs[4]. For example, the recent *h*KCC1 cryo-EM structure revealed two N-linked glycosylated residues in the long EC loop. This loop has six N-linked glycosylation sites in KCC2[62]. Glycosylation controls the correct folding and membrane localization of CCCs, preventing the internalization and degradation of the transporter[63] (Table 2 from our review[41]). For example, mutation of glycosylation sites at the EC

domain of NCC increased transport affinity or impaired membrane localization[64,65]. Moreover, in the EC domain of *h*KCC2 and *m*KCC4, mutation of glycosylation sites and close residues prevented protein glycosylation and drastically reduced transporter activity and membrane expression[18,40,66].

Ubiquitination is the least studied of the post-translational modifications of CCCs. However, several ubiquitination sites have been characterized for NCC. Interestingly, ubiquitination can directly modulate NCC transporter function, endocytosis, and degradation. Moreover, ubiquitination can also indirectly affect the membrane expression of NCC through the degradation of kinases involved in its phosphorylation[67]. Nevertheless, it is still not known what precise ubiquitination sites are responsible for specific ubiquitination-dependent NCC changes.

1.2. CCC mutations associated with human diseases

CCC mutations (e.g., missense, deletions, nonsense, frameshift, altered splice site) associated with human diseases result in changes in the amino acid sequence of CCCs prevalently at the level of the TM domain, with some also involving residues in the NT and CT domains. These mutations affect CCC protein synthesis (e.g., truncated or differently spliced proteins), processing, membrane insertion, function, and internalization (Table 3 from our review[41]).

Nearly 200 mutations in the SLC12A3 gene, which encodes for NCC, are linked to Gitelman syndrome (GS)[64,68]. GS is an inherited renal disorder characterized by hypokalemia, metabolic alkalosis, hypocalcemia, urinary calcium, and hypomagnesemia. The mutations linked to GS are predominantly located in the ion-translocation pathway, the EC domain, the TM-TM and TM-cytosol interfaces, and the NT and CT domains, likely affecting NCC folding and stability[32,69,70]. In vitro functional characterization of NCC missense mutations associated with GS revealed defective NCC plasma membrane expression, localization, and activity[71,72]. Interestingly, some NCC mutations associated with GS are also associated with salt-losing tubulopathy[73]. Other NCC mutations are linked to hypertension/increased Na^+ transport or reduction of blood pressure/Na^+ uptake[64,74]. NCC KO mice are healthy, fertile and grow normally despite GS-like symptoms[75].

Mutations in the SLC12A2 gene, which encodes for NKCC1, are associated with hearing, brain, and multiorgan disorders[15,76–78]. For example, mutations within the NKCC1 sequence have been found in patients affected by neurodevelopmental disorders (NDD) and/or bilateral nonsyndromic sensorineural hearing loss. All these mutations decrease K^+ transport in vitro[77]. A detected 22-kb homozygous deletion in NKCC1 is associated with Kilquist syndrome, a syndromic sensorineural hearing loss characterized by the absence of saliva, tears, and mucus release, and by respiratory/gastrointestinal problems[79,80]. Moreover, a de novo loss-of-function mutation leading to a frameshift and truncation of the NKCC1 CT domain has been linked to multiorgan impairment in vascular, pulmonary, gastro-intestinal, and urinary tissues[15]. NKCC1 KO mice die postnatally due to growth retardation, difficulties maintaining balance, and reduced blood pressure[81,82]. They also develop inner ear dysfunction and deafness, male infertility, salivation impairment, and nervous system deficits (hyperexcitability and impaired pain perception)[4,83]. Notably, altered NKCC1 expression has been described in patients and mouse models of Down syndrome, schizophrenia (SCZ), temporal lobe epilepsy (TLE), and Huntington disease[84].

More than 80 mutations of the SLC12A1 gene, which encodes for NKCC2, have been associated with Bartter syndrome (BS) type 1, a renal disorder characterized by polyuria, renal tubular hypokalemic alkalosis, hypercalciuria[85,86], and blood pressure alterations[74,87]. Other mutations in the NKCC2 TM and CT domains in antenatal/neonatal BS patients are associated with premature delivery, polyhydramnios, nephrocalcinosis, and hyperthyroidism[88–92]. Some of these mutations have been studied in vitro, showing a low expression profile and lack of Na^+ transport[93]. Other mutations in the TM and CT or NT domains have been linked to salt-losing tubulopathy or hypokalemic disorders, respectively[94,95]. NKCC2 KO mice exhibit BS-like symptoms that do not allow pups to survive[96].

No specific human disorders have been linked to mutations in the SLC12A4 gene, which encodes for KCC1. Nevertheless, KCC1 is relevant in hematopoietic lineage and cancer development[97]. KCC1 KO mice are similar to their WT littermates in terms of body weight, histological examination of organs, auditory system, and seizure susceptibility[98].

Mutations in the SLC12A5 gene, which encodes for KCC2, have been found in subjects affected by brain disorders. In particular, most patients with KCC2 mutation have some form of epilepsy, such as epilepsy of infancy with migrating focal seizures (EIMFS), febrile seizures, or idiopathic generalized epilepsy (IGE)[66,99–103]. Interestingly, R952H or R1049C point mutations found in patients with epilepsy are also associated with SCZ or autism spectrum disorder (ASD)[100,104,105]. Another mutation (R1048W) is also associated with ASD[105]. All these KCC2 mutants reduce expression, trafficking, and/or glycosylation and Cl^- extrusion activity[66,100,102,104,105]. KCC2 full-KO mice die immediately after birth due to motor deficits and respiration failure[106]. Isoform KCC2b KO mice are viable for up to 2 weeks and have generalized seizures[107,108]. Mice with mutations at KCC2 CT domain phosphorylation sites (preventing KCC2 phosphorylation) or constitutively KCC2 dephosphorylated mice (S940A, T906A and T1007A) display impairment of KCC2 activity and are good models of neurodevelopmental diseases, social/cognitive impairment, and status epilepticus, in line with human data[109–111]. Mice expressing phospho-mimetic KCC2 mutations (T906E-T1007E) have altered Cl- extrusion, which leads to early death, locomotor impairment, touch-evoked status epilepticus, and altered neuronal inhibition[50,112]. Notably, altered KCC2 expression has been described in patients with and/or mouse models of ASD, SCZ, TLE, Huntington disease, and Rett syndrome[113].

Mutations in the SLC12A6 gene that encodes for KCC3 have been found in subjects with agenesis of corpus callosum (ACC) with peripheral neuropathy (PN) and Andermann syndrome (AS), an early-onset PN associated with various degrees of mental disability, psychotic symptoms, and ACCPN[99,114–

[117]. In particular, T813X is the predominant KCC3 variant associated with ACCPN. T813X is correctly expressed and glycosylated but loses K^+ transport activity[117]. Moreover, T991A associated with early-onset and progressive PN abolishes KCC3 phosphorylation, resulting in a constitutively active transporter and altered cell-volume homeostasis[99]. Rare KCC3 variants have been found in bipolar disorder patients [104]. Finally, the P605L mutation, which leads to impaired K^+ transport, has been identified in people affected by congenital hydrocephalus and ACC but not PN[118]. KCC3 KO mice display deafness, reduced seizure threshold, neurogenic hypertension, and locomotor dysfunction, which resembles AS[117,119].

Only a de novo 2.6 kb copy number deletion in the KCC4-encoding gene (SLC12A7) was recently identified in a family affected by sporadic congenital hydrocephalus[118]. KCC4 KO mice develop progressive hearing loss until deafness and renal tubular acidosis to compensate for high urinary pH[119].

1.3. The role of CCC in water transport and associated pathologies

The choroid plexus (ChP) is a tissue characterized by high vascularization and is found in the brain ventricles. It fulfills two main functional roles. First, ChP is one of the principal sources that produce cerebrospinal fluid (CSF). Second, ChP also serves as the blood–CSF barrier – preventing the entrance of harmful metabolites and immune cells into the central nervous system (CNS)[120,121]. A significant feature of the cellular architecture and organization is that the choroid plexus epithelium (CPE) is made up of single-layer cuboidal cells[122], which to carefully regulate transport processes it has its membrane proteins asymmetrically distributed – this cellular feature is named cell polarization[123]. CPE polarization is organized in a basal and a luminal membrane, as in other polarized epithelia, although it presents atypical polarization – exemplified by NKCC1 expression in the luminal membrane instead of the expected basal membrane[124].

ChP has been thoroughly investigated for decades because of its participation in CSF formation and because CPE has one of the most efficient secretory rates[125]. The CPE is estimated to secrete 80% of the CSF[126] with a secretion rate of up to 0.4 ml/min per gram of tissue[125]. Usually, the human brain holds about 150 mL of CSF, with the CPE producing from 500 to 600 mL every 24 h – which is generally understood to mean that the human brain replaces CSF three to four times in this timeframe[127]. This rapid production of CSF suggests that any impediment to its circulatory pathway will lead to rapid accumulation, leading to increased intracranial pressure and eventually to hydrocephalus[128].

1.3.1. Clinical implications of cerebrospinal fluid accumulation

The dysfunction of the choroid plexus – cerebrospinal fluid biological intersection is associated with several neurological diseases. Altered CSF production has been observed in Alzheimer's disease due to increased amyloid deposits in the ChP[129], hyperaccumulation of CSF in posthemorrhagic hydrocephalus, leucocytes crossing the blood–cerebrospinal fluid barrier (BCSFB) in autoimmune diseases, and lymphocyte infiltration post-stroke, along with other neurodegenerative ailments[130–134].

Hydrocephalus, a type of ventriculomegaly accompanied by increased volume of CSF[125], is another common pathology associated with malfunctioning CSF circulation, leading to excessive accumulation[135]. Alternatively, CSF accumulation due to ChP production has been observed post-infection due to the immune system inflammatory response. The consequences of this pathology include injury to brain function, increased size of the brain ventricles, and direct damage to the neural vasculature[136].

Increased intracranial pressure is commonly associated with CSF accumulation, usually associated with other clinical conditions – e.g., stroke, tumors, infection, traumatic brain injury, and hydrocephalus[125]. It is also a consequence of intraventricular hemorrhage (IVH) causing posthemorrhagic hydrocephalus (PHH)[137], where increased ICP causes damage to the white matter and disrupts brain development in children and causes neurodegenerative damage in adults. Acute brainstem herniation and death have been observed after long-term increased ICP[138].

Notably, there are no targeted pharmacotherapeutic strategies to normalize CSF production, leaving invasive therapeutic approaches or insufficiently efficient transporter inhibitors to tackle this complex neuropathology. This highlights the need for a deeper understanding of the functional mechanism of NKCC1 and its role in transporting water at the ChP[139].

1.3.2. NKCC1 as a pharmacological target to treat cerebrospinal fluid accumulation

As previously mentioned, NKCC1 is located at the luminal membrane of choroid plexus epithelial cells[140]. It has also been shown that in adult brains NKCC1 plays an important role in CSF production, singlehandedly contributing to 50% of CSF secretions[42]. Consequently, bumetanide, a powerful NKCC1 inhibitor, when applied to the luminal side of the CPE decrease CSF secretion[141]. NKCC1 has been recently described as a water cotransporter, where researchers showed its ability to couple water transport and ion translocation, which under the right conditions this transporter is able to unusually export both water and ions, instead of its usual substrate import direction – helping to explain the role of NKCC1 in secreting CSF in the ChP[42].

It has been previously observed that after IVH, phosphorylation of the SPAK-NKCC1 cascade at the luminal membrane of ChP epithelial cells leads to hypersecretion of CSF[130]. Increased activity of the complex SPAK-NKCC1 is also observed in ischemic brain damage, where it leads to blood-brain barrier damage, neural excitotoxicity, and cytotoxic edema[142,143]. Recently, researchers were able to show that pathological overactivation of the SPAK-NKCC1 cascade causes damage to the ChP and surrounding tissue. Simultaneously, they also showed that blocking the SPAK-NKCC1 pathway by both SPAK and NKCC1 inhibitors, specifically bumetanide for the latter, protected ChP against stroke-induced damage[144]. Additionally, when NKCC1 activity is lowered either pharmacologically or by genetic deficiencies, decreased levels of blood-brain barrier breakdown and brain edema were observed, whilst maintaining tight juncture protein integrity[145]. Other studies have highlighted other regulatory routes that lead to the hyperactivation of NKCC1, contributing to increased CSF secretion

and aggravated hydrocephalus. For example, NLRP3 activation in ChP regulated NKCC1 phosphorylation levels directly impacting CSF secretion[146].

More direct evidence of the potential therapeutic potential of NKCC1 inhibition to treat CSF hypersecretion and its subsequent pathologies has recently been published. Intracerebroventricular delivery of bumetanide led to an 80% reduction in CSF secretion rate and a 50% reduction in ventricular volume after ventriculomegaly caused by IVH[138]. Further studies proved the function of function in CSF secretion, where application of bumetanide led to fewer phosphorylated NKCC1 positive cells being detected in the ChP after IVH[146].

Current knowledge on the dynamics of CSF hypersecretion at the ChP and the direct role of NKCC1 in this biological phenomenon have further highlighted the relevance in finding potent and selective NKCC1 inhibitors. A campaign that requires deepening our understanding of the underlying mechanisms of NKCC1 function.

1.4. Implications for CNS drug discovery

CCCs are unselectively targeted by widely used loop and thiazide diuretics to treat mild hypertension, edema, compromised blood pressure, and heart failure[4,5]. CCCs have been recently implicated in neuronal pathophysiology and cancer biology[6,147]. These diseases all involve gene mutations (Table 3 in our review[41]) or defective expression of CCCs[62,113]. The same CCCs are sometimes involved in multiple disorders, raising the possibility of treating them with one same drug. For example, the unselective NKCC inhibitor and diuretic drug bumetanide has been repurposed with positive outcomes in clinical trials and case studies to treat brain disorders in patients (e.g., ASD, SCZ, TLE, neonatal seizures, Parkinson's disease)[148]. Accordingly, the upregulation of NKCC1 and/or downregulation of KCC2 have been described in brain samples of patients and animal models of several brain disorders[84,113]. However, the strong diuretic effect of bumetanide, mostly due to NKCC2 inhibition, jeopardizes treatment compliance and creates safety issues for the chronic treatment required for brain disorders[84,149]. Thus, recent efforts have sought to develop NKCC1-specific antagonists and new KCC2 agonists[45,150,151].

In this context, the recent structural information on CCCs creates the possibility of structure-based design of new and selective CCC modulators. For example, combined with information from mutagenesis and chimeric-protein studies, these structures suggest the targeting of the TM domain and of specific residues at the CT and NT domains, which impact CCC sensitivity to ligands[32,36,37]. Because the extracellular loops in NCC and NKCCs have different amino acid sequences (despite a conserved structural motif), these loops could be a potential target for isoform-specific drugs. Moreover, the NT domain is poorly conserved among diverse CCCs, which could favor the development of selective drugs for diverse CCCs. Finally, chemical interventions to modulate kinase pathways could interfere with CT domain phosphorylation and thus with regulation of CCCs. Interestingly, this approach could exploit the fact that WNKs can modulate CCCs in opposite directions. Inhibiting WNKs could be especially important in diverse brain disorders characterized by increased intracellular Cl^- homeostasis. Indeed, in neurons NKCC1 functions as Cl^- importer, whereas KCC2 functions as a Cl^- exporter. Similarly, glycosylation (at the EC domain) or ubiquitination (at NT and CT domains) could also be considered to modulate CCC activity for therapeutic approaches. For example, targeting upstream glycosidases and/or deubiquitinating enzymes could be one strategy to improve CCC stability and avoid degradation in diseases where mutations of transporters lead to decreased activity[152]. Promoting protein degradation has been a strategy already investigated for other

SLC proteins involved, for example in tumor biology[153] or soluble proteins involved in proteinopathies with accumulation of misfolded or aberrant proteins[154].

In particular, the chloride importer NKCC1 and the chloride exporter KCC2 play a pivotal role in regulating neuronal chloride concentration. An imbalance in the expression ratio of NKCC1 to KCC2 has been linked to a variety of brain disorders. Bumetanide, an FDA-approved diuretic, has emerged as a potential inhibitor of NKCC1, offering a promising therapeutic avenue for numerous neurological conditions. However, its limitations, such as inadequate brain penetration and diuretic side effects due to its action on NKCC2 in the kidney, are evident. To address these challenges, there has been a surge in research focused on the development of novel NKCC1 inhibitors. This includes more selective bumetanide prodrugs, analogs, and other molecular entities with enhanced brain penetration. The pharmacological inhibition of NKCC1 is being explored as an effective strategy for managing neurological disorders. The advantages and drawbacks of repurposing bumetanide, as well as the potential benefits and risks associated with the introduction of novel NKCC1 inhibitors, are topics of significant interest and this emphasizes the need for continued research and development in this area[155].

Our understanding of CCCs has been enriched by their recent cryo-EM structures. These have revealed new chemical and biological insights into the structural topology of CCCs, including the orientation and flexibility of the diverse protein domains, the oligomerization state, and the exact location of ion/ligand binding-sites. This knowledge will stimulate the structure-based drug discovery of potent and selective inhibitors of CCCs. Surprisingly, diuretics are currently the only FDA-approved CCC-targeted drugs on the market, and they are all unselective inhibitors. But evidence suggests that it may be possible to modulate specific types and isoforms of CCCs by targeting specific, non-conserved protein domains. This would address many urgent medical needs, given the wide range of pathologies in which CCCs are implicated. Further elucidating the structure/function relationship of CCCs will unravel the mechanism for ion transport, leading to a better understanding of the pathophysiology of diverse diseases, and innovative, selective, and safe drugs for patients.

Chapter 2:
Computational tools as a magnifying glass for biological phenomena

2.1. Molecular dynamics

To investigate the function and mechanisms of CCCs we have chosen molecular dynamics (MD) simulations. MD simulations are a tool with the capacity of predicting the movement of every single atom in a molecular system, for example an ion transporter embedded in a membrane, over time. This is done based on a general model that describes the physics that rule interatomic interactions[156]. In general, MD simulations can capture different and relevant biomolecular processes. For example, conformational change, protein folding, ligand binding, by unveiling atomic positions of the system at a timescale resolution of femtoseconds. These simulations can also be used to understand the response of the simulated system to different types of perturbations, at an atomic level, like protonation, mutation, phosphorylation, and the presence or absence of a bound ligand[157].

In other words, MD simulations can compress our current understanding of physics and chemistry to create an atomistic scale representation of small subsections of the world around us, and then offer results that are often validated using wet lab experiments. This tool has been around for almost 70 years, where its first implementation was an MD simulation of simple gases[158] and the first MD simulation of a protein was performed 20 years later[159].

Recently, the popularity of MD simulations in neuroscience research articles has substantially increased[157]. The authors of the review identified two explanations for this increase. First, experimental structures of critical neuroscience protein have been only elucidated recently (for example, NKCC1's first structure[32] in 2019) thanks to advances in cryo-EM techniques. These experimentally obtained structures are extremely important because they provide a starting point for MD simulations. Second, MD simulations have become easily accessible to the average scientist, both in ease-of-use and the hardware requirements[157].

In simple terms, an MD simulation is based on the concept that starting from the 3D cartesian positions of every atom in a molecular system (in our case, NKCC1 embedded in a membrane in a solution of water, sodium, chloride, and potassium), it is then possible to calculate the force that each atom exerts on all other atoms. Using Newton's laws of motion, we can now determine all atomic

positions as a function of time. By repeating the force calculation, and then determining atomic positions at the next step in time, we can obtain a trajectory that describes the atomic positions of our entire molecular system through the simulated timespan. Currently, there are no experimental techniques that provide atomic level resolution of a biological system through time, which indicates how powerful MD simulations can be. The force calculations are performed using a molecular mechanics (MM) force field, of which there are several, but whose parameters are fit to either quantum mechanical (QM) calculations or experimentally obtained measurements. These force fields are approximations that, for example, treat covalent bonds as springs. Additionally, a limitation of MD simulations is that there is no forming nor breaking of covalent bonds. The determination of the atomic spatial positions, using the force field calculated forces, happens at timesteps at the femtosecond scale. But since biological phenomena happen at much greater timescales, from simple events at the nanosecond scale, to more and more complex events that occur at least at the microsecond scale, MD simulations usually comprise up to billions of time steps. This great number of steps, in combination with all the atomic interactions that must be computed for each step, are in great part why MD simulations are so expensive in computational terms[157]. This also means that the larger the system, the more expensive it is to simulate, further limiting the computationally accessible timescale.

In this latter case, there is a family of computational methods that have been designed to sample the space beyond what is accessible in a standard (or equilibrium) MD simulation. These methods are called enhanced sampling techniques, and they allow the user to "accelerate" or guide a MD simulation and observe non-equilibrium states and undiscovered parts of the free energy landscape that define protein conformations. For example, and for a bit of foreshadowing, one could use equilibrium MD to independently explore the inward open conformation and the outward open conformation of NKCC1 and its behavior in both conformational energy minima. But computationally accessible timescales are not enough to observe an inward open – outward open conformational transition, which would then require the use of enhanced sampling techniques.

In the given example, by applying these modern techniques, one could analyze the trajectories that contain conformational transitions of NKCC1 and identify essential protein features that define the computationally identified mechanism for conformational transitions. Based on these features, experiments can be proposed to a wet lab, for example mutating key residues, and then evaluating the

effect of these mutations on protein function. In such a way, we can validate the computational efforts and the hypothesis extracted from MD simulations.

With this in mind, let us explore in more detail the theory behind MD simulations before I delve into simulations of CCCs.

2.1.1. Theory of molecular dynamics

Molecular Dynamics (MD) is a computational method that offers a microscopic-level view of the physical movements of atoms and molecules over time. By simulating the interactions and the time-evolution of the positions of these particles, MD provides insights into the dynamic behavior of molecular systems.

Every MD simulation follows the same basic set of steps, where the first step is to obtain the initial configuration of the system of interest. This initial configuration is built by two main components: the **initial protein structure** (or the cartesian coordinates for the positions of every atom in the system) and the **initial velocities** of every atom in the system. The second step is **force calculation**, where the force acting on every atom is computed – considering bonded and non-bonded interactions. The third step is the determination of the **updated coordinates** for every atom in the system, based on the forces acting on them. This step is performed by numerically solving Newton's equations of motion. The fourth and last step is the outputting of the current state of the system, which includes the new atom coordinates and velocities. Using these two data sets, steps two through four can be repeated until the simulation reaches the desired length[160].

It is essential to understand the pivotal role of the **initial structure**. This structure serves as the starting point for simulations, determining the initial positions of all atoms in the system. A well-chosen initial structure can lead to more accurate and meaningful results, while a poorly chosen one often leads to unphysical behaviors and misleading outcomes. The initial structure often comes from experimental data or theoretical predictions. For example, experimental data on protein structures can be found in the Protein Data Bank – which contains thousands of structures from X-ray crystallography and recently cryo-EM, whereas theoretical predictions can be obtained by using software such as Alpha Fold[161] or Modeller[162]. Acquiring such a structure is generally the limiting factor when running MD simulations, and several protein families remained unstudied because no known structure existed[157]. CCCs were one of these previously structurally unknown protein families. Indeed, CCCs became experimentally available due to recent advances in cryo-EM.

Once a good structural starting point is identified, we can build our simulation box. This box can take several shapes, but commonly a cubic box is selected. A water model is chosen (check the next chapter for a more detailed description of water in MD simulations), and the box is then filled with water molecules, solvating our system. Another important step is the addition of counterions if the system is not neutral. Although, physiological concentration of ions can be added to the simulation (and it is generally recommended to do so – as we will see in the following chapters). With these steps completed, all the atoms required for an MD simulation have been included, and **initial velocities** can be assigned to each atom. Typically, these velocities are assigned based on a Maxwell-Boltzmann distribution at the desired starting temperature – which is defined by the user depending on the protein and/or experimental conditions.

In MD simulations, boundary conditions are crucial. They define how atoms at the edge of the simulation box interact with other atoms. The most commonly used boundary condition is the periodic boundary condition (PBC). With PBC, atoms that move out of the simulation box on one side re-enter on the opposite side, creating an illusion of an infinite system. Without PBC, simulations can suffer from "edge effects," where atoms at the boundaries experience different forces than those in the center[163]. This can lead to unphysical results and artifacts in the simulation. Additionally, without PBC, the size and shape of the system can significantly influence the results, making it challenging to study bulk properties.

The next step is **force calculation**, but first we must talk about molecular mechanics (MM). MM is a method used to predict the structure, energy, and other properties of molecules without considering quantum mechanics. In this context, not considering quantum mechanical effects means that there are no electrons being simulated and therefore covalent bonds cannot be formed or broken. It uses classical physics to model molecular systems, with the potential energy of the system described as a sum of different energy terms:

$$E_{total} = E_{bond} + E_{angle} + E_{torsion} + E_{vdw} + E_{electrostatic}$$

Where E_{bond} is the bond stretching energy, E_{angle} is the bond angle bending energy, $E_{torsions}$ is the torsional or dihedral angle energy, E_{vdw} is the van der Waals interactions energy, and $E_{electrostatic}$ is the electrostatic interactions energy.

To compute these terms, we must first understand atom types and forcefields. Force fields are mathematical models that describe the interactions between atoms and molecules in a system. They

are foundational to MD simulations, providing the necessary parameters and equations to calculate the potential energy of a system. Each force field is a collection of equations and associated parameters tailored to specific types of molecules and interactions. For example, let us consider a force field description of the amino acid phenylalanine. A force field will contain all associated parameters of this molecule in equilibrium. Atom types are classifications that define the chemical nature and behavior of atoms. They dictate how an atom will interact with others, with different types for carbons in protein backbones versus the aromatic ring in the sidechain of phenylalanine, for instance. In this case, the associated parameters are the bond lengths between atom types, the angles between them, and the dihedral angles.

In this work, I have used the AMBER force field[164], which in its functional form defines E_{bond} and E_{angle} as harmonic ideal springs:

$$E_{bond} = \sum_{i}^{\#\ bonds} k_{bi}(l_i - l_i^0)^2$$

Where l_i is the length of bond i, l_i^0 is its length at equilibrium, and k_{bi} its force constant.

$$E_{angle} = \sum_{i}^{\#\ angles} k_{ai}(\theta_i - \theta_i^0)^2$$

Where θ_i is the value of angle i, θ_i^0 is its value at equilibrium, and k_{ai} its force constant.

On the other hand, the term $E_{torsion}$ is expressed as a torsional potential for dihedral angles. In this case this is represented as a cosine series expansion[165], as follows:

$$E_{torsion} = \sum_{i}^{\#\ torsions} \sum_{n}^{\#\ cosines} \frac{1}{2} V_i^n [1 + \cos(n\omega_i - \gamma_i)]$$

Where ω_i is the value of dihedral torsion i. V_i^n, n and γ_i are the magnitude, multiplicity, and phase of the cosine summation.

Before delving into the non-bonded terms of the potential energy, E_{vdw} and $E_{electrostatic}$, we must first discuss charges. In MD simulations, as previously stated, electrons are not considered, but atomic charges are essential for the dynamical motions of proteins. To solve this issue, force fields will usually include partial charges for each atom type. Partial charges arise due to the uneven distribution of electron density in a molecule. In MD simulations, these charges play a pivotal role in determining the

electrostatic interactions between atoms. There are several methods to determine partial charges. Quantum mechanical calculations, such as those using the Hartree-Fock method[166] or Density Functional Theory (DFT)[167], can be used to compute the electron distribution and subsequently derive partial charges. Empirical methods, like the Mulliken[168] or RESP[169] (Restrained ElectroStatic Potential) methods, are also popular.

In the Amber force field, the non-bonded terms are expressed within one double summation over all atom pairs. But for clarity, I will show here each term individually. The term E_{vdw} for van der Waals interactions is expressed as a 6-12 Lennard-Jones potential, which considers London dispersion forces and exchange correlation forces:

$$E_{vdw} = \sum_{i}^{\#\,atoms} \sum_{j>i}^{\#\,atoms} \epsilon_{ij} \left[\left(\frac{r_{ij}^0}{r_{ij}} \right)^{12} - 2 \left(\frac{r_{ij}^0}{r_{ij}} \right)^{6} \right]$$

Where ϵ_{ij} is the well depth, r_{ij}^0 the distance for which London and exchange energetical contributions cancel out for the atom pair i and j, and r_{ij} is the distance between atoms i and j.

The last term, $E_{electrostatic}$, is expressed as a double summation of the Coulombic formulation:

$$E_{electrostatic} = \sum_{i}^{\#\,atoms} \sum_{j>i}^{\#\,atoms} \frac{q_i q_j}{4\pi\epsilon_0 r_{ij}}$$

Where q_i and q_j are the partial charges on atoms i and j, ϵ_0 is the vacuum permittivity, and r_{ij} is the distance between atoms i and j.

With the **force calculation** step completed, we now have both the forces acting on the atoms that comprise the system along with their velocities. These are the essential components of the next step in a MD simulation, **updating atomic coordinates** at the next time step. These new system configurations are generated by integrating Newton's laws of motion, and when done successively results in a trajectory that shows how the positions and velocities of our system change with time. In classical MD the trajectory is derived by resolving the differential equations inherent in Newton's second law ($F = ma$)[165]:

$$\frac{d^2 \boldsymbol{r}_i}{dt^2} = \frac{F_{\boldsymbol{r}_i}}{m_i}$$

This equation characterizes the movement of an atom with mass m_i along a position vector ($\boldsymbol{r}_i$), where $F_{\boldsymbol{r}_i}$ represents the force acting on the atom in that direction. At its core, integration in MD is about evolving the system from one point in time to the next, based on the forces acting on each atom. In other words, the integration algorithm determines the new spatial coordinates of every atom in the system as the simulation progresses. Starting from an initial set of positions and velocities for all atoms, the forces acting on each atom due to their interactions with neighboring atoms are computed.

The time interval over which the integration is performed is termed the 'time step'. It is a crucial parameter in MD simulations. The choice of the time step is a balance between accuracy and computational efficiency. Shorter time steps offer more accurate simulations by capturing high-frequency vibrations (like bond stretching in molecules), but they require more computational steps to simulate the same physical time, making the simulation computationally expensive. On the other hand, longer time steps can miss important fast motions in the system and can even lead to numerical instabilities, where the simulation produces unphysical results. Typically, time steps in the range of one to five femtoseconds (fs) are chosen for most MD simulations, ensuring that the fastest motions (like hydrogen atom vibrations) are accurately captured[170].

Following this consideration of time steps, it is equally crucial to address the mechanisms that maintain the desired thermodynamic conditions during an MD simulation: thermostats and barostats. In the realm of MD simulations, a thermostat is an algorithmic tool designed to control and maintain the temperature of the system. As simulations progress, the kinetic energy of the system can drift due to various interactions, leading to temperature fluctuations. Thermostats counteract these fluctuations by either adding or removing kinetic energy, ensuring the system remains at the target temperature. There are several types of thermostats, each with its own mechanism. For example, the Berendsen thermostat[171] rescales the velocities of atoms to bring the temperature of the system closer to the desired value. It allows for rapid equilibration but does not strictly adhere to the canonical ensemble. Unlike the Berendsen, the Nose-Hoover thermostat[172,173] introduces additional degrees of freedom to the system to control temperature, ensuring adherence to the canonical ensemble. Another example of a thermostat algorithm is the Andersen thermostat[174], which mimics collisions with an imaginary heat bath by periodically reassigning velocities to atoms based on the desired temperature.

While thermostats control temperature, barostats are responsible for regulating pressure in an MD simulation. They adjust the volume (and sometimes the shape) of the simulation box to maintain the desired pressure. This is essential, especially when studying systems under conditions that mimic real-world atmospheric or physiological pressures. For example, the Parrinello-Rahman barostat[175] adjusts the shape and size of the simulation box based on the stress tensor of the system, ensuring isotropic scaling, and maintaining the desired pressure. In essence, thermostats and barostats are the guardians of thermodynamic stability in MD simulations. They ensure that the system remains under the desired conditions, providing a more realistic and controlled environment for the study of molecular behaviors.

Building on the foundational roles of thermostats and barostats in maintaining thermodynamic stability, it is imperative to delve deeper into the statistical frameworks that underpin these simulations. These frameworks, known as ensembles, offer a comprehensive understanding of the behavior of the system under various conditions, further enhancing the depth and breadth of insights gained from MD simulations.

In the context of statistical mechanics and molecular dynamics, an ensemble is a collection of a large number of virtual copies of a system, each representing a possible state that the system can be in. Ensembles provide a framework to average properties over these states, offering a statistical approach to understanding the behavior of molecular systems[165]. Different ensembles are defined based on which macroscopic properties are held constant. In the microcanonical ensemble (NVE), the number of particles (N), volume (V), and energy (E) are held constant. This ensemble is representative of an isolated system with no exchange of energy or particles with its surroundings. It is useful for studying fundamental properties of molecules and understanding the inherent dynamics of a system. In the canonical ensemble (NVT), the number of particles (N), volume (V), and temperature (T) are held constant. This is the ensemble generated by the Nose-Hoover thermostat. In the isothermal-isobaric ensemble (NPT), the number of particles (N), pressure (P), and temperature (T) are held constant. The Parrinello-Rahman barostat generates this ensemble. The NPT ensemble is representative of real-world conditions where systems are often subjected to constant atmospheric pressure. It is particularly useful for studying phase transitions, compressibility, and systems that might undergo significant volume changes. In the grand canonical ensemble (μVT), the chemical potential (μ), volume (V), and temperature (T) are held constant. This ensemble allows for the exchange of particles with a reservoir. The grand canonical ensemble is essential for studying systems in equilibrium with a particle reservoir,

like in adsorption phenomena or when studying reactions where the number of molecules can change[165].

Ensembles provide a theoretical framework to understand the behavior of molecular systems under various conditions. By defining the macroscopic properties that are held constant, ensembles allow us to simulate and study systems under conditions that mimic real-world experiments. Moreover, the choice of ensemble can influence the results of a simulation, making it essential to select the appropriate ensemble for the system and properties of interest.

2.1.2. Introducing atomistic water

Water is a fundamental component of biological systems, and its accurate representation is crucial for understanding the behavior of proteins, nucleic acids, and other biomolecules in their natural environment. Molecular dynamics (MD) simulations, which provide a microscopic view of molecular motions over time, heavily rely on the accuracy of the water model used. As promised in the previous chapter, we will now delve into the various water models employed in MD simulations, emphasizing atomistic models while also briefly discussing their predecessors and non-atomistic counterparts.

Before the advent of atomistic models, researchers employed simpler models to represent water in simulations. These models, while less detailed, provided foundational insights into the behavior of water in molecular systems. For example, continuum models[176] treat water as a continuous medium with specific dielectric properties. These models are computationally less demanding and are often used in electrostatic calculations. They are particularly useful for large-scale simulations where detailed water interactions are not the primary focus. However, they lack molecular detail and cannot capture specific interactions like hydrogen bonding. Moreover, lattice models[177] represent water molecules as points on a lattice. These models can capture some essential properties of water, such as hydrogen bonding, but lack the flexibility and detail of atomistic models. They are often used in coarse-grained simulations and provide a balance between computational efficiency and accuracy.

Atomistic models provide a detailed representation of water molecules, capturing the nuances of their interactions. These models are widely used in MD simulations of biological systems due to their accuracy. The SPC model[178] represents a water molecule as three-point charges: one for the oxygen atom and two for the hydrogen atoms. This model captures essential electrostatic interactions but lacks polarization effects. It is a widely used model due to its simplicity and computational efficiency. The TIP models are a series of refined atomistic water models. TIP3P[179] uses three-point charges,

similar to the SPC model. TIP4P[179] introduces an additional point charge to better capture polarization effects. TIP5P[180] further refines the model by adding another point charge. These models are more computationally demanding than the SPC model but offer improved accuracy when simulating biological systems.

Water plays a pivotal role in the behavior of biological molecules. Its dynamic nature and ability to form complex hydrogen bond networks make it a unique solvent that can influence the structure, dynamics, and function of biomolecules. An example of the importance of water is its great influence in protein folding[181], the process by which a protein adopts its functional structure. Water molecules can stabilize certain protein conformations through hydrogen bonding and hydrophobic interactions. Moreover, the dynamic nature of water allows it to rapidly adapt and respond to changes in the protein structure, facilitating the folding process. Another example is that of ligand binding[182], which is a fundamental process in biology, underlying enzyme catalysis, signal transduction, and drug action. Water molecules in the binding pocket can either facilitate or hinder the binding process. Some water molecules can act as bridges, enhancing the interaction between the protein and ligand. In contrast, others might need to be displaced during ligand binding, contributing to the binding free energy. Accurate water models can help predict these water-mediated effects, leading to better predictions of binding affinities and mechanisms.

2.1.3. Involvement of ions in simulated biological systems

Ions are atoms that have gained or lost one or more electrons, resulting in a net positive or negative charge. Based on their charge, ions can be classified into two main categories: cations and anions. Cations are positively charged ions, such as K^+, Na^+, whereas anions are negatively charged ions, like Cl^-. The physical properties of ions, such as size and charge, play a determinant role in their behavior in biological systems. In a medium, ions move under the influence of an electric field – although lacking an electric field, like in the simulations we will explore in following chapters, ions will still move albeit seemingly stochastically.

Ions play pivotal roles in various biological processes. For example, K^+ and Na^+ are essential for generating and propagating action potentials in neurons. These electrical signals are crucial for transmitting information within the nervous system. Alternatively, many enzymes require specific ions as cofactors to function optimally. For instance, magnesium ions (Mg^{2+}) are essential for the activity of many DNA polymerases[183].

In other words, ions play a crucial role in biological systems, and their inclusion cannot be disregarded in MD simulations. As we saw previously, the force field requires a set of parameters for every object that will take part in the simulation. The representation of ions in force fields requires careful parameterization to capture their unique properties, such as charge, size, and polarizability[184]. Accurately modeling ionic interactions is challenging due to the long-range nature of electrostatic interactions and the need to account for polarization effects. Traditional force fields, which use fixed charges[185], often struggle to represent the dynamic nature of ionic interactions in varying environments. Polarizable force fields, such as those based on the Drude model[186], offer a more dynamic representation by allowing charges to fluctuate based on their local environment.

The interactions between ions and water molecules are often related to the important biological processes mentioned before. These interactions, often termed as hydration, are fundamental in determining the behavior of ions in aqueous solutions and have profound implications for phenomena ranging from solvation to ion transport. An important aspect of ion hydration is the formation of hydration shells, which are structured layers of water molecules that surround an ion in an aqueous solution. The formation of these shells is primarily driven by the electrostatic interactions between the ion and water molecules[187]. The presence of hydration shells significantly influences the thermodynamic properties of ions, including their solvation energies and mobility in solution[188]. The water molecules in the hydration shell exhibit distinct dynamic behaviors compared to those in the bulk solution. These dynamics are influenced by the strength and nature of the ion-water interactions[189]. For instance, water molecules around ions with high charge densities may exhibit reduced mobility due to stronger electrostatic attractions. The sign of the charge of the ions will also determine the orientational dynamics of water molecules. A cation will induce water molecules to orient the oxygen atom towards it, whereas an anion will induce water molecules to orient either hydrogen towards it. This effect propagates towards the bulk solvent, since the first layer of water molecules will present a homogeneous outer layer with a specific charge distribution[187] that will attract bulk water in a specific orientation. The residence time of water molecules in the hydration shell, their exchange rates, and their rotational dynamics provide a comprehensive picture of the influence of the ion on local water structure and dynamics.

Ions also have a much more direct effect on protein structure, function, and dynamics. Ions influence the folding pathways and stability of proteins by interacting with specific amino acid residues and modulating the electrostatic environment[190]. The presence of certain ions can either stabilize or

destabilize specific protein conformations. For instance, divalent cations like Mg^{2+} and Ca^{2+} often stabilize protein structures by bridging negatively charged residues, thereby promoting protein folding and enhancing stability[191]. Conversely, high concentrations of monovalent ions can lead to protein denaturation due to charge screening effects. Proteins often possess specific binding sites that can selectively recognize and bind ions. These sites are crucial for the function of the protein and can be involved in catalysis, signal transduction, or ion transport[192]. Ion channels, a subset of these proteins, are specialized to allow the selective passage of ions across cell membranes. The selectivity of these channels is determined by the specific amino acid residues lining the channel pore, which interact with the ions based on their size, charge, and hydration shell[193]. Ions can significantly influence the dynamics of proteins. Their binding can induce conformational changes, modulate protein flexibility, and even drive large-scale domain movements[194]. For instance, the binding of calcium ions to calmodulin induces a significant conformational change, allowing the protein to interact with its target proteins[195]. Similarly, the dynamics of enzymes can be modulated by the presence of cofactor ions, influencing their catalytic activity.

The presence and concentration of ions in the cellular environment can significantly influence membrane dynamics, impacting its overall function and stability. For instance, ions influence the membrane potential, a crucial determinant of cellular activity that dictates the electrical gradient across the cell membrane. Particularly cations such as Na^{+}, K^{+}, and Ca^{+}, are instrumental in establishing and maintaining this potential. The differential distribution of these ions across the membrane, facilitated by ion channels and transporters, results in an electrical potential difference[196]. This potential is essential for processes like nerve impulse transmission and muscle contraction. Ions can also interact directly with lipid bilayers, influencing their structure and properties. For instance, certain ions can bind to or disturb the polar head groups of lipids, leading to changes in bilayer thickness, curvature, overall stability, and fluidity. For example, divalent cations like Ca^{2+} can bridge adjacent lipid molecules, leading to a more ordered and less fluid membrane. Conversely, monovalent ions might increase fluidity by disrupting lipid-lipid interactions[197].

2.1.4. Membranes for integral proteins – degrees of complexity

Cell membranes, often referred to as plasma membranes, serve as the defining boundary of cells, separating the internal cellular environment from the external milieu. These membranes are not just passive barriers but are dynamic structures that play crucial roles in various cellular processes. The fundamental structure and function of cell membranes are intricately linked. Biological membranes

are primarily composed of three structures: phospholipids, cholesterol, and proteins. Phospholipids form the fundamental structural component of cell membranes. These molecules possess a hydrophilic (water-attracting) head and two hydrophobic (water-repelling) tails. The amphipathic nature of phospholipids allows them to spontaneously form bilayers in aqueous environments, with the hydrophilic heads facing the water and the hydrophobic tails oriented inward. There are various types of phospholipids, such as phosphatidylcholine, phosphatidylethanolamine, and phosphatidylserine, each differing in their head group composition[198]. Cholesterol is another crucial component of cell membranes. It is interspersed between phospholipids and modulates the membrane organization. Cholesterol molecules are oriented such that their hydroxyl group aligns with the hydrophilic heads of phospholipids, while the rest of the molecule interacts with the hydrophobic tails. The distribution of cholesterol in membranes can vary, and its presence can lead to the formation of specialized lipid domains known as lipid rafts[199]. Proteins embedded within the cell membrane can be categorized into integral and peripheral proteins. Integral proteins span the entire thickness of the membrane and often serve as receptors or channels. In contrast, peripheral proteins associate with the surface of the membrane, either through interactions with integral proteins or with the polar head groups of the lipid bilayer.

The composition of cell membranes can vary significantly among different cell types. For instance, erythrocytes (red blood cells) have a high concentration of specific proteins like hemoglobin and lack organelles, impacting their membrane composition. In contrast, neurons, with their intricate network of dendrites and axons, have membranes rich in ion channels and receptors to facilitate neurotransmission. Another difference in membrane composition is phospholipid type distribution. Neurons, for instance, are primarily composed of POPC.

The development of force fields tailored for simulating biological membranes has been a focal point in the realm of MD simulations. These force fields aim to capture the intricate interactions and behaviors of lipids, proteins, and other membrane components at the atomic level. The historical development of membrane-specific force fields has its roots in the broader evolution of molecular mechanics force fields. Early force fields were primarily designed for proteins and nucleic acids, with limited parameters for lipids. However, as the significance of lipid bilayers in cellular processes became evident, there was a growing need for dedicated lipid force fields. This led to the development of force fields that could accurately represent lipid-lipid and lipid-protein interactions, paving the way for realistic simulations of biological membranes[200]. One of the primary challenges in accurately

representing membrane interactions lies in the amphipathic nature of lipids. The dual hydrophilic and hydrophobic character of lipids necessitates a force field that can capture both polar and non-polar interactions. Additionally, the dynamic behavior of membranes, such as lipid flip-flop, phase transitions, and interactions with embedded proteins, adds layers of complexity to the simulation[201].

A notable advancement in this field is the introduction of LIPID11[202], a framework designed for lipid simulations within the Amber suite. This framework was developed with a new charge derivation strategy for lipids, consistent with the Amber RESP approach. The LIPID11 framework is modular, making it suitable for phospholipids and offering a flexible starting point for the development of a comprehensive, Amber-compatible lipid force field. This force field has gone through several iterations and improvements, which lead to the current version, LIPID21[203], where its creators have further expanded the parametrized membrane components, revised certain parameters and overall improvements.

The composition of the membrane plays a pivotal role in determining the outcomes of MD simulations. The influence of lipid diversity on membrane properties is profound. Lipids are the primary constituents of membranes, and their diversity can significantly affect membrane fluidity, thickness, and overall behavior. Different lipid species have distinct head groups, tail lengths, and degrees of saturation, which can influence their packing and interactions within the bilayer. For instance, unsaturated lipids tend to introduce kinks in the hydrocarbon chains, leading to increased membrane fluidity[200]. Cholesterol plays a unique and multifaceted role in modulating membrane behavior. It can insert itself between lipid molecules, influencing the packing and ordering of lipids. Cholesterol has been shown to stiffen unsaturated lipid membranes, impacting their mechanical properties. Its presence can modulate membrane fluidity, either increasing it in highly ordered membranes or decreasing it in more fluid membranes[204].

Protein-lipid interactions have a significant impact on simulation outcomes. Membrane proteins can interact with specific lipid species, influencing their conformation, function, and dynamics. These interactions can lead to the formation of lipid shells or annular lipids around proteins, which can affect protein function. Additionally, proteins can induce local deformations in the membrane, leading to curvature or the formation of lipid domains. The presence of proteins can also influence the overall properties of the membrane, including its fluidity and thickness[205]. A notable study highlighted the importance of using realistic membrane compositions in MD simulations. The study demonstrated that altering the compositional complexity of the membrane can impact the stabilization of protein

conformational states. The research emphasized that protein-specific responses to membranes might differ due to altered packing caused by compositional fluctuations[206].

The choice of membrane complexity for MD simulations, particularly the decision to use pure lipid all-atom membranes versus more complex and realistic models, comes with its set of advantages and limitations. Utilizing pure lipid all-atom membranes offers a streamlined system, devoid of the complexities introduced by a more complete lipidic profile, additional proteins, carbohydrates, and other cellular components. This simplification facilitates a clearer understanding of lipid interactions, membrane dynamics, and the fundamental properties of the lipid bilayer without the confounding effects of other membrane constituents[201]. One of the primary challenges in MD simulations is the computational demand, especially for long simulation timescales. Complex membranes, containing a mixture of lipids will take several microseconds to reach dynamic equilibrium, whereas pure lipid membranes take only around 250 nanoseconds[201].

Biological membranes in vivo are complex entities, with a myriad of components interacting in a coordinated manner. Pure lipid membranes lack this cellular context, potentially missing out on important physiological interactions. While pure lipid membranes offer a simplified model, there is a risk of oversimplifying the system to the point where it no longer accurately represents real biological membranes. This can lead to results that, while interesting, might not be directly translatable to in vivo scenarios. This is an inevitable overall limitation of MD simulations, which highlights the need for wet lab experimental validation of results and observations derived from computational efforts – even more when these were obtained using simplified models.

2.2. Enhanced sampling techniques

Molecular dynamics (MD) simulations have inherent limitations when it comes to protein conformational exploration. As we saw in the previous chapter, an MD simulation of a protein system will explore – given infinite time – all protein configurations, conformations, and even metastable states, if and only if, they are accessible through structural thermal fluctuations. There is no inward flow of energy into the system other than the effect of the chosen thermostat at the determined temperature, so any biological event with an energetical barrier higher than that provided by thermal fluctuations will be extremely unlikely to occur in the simulation. Although some biological events, albeit energetically accessible, are so rare that could, maybe, be observed in simulations after an unsurmountable amount of computer-hours – making them virtually inaccessible.

Expectedly, a significant number of biologically relevant phenomena under computational investigation are inaccessible to equilibrium MD simulations, a need which gave rise to the field of enhanced sampling methods – also known as out-of-equilibrium MD simulations (within the present context). These tools accelerate the elucidation of slow biological processes, hastening the infrequent events typified by high free-energy states. Put differently, enhanced sampling techniques endeavor to circumvent Boltzmann statistics, yet maintain the accurate distribution of states within the specified statistical ensemble[207].

There are primarily two distinct categories of enhanced sampling methodologies[208]. The first category, termed global enhanced sampling methods, operates by elevating all the degrees of freedom of the system (or a subset thereof) simultaneously. It is imperative to emphasize that the term "temperature" should be interpreted metaphorically, as the increase in sampling can be achieved either through literal thermal elevation of the system or through judicious scaling of the energy of the system. Temperature replica exchange MD (T-REMD, also known as "parallel tempering")[209–211] is an example of this class.

The second category encompasses methods guided by collective variables (CVs). These methods facilitate the reconstruction of the free energy landscape of the subject phenomena based on a specific CV, often referred to as a reaction coordinate. This reaction coordinate effectively captures the pertinent degrees of freedom associated with the phenomena under investigation. Techniques within this category enable the probing of infrequent events by introducing biases to MD simulations along the designated CVs. This biasing can be implemented through various means, including modulating the forces or introducing external potentials. Consequently, CV-driven techniques necessitate an initial determination of the reaction coordinate for sampling. In many instances, delineating an appropriate

CV (or a set thereof) is non-trivial. It often demands considerable insight and/or preliminary simulations to ensure a comprehensive representation[208]. Examples include metadynamics[212] and OPES[213].

2.2.1. What are collective variables?

One of the most important concepts that I previously mentioned is that of collective variables, which I believe is easier to fully understand with an example. Take a researcher interested in understanding the free energy profile of the binding and unbinding of a cation to its binding site within a protein, as shown in **Figure 4.A**. If they were to run equilibrium MD simulations of this system the cation would succinctly lose itself in the solvent in the great majority of cases, and perchance, in an occasional simulation the cation would find its way to its binding site. A much better and practical approach would be to run an out-of-equilibrium simulation, where the MD simulation would repeatedly sample the cation binding and unbinding. In this specific case, an appropriate reaction coordinate would be the distance between the cation and the center of mass of the residues composing the binding site (distance D in **Figure 4.A**). The researcher could then run a metadynamics simulation over this distance, our chosen CV.

The core concept of metadynamics revolves around biasing the dynamics of the system along selected collective variables (CVs) through a history-dependent repulsive potential. To realize this, Gaussian-shaped potentials are periodically introduced to the bias at the present location of the CVs. This strategy deters the system from retracing previously visited spatial regions[212,214]. Over time, this history-dependent potential accumulates until it offsets the projection of the free energy along the designated CVs. Consequently, the system can transition through a saddle point to an adjacent local minimum, at which point the process recommences. Once all local minima are populated with Gaussians, the system traverses freely among various states without encountering barriers. The accumulated bias potential can subsequently serve as an unbiased estimator of the potential of mean force (PMF) by merely inverting its sign[208].

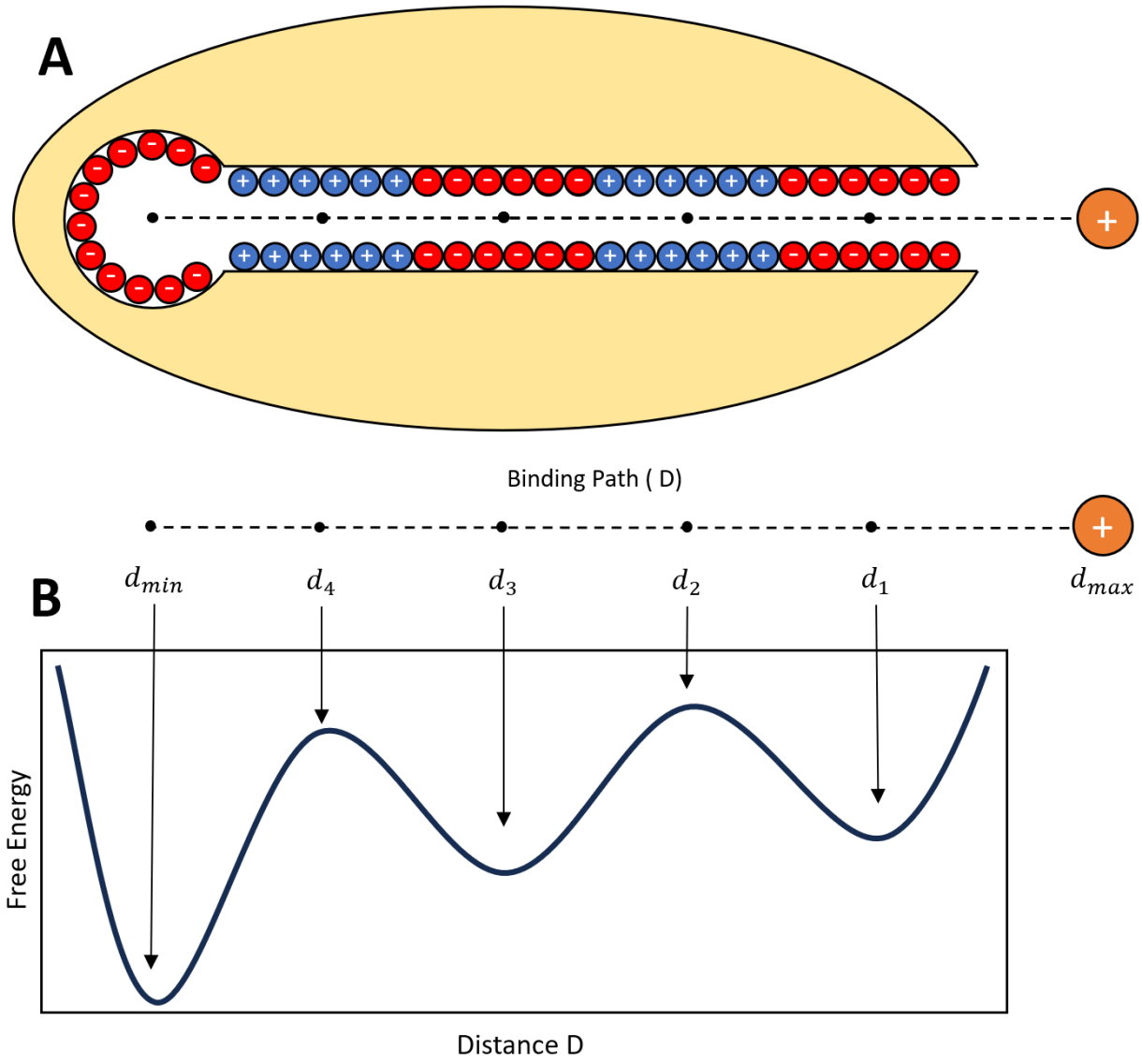

Figure 4. Simplified example of a collective variable. **(A)** Shows a schematic representation of a cation binding protein (light yellow), with negatively charged amino acids (red spheres with a – sign), and positively charged amino acids (blue spheres with a + sign). The discontinuous line shows the binding path (or distance D), and below the yellow protein a more detailed representation of the binding path is shown, where the black dots are given names. **(B)** Schematic representation of the potential free energy profile for such a system, showing potential minima and maxima along the binding path collective variable.

In the scenario presented by our researcher, the cation initiates its journey from a distance of d_{max} and progresses towards d_{min}. Upon reaching d_1, the cation encounters a negatively charged environment, which, for the sake of this simplified illustration, can be perceived as a local energy minimum. This minimum is subsequently populated with a Gaussian-shaped biasing potentials. Once this minimum is saturated, the cation is energetically encouraged to advance along the binding trajectory, surmounting the saddle point at d_2, a region of positive charge that would typically repel

the cation. This facilitates its transition to the subsequent energy minimum at d_3, another negatively charged domain. After this minimum is populated with the biasing potential, the cation is equipped to transcend the energy barrier presented by the positively charged zone at d_4. Surpassing this barrier enables the cation to reach its terminal binding site, denoted as d_{min} in the CV space. Once a sufficient biasing potential is introduced to d_{min}, the cation can oscillate between binding and unbinding, transitioning between d_{max} and d_{min}, given that all the energy minima along its path have been previously filled with Gaussians. By analyzing the accumulated Gaussians, our researcher can deduce the free energy landscape associated with the binding and unbinding processes of the cation, akin to the representation in **Figure 4.B**.

2.2.2. On-the-fly Probability Enhanced Sampling (OPES) Explore, the new metadynamics for complex protein systems?

The challenge of sampling is central to atomistic simulations. Even the most precise models can fall short if the phase space is not adequately sampled. This sampling challenge arises from the vast gap between macroscopic physical timescales and the actual time explored in standard atomistic simulations. One aspect of this challenge is the existence of metastable states separated by kinetic bottlenecks, making transitions between states a rare event. Enhanced sampling methods offer a solution by creating a modified ensemble where the probability of sampling rare events is significantly increased[215].

As we briefly introduced in the previous chapter, metadynamics is a renowned enhanced sampling method that focuses on the on-the-fly construction of a bias potential based on a selected set of collective variables. The recent publication of On-the-fly Probability Enhanced Sampling (OPES) introduced a new perspective, which emphasizes the reconstruction of the probability distribution rather than the bias[213].

In adaptive-bias enhanced sampling methods, a bias potential is added to the system to facilitate transitions between metastable states. This bias potential is a function of a few collective variables and is progressively modified according to the underlying free energy surface. However, when the collective variables are not optimal, there exists an exploration-convergence tradeoff. This tradeoff means that one must choose between a bias that converges quickly, leading to fewer transitions, or a slower-to-converge bias that can explore the phase space more efficiently but might take a longer time to produce an accurate free energy estimate[215]. The recently developed OPES can be adapted to

address this exact problem. OPES, initially introduced as an evolution of metadynamics, can provide similar enhanced sampling but typically exhibits faster convergence and requires fewer adjustable parameters, when compared to metadynamics. When applied to sample expanded ensembles, OPES retains these properties, making it a versatile and reliable method for sampling various ensembles[213].

The traditional OPES method is designed with a focus on fast convergence. However, there are scenarios where rapid exploration is more desirable than swift convergence. Recognizing this need, a new variant of the OPES method, termed OPES Explore[216], has been introduced. The primary advantage of this approach is its ability to navigate the phase space efficiently, especially in systems where the collective variables might not be optimal. OPES Explore is designed to quickly escape metastable states, making it particularly effective in systems where transitions between states are rare or challenging. The method has been shown to outperform popular methods like metadynamics in certain scenarios, showcasing its potential as a versatile enhanced sampling tool[215].

In other words, while both OPES and OPES Explore are adaptive-bias enhanced sampling methods, their primary objectives differ. Traditional OPES focuses on fast convergence to produce accurate free energy estimates in a shorter time. In contrast, OPES Explore prioritizes efficient exploration of the phase space, even if it means slower convergence. OPES might be more suitable for systems where the collective variables are well-defined and optimal, ensuring swift convergence. On the other hand, OPES Explore can be more beneficial in systems with suboptimal collective variables, where efficient exploration is crucial.

Chapter 3:
Structure and molecular dynamics simulations of the human cation-chloride cotransporter KCC1

3.1. Abstract

Cation–chloride cotransporters (CCCs) mediate the electroneutral co-transport of Cl^- ions concomitantly with Na^+ and/or K^+ ions across cellular membranes. These cotransporters play pivotal roles in the regulation of cellular volume, transepithelial ion flux, intracellular Cl^- ion concentration equilibrium, and modulation of neuronal excitability. In our publication[35], with our collaborators, we presented a cryoelectron microscopy structure of human K^+–Cl^- cotransporter (KCC)1 bound with the VU0463271 inhibitor in an outward-open state alongside KCC1 in an inward-open state. In the following chapter, I will show the computational insights molecular dynamics can give to crystallographers.

3.2. Introduction

Secondary active cation–chloride cotransporters (CCCs) utilize the Na^+ and/or K^+ ionic gradients present across all animal cellular membranes to facilitate Cl^- ion transport into or out of cells without net charge movement[4,217]. These CCCs are integral to several physiological functions, including transepithelial ion transport, cellular volume regulation, control of intracellular Cl^- ion concentration ($[Cl]_i$), and modulation of neuronal activity[218–221]. For instance, when faced with a hypotonic environment, K^+–Cl^- cotransporters (KCCs) actively transport Cl^- and K^+ out of the cell, preventing cellular swelling by inducing concurrent water efflux[222,223]. In the majority of mature neuronal cells, KCC2 acts as the primary mechanism for Cl^- expulsion, ensuring that $[Cl]_i$ remains below its electrochemical equilibrium. This facilitates inhibitory neurotransmitters like γ-aminobutyric acid [GABA] to induce Cl^- entry through pentameric ligand-gated Cl^- channels, resulting in cellular hyperpolarization[224]. Consequently, genetic mutations in KCC2 (or KCC3) have been linked to various neurological disorders, including epilepsy, autism, and schizophrenia[66,100,101,104,105,116,117,225]. This positions KCCs as potential therapeutic targets, not only in the nervous system but also in non-excitable cells. In fact, KCC activators have been employed to reinstate inhibitory GABAergic signaling in several neuropsychiatric conditions[224,226–230]. On the other hand, suppression of KCC activity in erythrocytes has demonstrated potential in mitigating the dehydration typical of sickle cells, offering a prospective treatment approach for sickle cell anemia[231,232]. Additionally, NKCC2 and NCC, two renal CCC variants, are targeted by loop and thiazide diuretics for the management of hypertension and fluid retention[233,234], though these treatments can sometimes lead to adverse effects like auditory impairment[235,236].

Here we investigated the two cryoelectron microscopy (cryo-EM) structures that represent human KCC1 trapped in an inward-open state or arrested in its elusive outward-open state by the KCCs inhibitor VU0463271[45,237]. Based on several molecular dynamics simulations of these new structures, we show that the inhibitor VU0463271 stabilizes the outward-open state, ion loading is synergistic and we revealed a putative occluded state of KCC1.

3.3. Results

Classical molecular dynamics (MD) simulations were performed on five model systems of KCC1: 1) outward–open structure bound to the inhibitor VU0463271 (system **OO_VU**); 2) outward–open without bound inhibitor (**OO**); 3) inward–open with one K^+ ion bound (**IO_K**); 4) inward–open with one K^+ and two Cl^- ions bound (**IO_KCC**); 5) outward–open with one K^+ and two Cl^- ions bound (**OO_KCC**).

The VU0463271 inhibitor stabilizes the outward–open conformation. The **OO_VU** model equilibrated within the first 50 ns simulation, with the RMSD distance of the secondary structure elements from the initial structure settled at ~2 Å (**Figure 5**). The inhibitor VU0463271 maintained the experimentally determined binding pose throughout the 500 ns long MD simulation. After about 400 ns simulation, a small shift of extracellular end of TM6, which constitutes part of the binding site of the inhibitor, was observed, accompanied by an increase of the RMSD to 2.5 Å. This shift did not alter the binding mode of VU0463271 nor the volume of the outer vestibule, which maintained an open conformation (**Figure 6.A, B**). After the removal of the inhibitor (simulation **OO**), the outer vestibule started to shrink (**Figure 6.C, D**) – please note that the binding site was filled by solvent molecules before letting the protein to move again, which is good-practice in order to let the system equilibrate. Despite difficult to appreciate from the RMSD graph (**Figure 5**), the structure indeed changed after removal of the inhibitor. A clustering analysis performed on the cumulative trajectory of the **OO_VU** and **OO** simulations allowed distinguishing intermediate conformations corresponding to different openings of the outer vestibule (**Figure 7**). Interestingly, the outward–open structure is not reverting to the inward–open conformation (**Figure 5** orange line), upon removal of the inhibitor. Longer simulations are likely needed to investigate the relaxation of the outward–open conformation and assess the stability of intermediate conformational states.

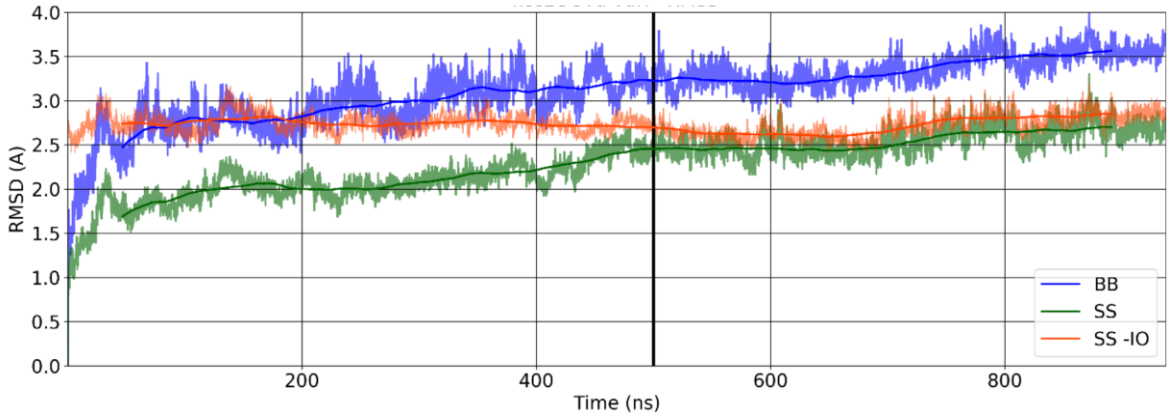

Figure 5. Root-mean square deviation (RMSD) of the simulations of the OO_VU and OO models. The vertical black bar at 500 ns indicates the start of the simulation after removal of the inhibitor. RMSD of the backbone of the full transmembrane domain in blue (BB). RMSD of the backbone of the transmembrane helices in green (SS). RMSD of the backbone of the transmembrane helices calculated against the initial KCC1 K-bound structure in orange (SS-IO).

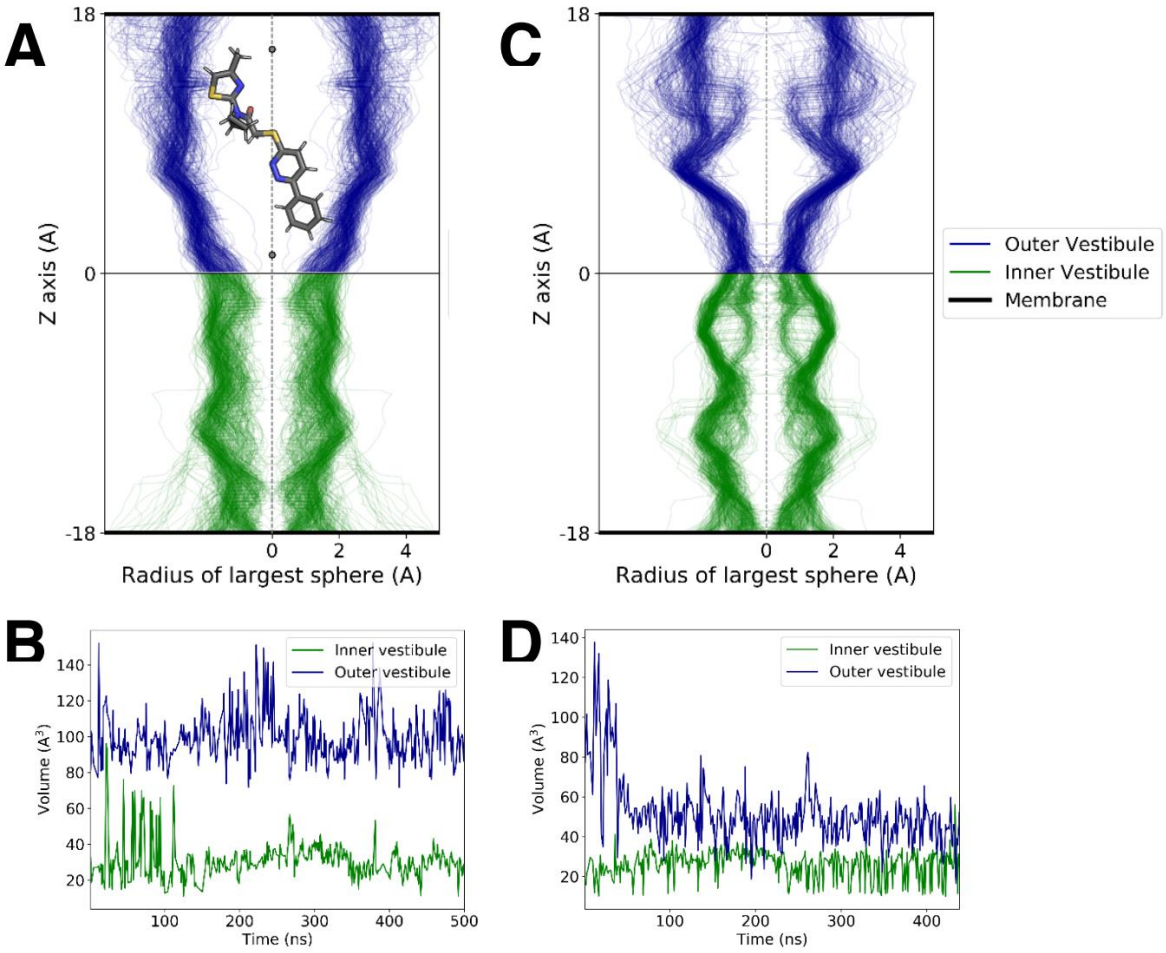

Figure 6. Representation of the width of the transport path during the simulation of the **(A) OO_VU** model, VU representation is to scale (grey spheres mark the Z axis range occupied by the inhibitor), and the **(C) OO**

model. Volume of the inner and outer vestibules during the simulation of the **(B) OO_VU** model, and the **(D) OO** model, upon removal of the inhibitor from its binding site.

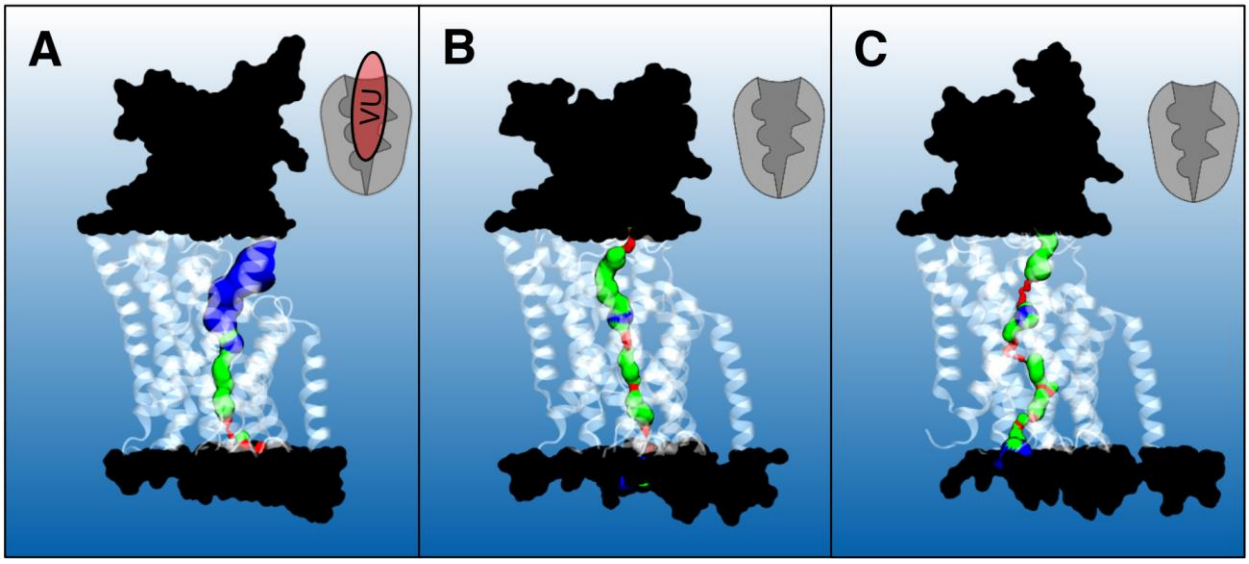

Figure 7. The cumulative **OO_VU** and **OO** MD trajectories were grouped based on RMSD similarity. Three groups (clusters) were detected, whose representative structures are shown. The transport path is highlighted and colored depending on channel width (red color implies that the pore radius is too narrow to allow a water molecule to pass; green implies that there is enough space for one water molecule to pass; and blue implies there is at least double the space necessary for a single water molecule to go through). Cluster **A** shows a wide outer vestibule, congruent with the presence of a bound inhibitor. Cluster **B** is formed when VU is removed from the simulation, and it represents a stage where the outer vestibule is closing. Cluster **C** represents a section of the simulation where the outer vestibule is at its narrowest state, along the MD simulations in the absence of the inhibitor.

Ions loading is synergistic. The MD simulations of model **IO_K** show a stable inward–open conformation. The RMSD of the transmembrane helices settles after about 50 ns and remains at ~1.5 Å throughout ~500ns of production simulation (**Figure 8.A**). We observed the K^+ ion leaving its binding site and exiting the intracellular vestibule after ~15 ns. A similar behavior was reported by a recent report on KCC1[33], suggesting that in the absence of the Cl^- counter ions, K^+ binding is short lived. However, the exit of the K^+ ion does not affect the structure of the transporter, which apparently does not require any ligand to maintain the inward–open conformation (**Figure 8.B**). Indeed, when the Cl^- anions are present, the residence time of K^+ increased. In the inward–open conformation (simulation **IO_KCC**), the three ions remain bound for ~220ns (**Figure 9.A**), a comparable timespan to that found in previous simulations[33]. After ~220ns, Cl1 (see **Figure 9.C**) leaves the binding site and exits the intracellular vestibule towards the cytoplasm. This event destabilizes K^+, which experiences larger fluctuations in the binding site (**Figure 9.A**), ultimately resulting in the exit of this ion from the intracellular vestibule after ~450ns. Thus, the lifetime of Cl1 and K^+ in their respective binding sites

seems highly correlated, as previously suggested[33]. Cl2, on the other hand, remained stably bound to its binding site throughout the simulations, even after the unbinding of Cl1 and K^+. This finding is also in line with what was previously described[33]. Notably, the overall structure of the transporter did not change upon different ion occupancy, stably maintaining the inward–open conformation (**Figure 9.B, C**).

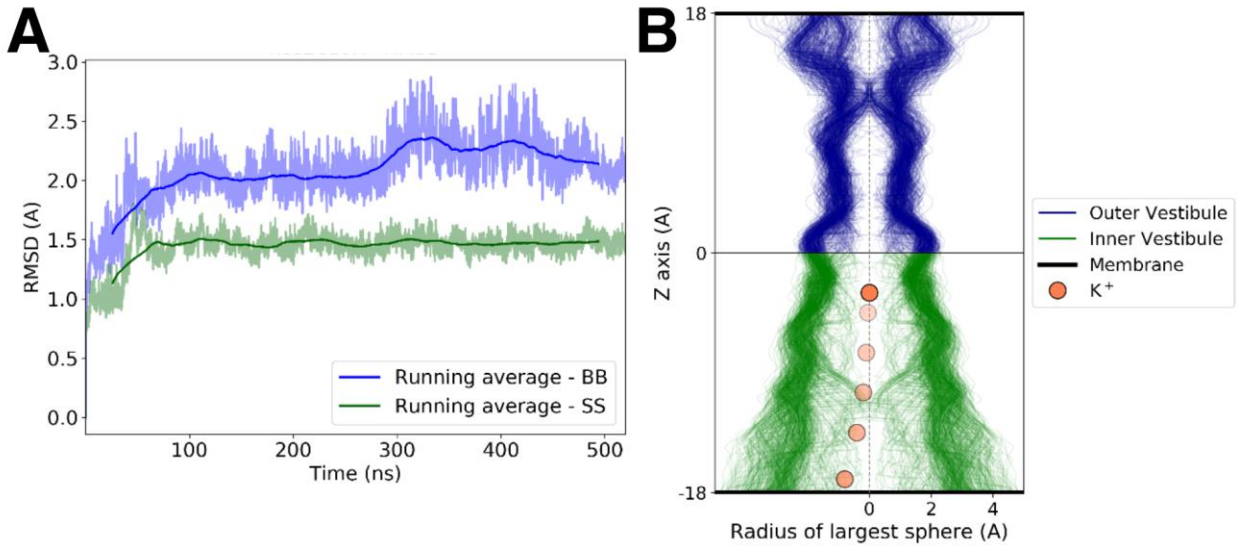

Figure 8. (A) RMSD during the simulations of the **IO_K**. RMSD of the backbone of the full transmembrane domain in blue (BB). RMSD of the backbone of the transmembrane helices in green (SS). **(B)** Representation of the width of the transport path during the simulation of the **IO_K** model. The opaque orange sphere indicates the initial position of the bound K^+, and transparent spheres represent the exit pathway of K^+.

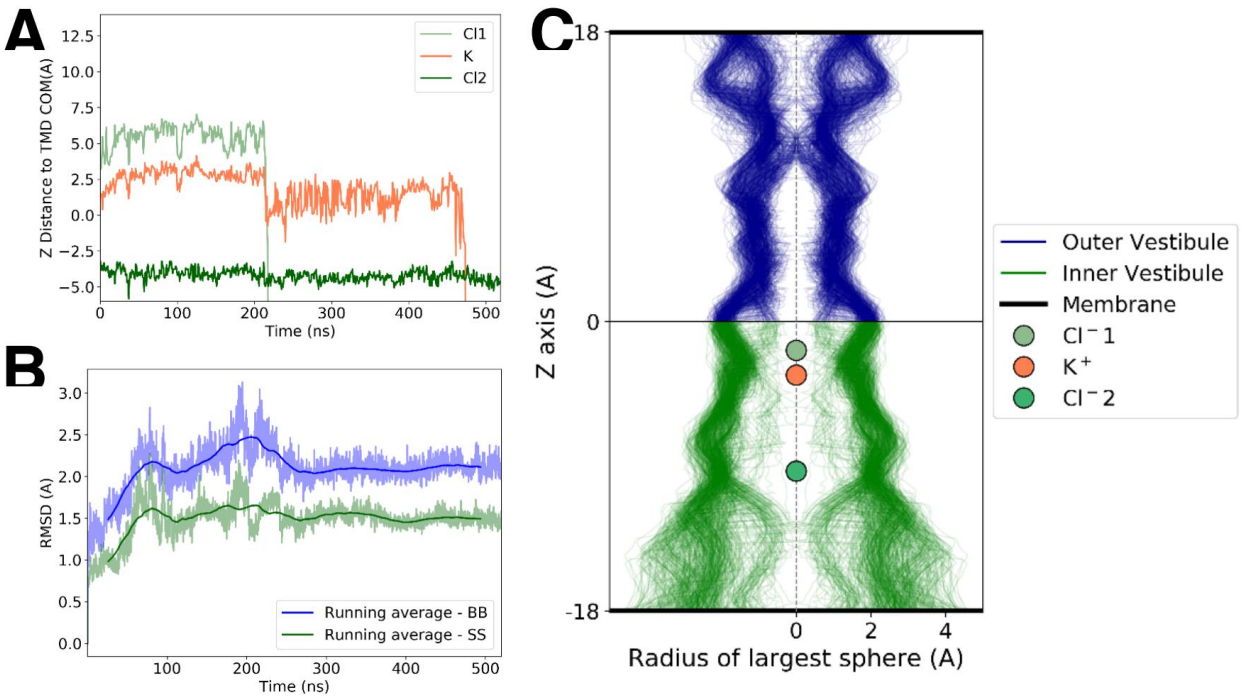

Figure 9. (A) Position of the ions along the axis perpendicular to the membrane bilayer during the simulation of the **IO_KCC** model. **(B)** RMSD of the **IO_KCC** model during the MD simulation. RMSD of the backbone of the full transmembrane domain in blue (BB). RMSD of the backbone of the transmembrane helices in green (SS). **(C)** Representation of the width of the transport path during the simulation of the **IO_KCC** model. Green and orange circles represent initial positions of bound Cl and K, respectively. Cl1 is closest to the extracellular side, and Cl2 is closest to the intracellular side.

MD simulations reveal a putative occluded state. We also investigated the ions binding in the outward–open conformation. Simulations of the **OO_KCC** model displayed a different behavior compared to **IO_KCC**. All bound ions remained in their binding sites for the whole duration of the simulation (500ns) (**Figure 10.A**). Notably, Cl1 attempted to move towards the extracellular side in the 100–200ns window of the simulation time, but then settled again stably in its original binding site. Only then, the secondary structure RMSD started stabilizing (**Figure 10.B**), and the volume of the outer vestibule started decreasing (**Figure 10.C, D**). The closing of the extracellular vestibule was also observed in the OO model (see above) once the inhibitor was removed from its binding site. This is here more severe, decreasing to levels seen in the IO conformation. The result of this simulation is a state in which the three binding sites are inaccessible to the solvent, indicative of an occluded state.

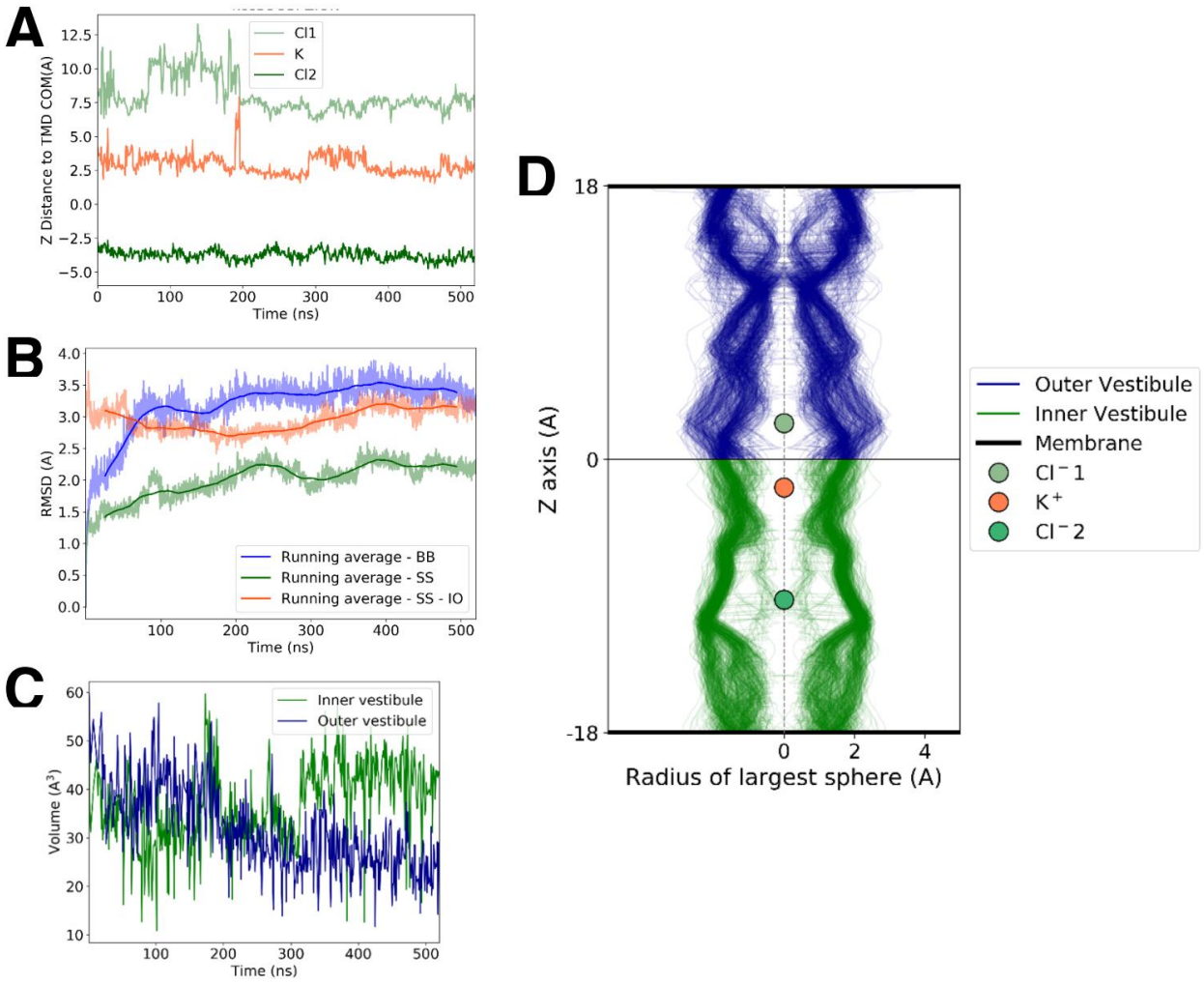

Figure 10. (A) Position of the ions along the axis perpendicular to the membrane bilayer during the simulation of the **OO_KCC** model. **(B)** RMSD of the **OO_KCC** model during the MD simulation. RMSD of the backbone of the full transmembrane domain in blue. RMSD of the backbone of the transmembrane helices in green. RMSD of the backbone of the transmembrane helices calculated against the initial KCC1 K-bound structure in orange. **(C)** Volume of the inner and outer vestibule during the simulation of the **OO_KCC** model. **(D)** Representation of the width of the transport path during the simulation of the **OO_KCC** model. Green and orange circles represent initial positions of bound Cl and K, respectively. Cl1 is closest to the extracellular side, and Cl2 is closest to the intracellular side.

3.4. Discussion

Our classical MD simulations of the newly obtained KCC1 in both the inward-open and outward-open state, allowed for several relevant conclusions. For instance, we observed that the VU0463271 inhibitor stabilizes the outward-open conformation of the KCC1 structure. Simulations reveal that the removal of VU0463271 causes the KCC1 structure to deviate from the outward-open conformation, without adopting the inward-open conformation, indicating the likelihood of an intermediary, possibly occluded, state being sampled. Additionally, the loading of ions is found to be synergistic, as simulations demonstrate a correlation between Cl1 and K^+ binding. The unbinding of one of these ions precipitates the unbinding of the other, and the absence of Cl2 results in the swift unbinding of K^+. This synergy and the observed structural transitions provide insights into the dynamic behaviors and regulatory mechanisms of the KCC1 structure in the presence and absence of inhibitors and ions.

3.5. Methods

Models included only the transmembrane domain (comprising residues 116-661) of one KCC1 monomer embedded in a POPC bilayer. Models **IO_K** and **IO_KCC** were based on the experimentally determined structures of KCC1[35] in the inward–open conformation bound to K^+, while models **OO_VU** and **OO_KCC** were based on the experimentally determined structure of KCC1[35] in the outward–open conformation bound to inhibitor VU0463271. The location of chloride ions in models **IO_KCC** and **OO_KCC** were determined from a previously published structure of KCC1 (PDB code: 6KKR) after alignment of the residues composing the ions binding sites. Model **OO** was generated by removing the inhibitor from the last snapshot of a 500 ns long MD simulation of model **OO_VU.** Before starting the simulation without VU0463271, the space previously occupied by this inhibitor was filled with water molecules. An extracellular loop between helices TM3 and TM4, missing in the experimental structure of the transporter/inhibitor complex, was modelled using Modeller[162,238]. The outward–open experimental structure also lacked six residues at the cytoplasmic end of TM12. Since this helix was solved in the inward–open structure, the coordinates of the missing residues were transferred from this structure after alignment of the terminal segment of the helix. The ionization state of titratable residues was determined using PropKa 3.0 assuming pH 7[239]. The simulation cells included the transporter and its ligands (if any), together with 359 POPC molecules, 84 Cl, 86 K ions (in the bulk solution, corresponding to about 150 mM concentrations) and 31224 water molecules (~ 150,300 atoms in total for a simulation box of ~112 x 112 x 121 $Å^3$ size). Initial

configurations of each simulation cell were assembled using Packmol-Memgen[240], part of the AmberTools software package.

MD simulations were performed with the GPU version of the PMEMD code[241] of the AMBER package[242]. The ff14SB force field was used for the protein[243], Lipid17 for the POPC bilayer[244], TIP3P for water[179] and for the ions[245]. The system was treated under periodic boundary conditions, using the particle mesh Ewald[246] method to compute long-range electrostatics. A 10 Å cutoff was used for the real part of the electrostatic and for van der Waals interactions. The SHAKE algorithm was used to constrain bonds involving hydrogen atoms[170], allowing an integration time step of 2 fs. Simulations were performed at constant temperature (310 K) and pressure (1 bar). The POPC bilayer and water solvent were allowed to equilibrate around the protein during 200 ns of MD simulations. After energy minimization, the system was gradually heated to 310 K, maintaining the protein backbone close to the crystallographic positions by applying a harmonic restraint. Then, about 500 ns of production MD were performed for each model. A clustering analysis was performed based on the density of data points[247]. Radius of largest sphere was determined with HOLE[248].

Chapter 4:
The cation-chloride cotransporter NKCC1 operates through a rocking-bundle mechanism

4.1. Abstract

The sodium, potassium, chloride cotransporter 1 (NKCC1) plays a key role in tightly regulating ions shuttling across cell membranes. Lately, its aberrant expression and function have been linked to numerous neurological disorders and cancer, making it a novel and highly promising pharmacological target for therapeutic interventions. A better understanding of how NKCC1 dynamically operates would therefore have broad implications for the several ongoing efforts toward its exploitation as a therapeutic target through its modulation. Based on recent structural data on NKCC1, we reveal conformational motions that are key to its function. Using extensive deep learning-guided atomistic simulations of NKCC1 models embedded into the membrane, we captured complex dynamical transitions between alternate open conformations of the inner and outer vestibules of the cotransporter and demonstrate that NKCC1 has water permeable states. We found that these previously undefined conformational transitions occur *via* a rocking-bundle mechanism characterized by the cooperative angular motion of transmembrane helices (TM) 4 and 9, with the contribution of the extracellular tip of TM 10. We found these motions to be critical in modulating ion transportation, and in regulating the water transporting capabilities of NKCC1. Specifically, we identified inter-helical dynamical contacts between TM 10 and TM 6, which we functionally validated through mutagenesis experiments of four new targeted NKCC1 mutants. We conclude showing that those four residues are highly conserved in most Na^+-dependent cation chloride cotransporters (CCCs), which highlights their critical mechanistic implications, opening the way to new strategies for function modulation of NKCC1 and thus to potential drug action on selected CCCs[249].

4.2. Introduction

The cation chloride cotransporter (CCC) NKCC1 is a modulator of intracellular Cl^- concentration in diverse cell types, in numerous body organs. Particularly, NKCC1 is expressed in parenchymal brain cells, where it regulates intraneuronal Cl^- concentration which in turn is crucial for the modulation of the function of the neurotransmitter GABA[84]. In the majority of cell types, NKCC1 uses an inward-directed Na^+ gradient to import Na^+, K^+ and Cl^-, in a 1:1:2 stoichiometry. NKCC1 is also highly expressed on the apical membrane of the choroid plexus, where it plays a major role in producing and regulating cerebrospinal fluid (CSF). Importantly, in recent years, extensive research has shown that an increased intracellular Cl^- concentration in neurons is symptomatically related to multiple neuropathologies and also glioblastoma, along with the growing body of literature showing the important pathological role of NKCC1 in increased CSF production[6,155,250–252]. Accordingly, normalization of intracellular Cl^- concentration and of CSF hypersecretion in the brain by modulation of CCC (including NKCC1) functions is considered a very promising strategy for neuroscience drug discovery[130,144,148,155,250]. A fundamental understanding of the structure, dynamics and overall conformational motions of NKCC1 for ion passage may therefore open new avenues for therapeutic interventions on many human disorders ranging from brain and hearing to kidney and cancer diseases.

Interestingly, 15 NKCC1 structures have been recently resolved alone or together with unselective inhibitors (e.g., the FDA-approved diuretic bumetanide). All these recent cryo-EM structures of NKCC1 have clarified several functional features of its multidomain system[32,34,38,44,253], revealing a structural similarity to the LeuT-fold transporters[23,254]. In particular, NKCC1 is a homodimer, where each monomer is constructed by three main components: a conserved transmembrane (TM) domain, composed of 12 helices organized in two inverted repeats of five-helix bundles, which contain all four ion binding sites (**Figure 11.A**). Two additional intracellular domains are the disordered amino-terminal and the large carboxy-terminal domains, which are related to NKCC1 activation (**Figure 11.B**)[34].

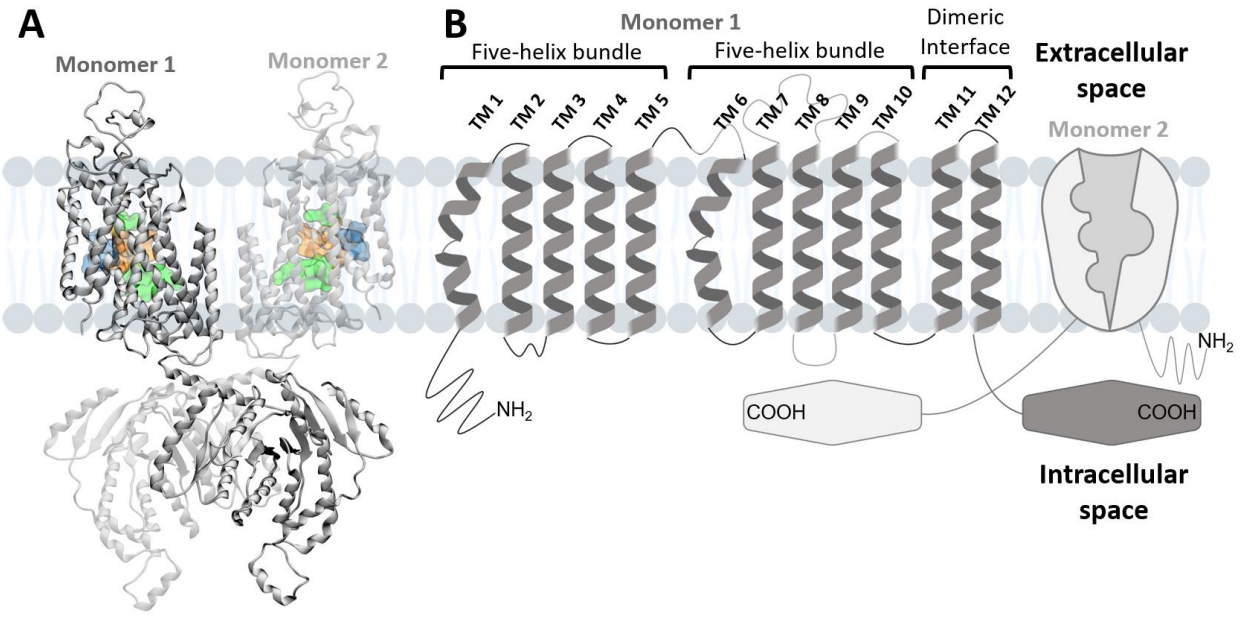

Figure 11. NKCC1's structure embedded in the membrane. **(A)** 3D representation of full length *human* NKCC1 (PDB 7MXO), with each monomer represented in dark and light grey. Each monomer is constructed by three main components: i) a conserved TM domain, composed of 12 helices, which contains all four ion binding sites, shown in green, blue and orange for Cl^- , Na^+ and K^+ ions, respectively; ii) the disordered amino-terminal; and iii) the large carboxy-terminal domains[34]. All structures of NKCC1, and related CCCs of the same family[41], revealed that the TM helices are organized in two inverted repeats of five-helix bundles – also known as LeuT-fold[11,23,254,255]. **(B)** Schematic representation of NKCC1, showing its homodimeric structure with one monomer represented to highlight the transmembrane domains (TMs, dark grey); the other monomer represented to highlight the channel arrangement across the cell membrane (light brown); the two five-helix bundle inverted repeats (TM 1 to TM 5 and TM 6 to TM 10) and the dimeric interface (TM 11 and TM 12). The amino and carboxy terminal domains are also highlighted.

The NKCC1 structures recently resolved have also confirmed that NKCC1 operates transiting from conformations where the ion binding sites are exposed either to the extracellular or to the intracellular side of the membrane[255]. That is, NKCC1 must transit dynamically through two distinct conformational states: an outward open (OO) state, in which the transporter binds to ions from outside of the cell, and an inward open (IO) state, in which the protein releases the ions to the inside of the cell (**Figure 12**). However, the mechanism for the IO ↔ OO conformational transitions in NKCC1 is unclear.

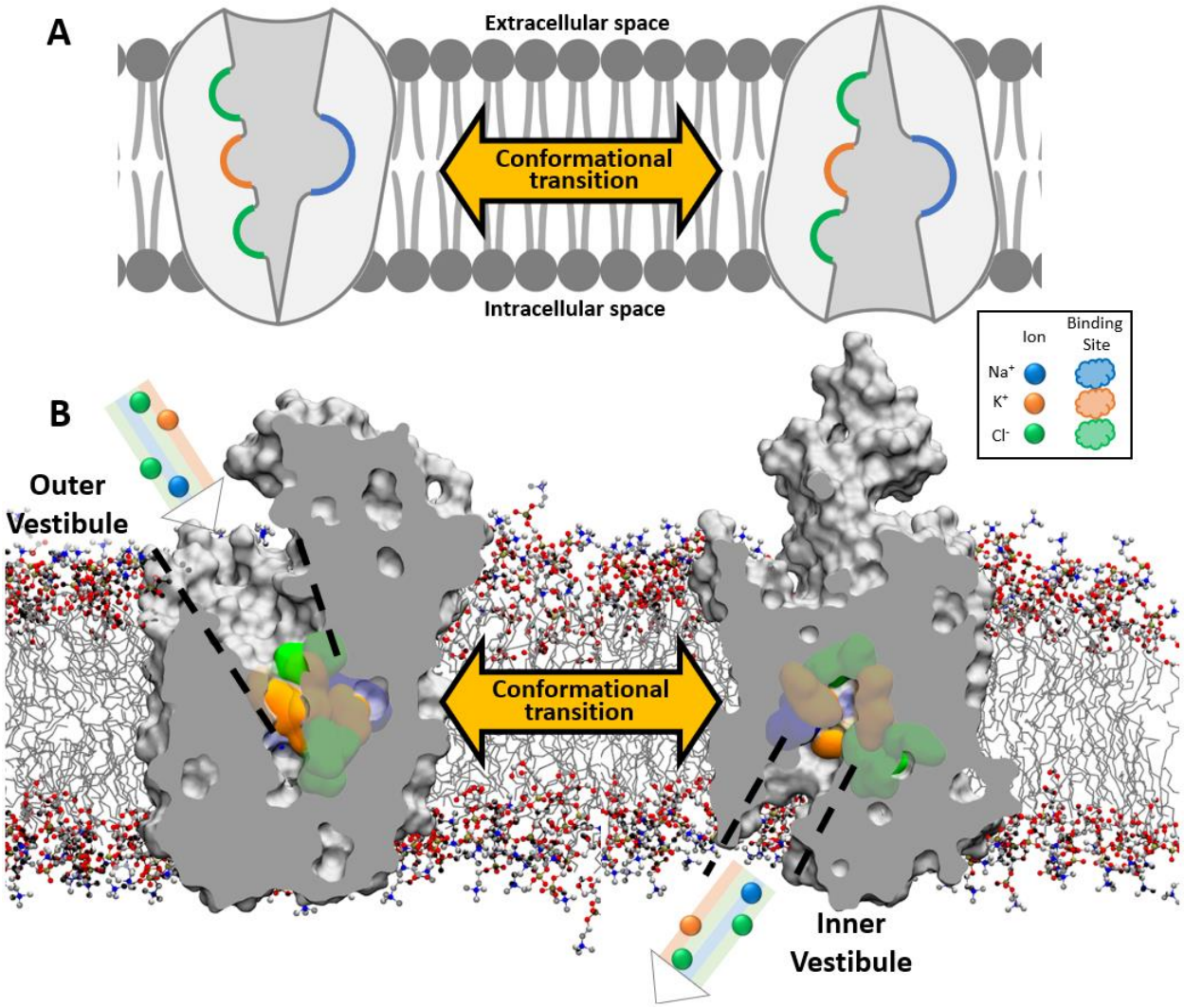

Figure 12. An essential conformational transition for alternating accessibility of ion binding sites allows NKCC1 ion transport. **(A)** Schematic representation of Outward Open (left) and Inward Open (right) NKCC1 conformation. Ionic binding sites are exposed to the extra and intracellular side of the membrane, respectively. **(B)** In gray, atomic surface representation of Outward Open (left) and Inward Open (right) NKCC1 conformation. Ionic binding sites for Na^+, K^+, and Cl^- are shown as colored surfaces (blue, orange, and green, respectively), and ions are represented as colored spheres. Outer (left) and inner (right) vestibules, open to the extra and intracellular sides of the membrane, are highlighted with discontinuous black lines.

In this context, we have explored here different molecular mechanisms for IO ↔ OO conformational transitions in NKCC1 and ions transport in NKCC1 embedded in the membrane. To do so, we have used extensive classical equilibrium molecular dynamics (MD) simulations and deep learning-guided enhanced sampling free energy calculations[216,256]. We also validated our *in-silico* evidence by biological functional studies in cell cultures with targeted NKCC1 mutagenesis. Combining our molecular modeling and molecular biology experiments, we clarified the complex IO ↔ OO conformational

transition in NKCC1 and revealed that it operates through a rocking-bundle mechanism. In addition, we have identified specific inter-helical dynamical contacts that we have found to be fundamentally involved in the transport cycle of NKCC1, favoring also water diffusion through the transporter. Based on structural similarities and biochemical data analyses, we propose that our findings could be extended to all Na^+-dependent CCCs.

4.3. Results

4.3.1. NKCC1 operates *via* a rocking-bundle mechanism for conformational transitions

To investigate the mechanism of the NKCC1 ion transporter, we ran extensive classical molecular dynamics (MD) simulations coupled to on-the-fly probability enhanced sampling (OPES) method to handle elaborated deep learning-derived collective variables (CVs) needed to capture complex dynamical phenomena[213,216] and accelerate a meaningful sampling of the underlying conformational space. Notably, these simulations of atomistic models embedded into the membrane were grounded on the recently resolved human NKCC1 structures. Specifically, our realistic models were based on the structure of the Inward Open (IO) state[34] and a partially loaded Outward Open (OO) state of NKCC1 (**Figure 12.B**)[44]. We initially focused on NKCC1 model systems in which ions bound at the vestibules are absent (i.e., the ions' external gates at the transporter, see **Figure 12**). This setup allowed focusing our exploration on the mechanistic transitions between the IO ↔ OO NKCC1 conformations. As a result, we could sample 16 IO ↔ OO conformational transitions (**Appendix Figure SI 4**) and collected over ~2 μs of trajectories from a total of 3 independent enhanced sampling simulations, in addition to ~2.5 μs of equilibrium MD runs.

There are diverse alternating access mechanisms that could allow NKCC1 to shuttle ions inside the cell, passing across the cell membrane[11,255]. For example, the 'rocking bundle' or the 'elevator' mechanism are equally plausible alternating mechanisms for ions transport across the membrane. Significantly, these distinctive alternating mechanisms differ in the active motions of specific transmembrane (TM) helices, which must assist the dynamical passage of ions. The IO ↔ OO conformational transitions observed in our simulations revealed that NKCC1 operates through the 'rocking-bundle mechanism'[257]. In particular, our computational evidence shows the exact protein motions for NKCC1's function, clarifying which specific dynamics operates within the general 'alternating access mechanism'. We found indeed that the inner and outer NKCC1's vestibules alternate their accessibility using the rocking-bundle mechanism for NKCC1 characterized by the motion of TM helices TM 4 and TM 9. In fact, both TM 4 and TM 9 stably maintained their initial structure for over ~1 μs in both IO and OO states during our equilibrium MD, with an average root mean square deviation (RMSD) of 0.68 ± 0.14 Å and 0.72 ± 0.11 Å, respectively. However, in all the 16 IO ↔ OO transitions (**Figure 13.B**), these TM helices showed a concerted angular motion, with a rotation of at most 14° with respect to the intracellular extreme of TM 2 and TM 7 - both located

within the *static* domain formed by TM 1, TM 2, TM 6 and TM 7 of NKCC1 (**Figure 13.A**), which is used for structure alignment. The RMSD of TM 4 and TM 9, in the IO and OO states of the cryo-EM structures, was 4.21 Å (*vs* 1.75 Å for the whole remaining TMs). This confirmed the concerted movement of these two TM helices to be in line with an angular motion typical of the rocking-bundle mechanism (**Appendix Figure SI 1**;[258]).

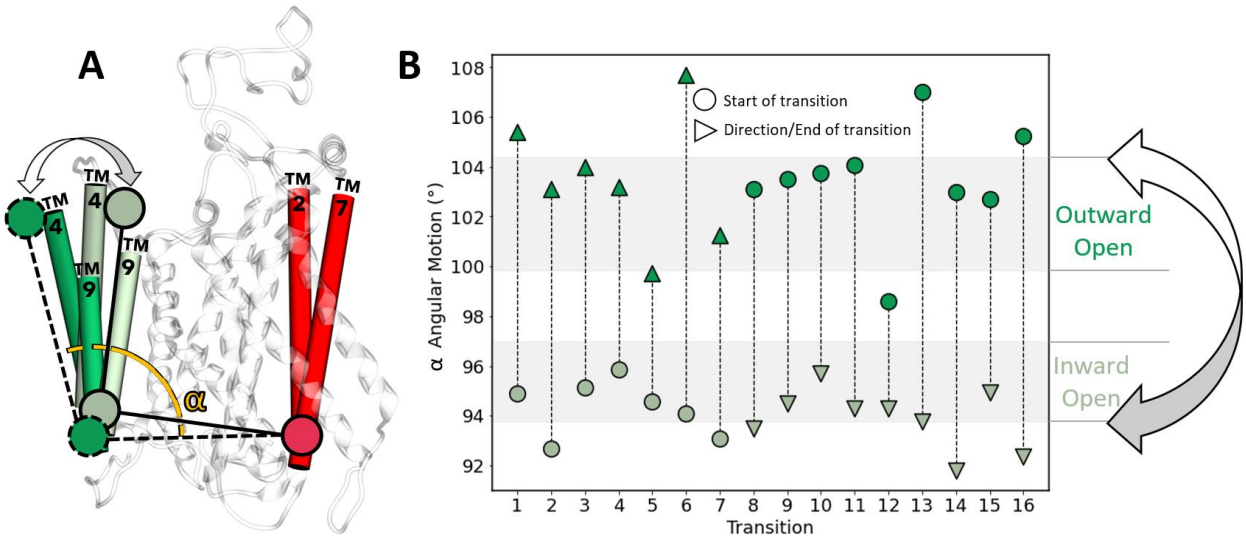

Figure 13. Rocking-bundle angular motion of specific NKCC1 TMs facilitates alternate accessibility of ion binding sites. **(A)** Schematic representation of NKCC1's angular motion, defined as the change of the angle (α) between TM 4 and TM 9 (in green) and TM 2 and TM 7 (in red), during the conformational transition between the Outward Open state (bright green) and Inward Open state (dim green), calculated from the centers of mass of the backbone atoms from the extracellular and intracellular tip of TM 4 and TM 9 and the intracellular tip of TM 2 and TM 7 (in red). **(B)** Quantification of TM 4 and TM 9 angular motion represented by the angle α through 16 conformational transitions from OPES Explore simulations. The light brown horizontal bars represent the Outward Open and Inward Open average angle α ± 1SD calculated from 1 μs of equilibrium molecular dynamics (MD). Circles represent the starting point of each transition, whereas the triangles represent the endpoint of the same transition and its direction. Circles and triangles are colored depending on the NKCC1 conformation they represent (bright green for Outward Open and dim green for Inward Open).

Interestingly, we found that TM 4 and TM 9 operate as a joint structural motif due to several hydrophobic interactions at their interface, in agreement with previous structural observations[44]. Here, we found that these hydrophobic interactions involved Ala 414, Val 417, Val 418 and Leu 421 from TM 4, while Phe 659, Leu 663 and Ile 666 from TM 9 (**Figure 14**). These interactions, statically present also in the cryo-EM structures[32,34,38,44,253], were stably maintained during our equilibrium MD simulations, in both the IO and OO states. In addition, we observed the crucial involvement of TM 10, which was key to the NKCC1's rocking bundle mechanism in our simulations. TM 10 is connected by a short loop on the extracellular side to TM 9. This connection made TM 10 susceptible to

conformational changes due to TM 4 and TM 9's angular motion, when transiting from the IO to the OO state (and *vice versa*). In our simulations, this motion modulated the solvent accessibility to the outer vestibule of NKCC1. In detail, TM 10 rested at an angle of 151.2 ± 2.9° during our equilibrium MD of the IO state, while it conserved an angle of 169.2 ± 4.0° in the OO state throughout the equilibrium MD. However, during IO → OO transitions, TM 4 and TM 9's angular motion was critical to drag the TM 10's extracellular tip outward, allowing the solvent to access the outer vestibule (**Figure 15.A**). In the OO → IO transitions, TM 10 was dynamically straightened (again, from 151.2 ± 2.9° to 169.2 ± 4.0°). This broke the interatomic contacts at the TM 10-TM 6 interface (i.e., Asn 672 with Ile 493, Pro 676 with Ala 492 and Ser 679 with Pro 496, at the TM 10 and TM 6, respectively; **Figure 16**, inset on the top right). Notably, Pro 496 and Ser 679 interacted with water molecules, thus potentially assisting the flooding of water into the NKCC1's outer vestibule. This mechanism is again in line with a rocking bundle mechanism. Also, in agreement with this evidence, during OO → IO transitions TM 4 and TM 9's angular motion pushed TM 10's extracellular tip inward, therefore disabling solvent accessibility to the outer vestibule of NKCC1. Taken together, these results show that the inward ↔ outward motion of TM 10 modulates NKCC1 solvent accessibility, as observed in all the 16 conformational transitions (**Figure 15.B**).

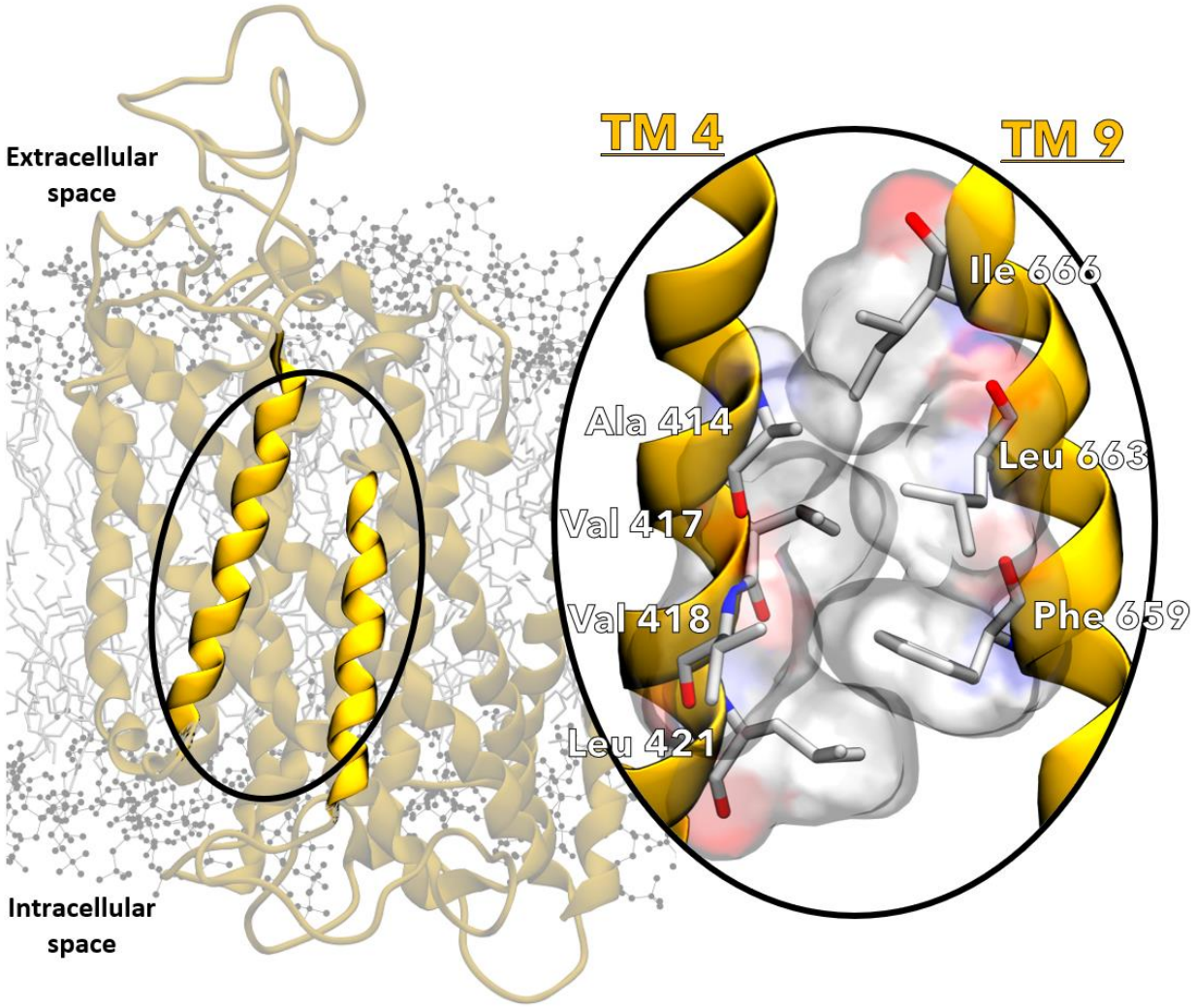

Figure 14. Stabilization of the hydrophobic interface between TM 4 and TM 9 allows for their cooperative action. Representation of human NKCC1 embedded in the cell membrane, with TM 4 and TM 9 highlighted in bright yellow. *Inset on the right*: Higher magnification of the hydrophobic interface between TM 4 and TM 9 (highlighted by the oval), which allows for their cooperative angular motion. Relevant residues are shown as sticks with their atomic surfaces pictured in red (oxygen), blue (nitrogen), grey (carbon) and white (hydrogen).

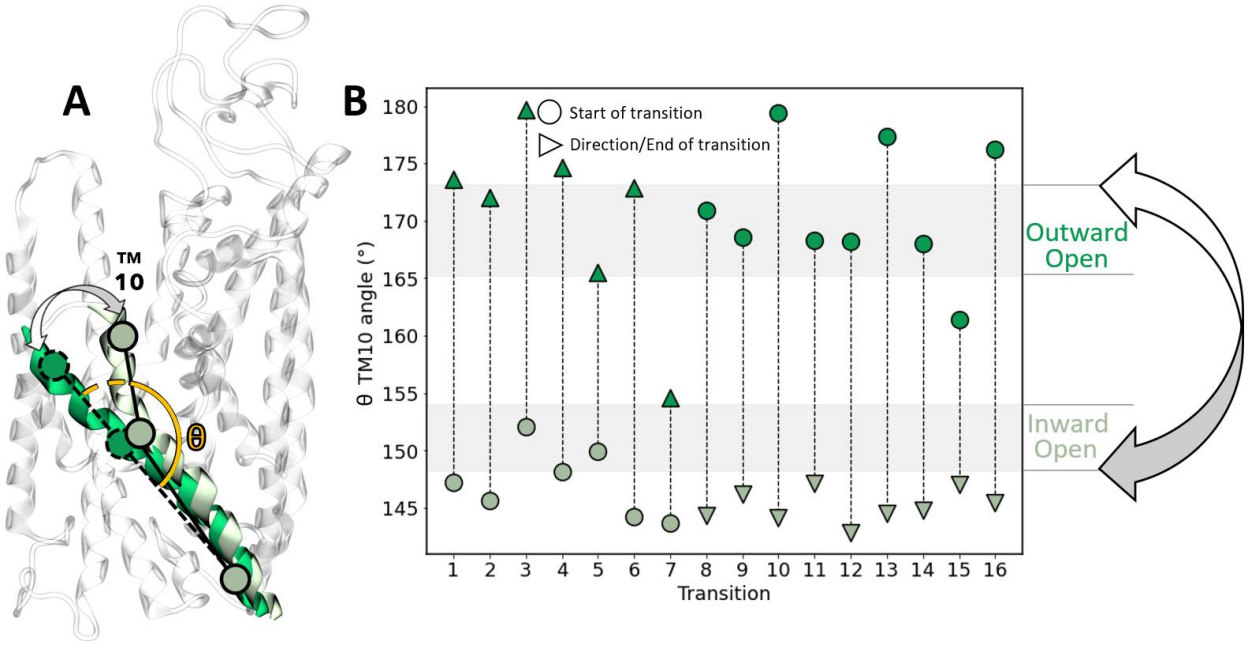

Figure 15. NKCC1 TM 10's corking motion modulates ion/water access to the outer vestibule. **(A)** Schematic representation of NKCC1 TM 10's corking motion, defined as the change of TM 10's (in green) intrahelical angle (θ), during the conformational transition between the Outward Open state (bright green) and Inward Open state (dim green), calculated from the centers of mass of the backbone atoms from TM 10' intra and extracellular tips, and the backbone atoms where TM 10 bends. **(B)** Quantification of TM 10's corking motion represented by the angle θ through 16 conformational transitions from OPES Explore simulations. The light brown horizontal bars represent the Outward Open and Inward Open average angle θ ± 1SD calculated from 1 μs of equilibrium molecular dynamics (MD). Circles represent the starting point of each transition, whereas the triangles represent the endpoint of the same transition and its direction. Circles and triangles are colored depending on the NKCC1 conformation they represent (bright green for Outward Open and dim green for Inward Open).

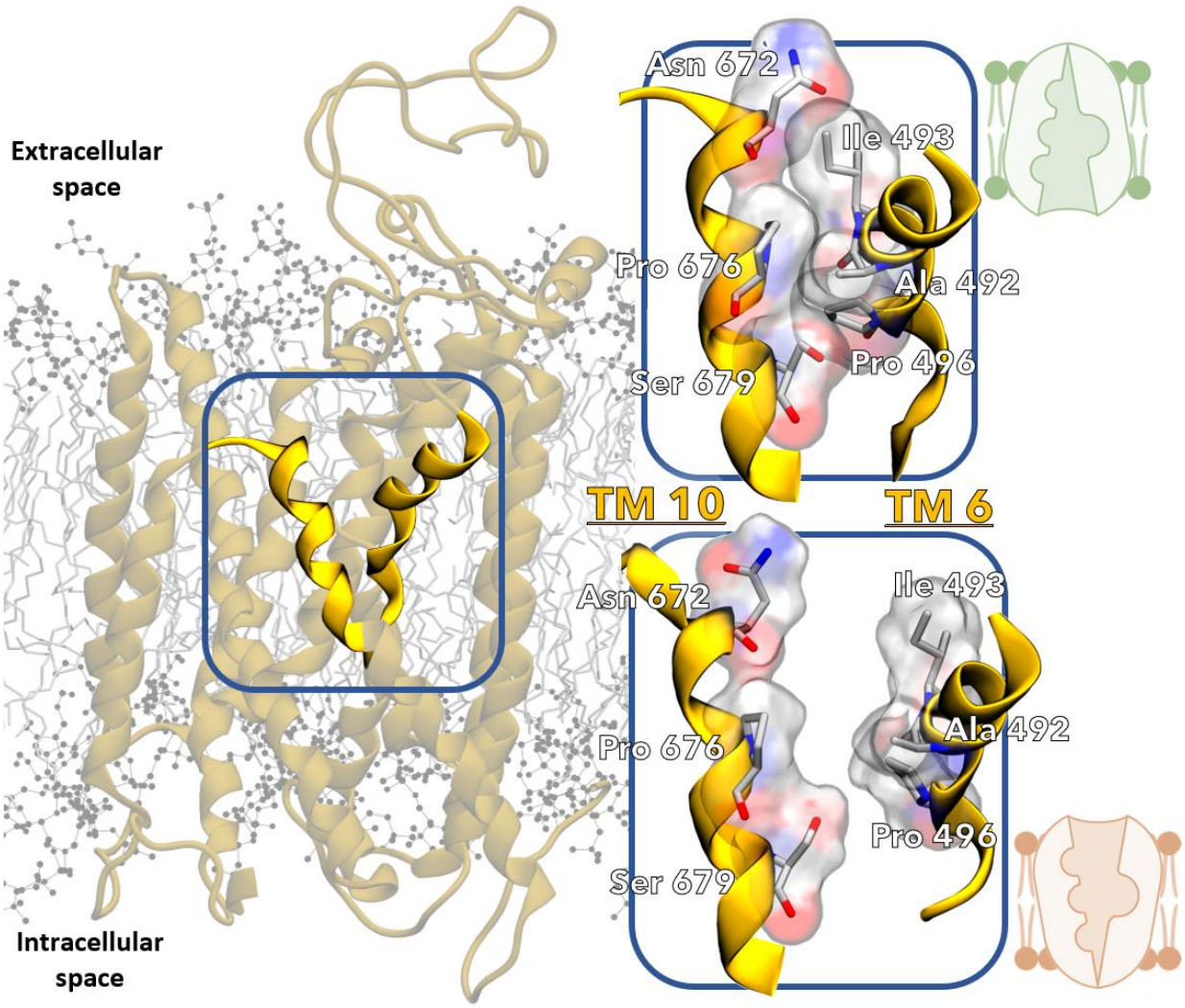

Figure 16. The interface between TM 10 and TM 6 highlights crucial interactions that determine accessibility of extracellular binding sites. Representation of human NKCC1 embedded in the cell membrane, with TM 10 and TM 6 highlighted in bright yellow. *Inset on the top right*: In the IO state, as shown by the light green schematic representation, interacting residues at the TM 10 and TM 6 interface are shown as sticks with their atomic surfaces (pictured in red – oxygen, blue – nitrogen, grey – carbon and white – hydrogen), blocking solvent access to the outer vestibule. *Inset on the bottom right*: In the OO state, as shown by the light orange schematic representation, previously interacting residues at the TM 10 and TM 6 interface are now shown to be too far apart to form bonds.

Next, we also investigated the possibility for NKCC1 to operate by the so-called 'elevator mechanism', which would be alternative to the rocking bundle one. The possibility of identifying an elevator mechanism was evaluated by measuring the vertical translation of TM 4 and TM 9 *vs* TM 2 and TM 7, which are part of the *static* domain. We found that TM 4 and TM 9 did not show any vertical translation during any of the conformational transitions, as their relative positions in the IO and OO state cryo-EM structures were not vertically translated. This is not what would be expected for an

elevator mechanism (**Appendix Figure SI 5**). Altogether, our results indicate a rocking-bundle mechanism for NKCC1 function, while excluding an elevator mechanism.

To test the functional importance of TM 10's motion and association with TM 6 as evidenced by our simulation data, we performed cell and molecular biology experiments in standard stable cell lines (HEK293 kidney cells) transfected with 4 diverse mutants (Ala490Trp, Leu664Ala, Asn665Ala and Ala668Trp) of mouse NKCC1. Specifically, the NKCC1 constructs were generated with 4 mutations on residues located at the interface between TM 10 and TM 6. These TM residues, all located at the outer vestibule (**Figure 17.A**), were selected because of their involvement in the dynamic interaction network highlighted by our MD simulations for NKCC1 conformational transitions. Next, we performed *in vitro* Cl^- influx assay[150,259,260] measurements on HEK293 cells transfected with one of the four *mouse* NKCC1 mutants, at the time.

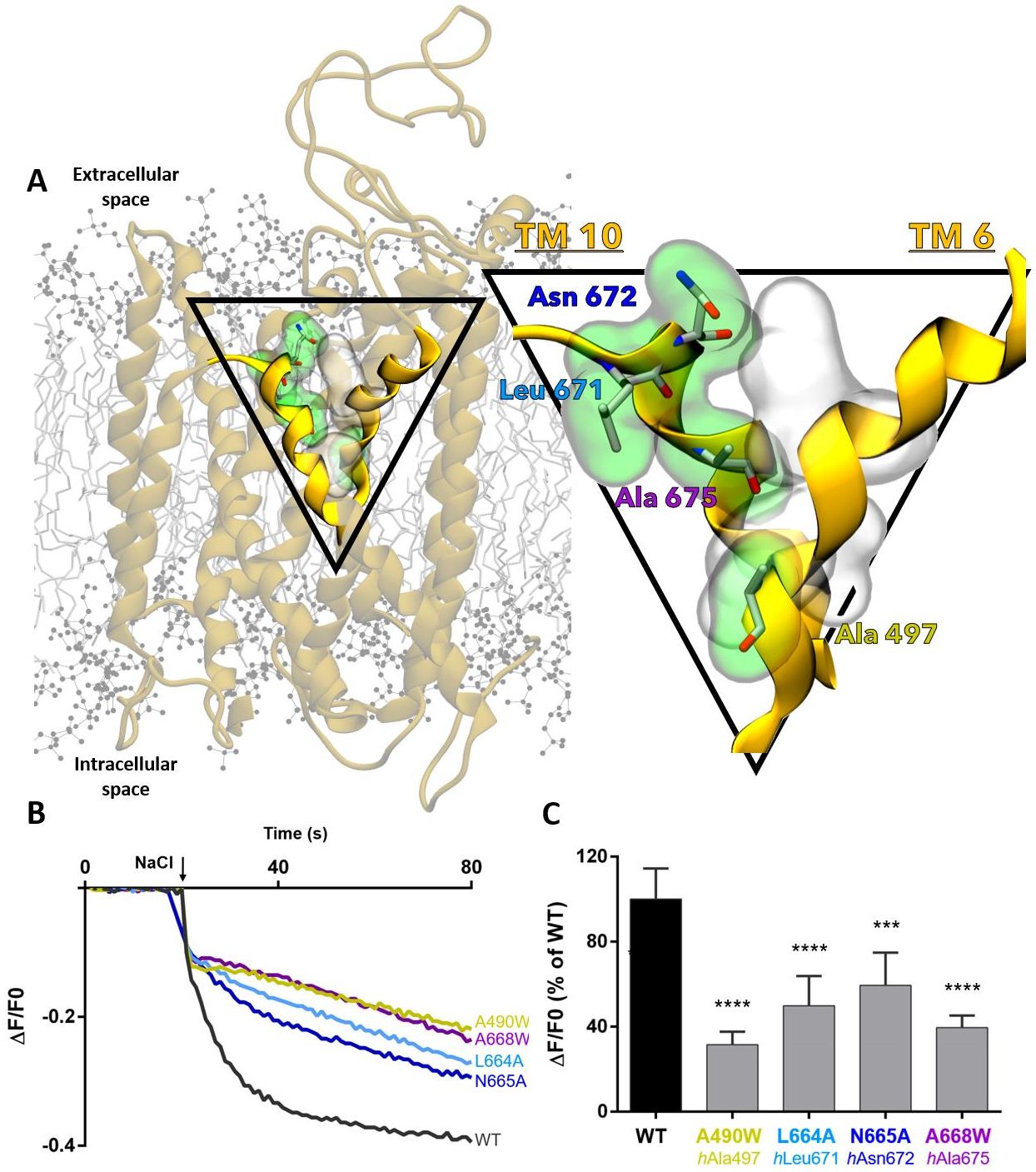

Figure 17. Mutagenesis targeting residues from TM 10 and TM 6 highlight their functional relevance. **(A)** Representation of human NKCC1 embedded in the cell membrane, with TM 10 and TM 6 highlighted in bright yellow. *Inset on the right*: The interface between TM 10 and TM 6 where homologous mutated residues are shown as sticks and are highlighted in green surface. Namely these residues are mouse A490W (human Ala 497), mouse L664A (human Leu 671), mouse N665A (human Asn 672) and mouse A668W (human Ala 675). Grey surface represents the position of residues that mainly form/break interactions throughout TM 10's corking motion. **(B)** Example traces obtained in the Cl^- influx assay on HEK293 cells transfected with the WT NKCC1 transporter or NKCC1 mutated at different residues. The arrow indicates the addition of NaCl (74 mM) to

initiate the NKCC1-mediated Cl^- influx. **(C)** Quantification of the mouse NKCC1 inhibitory activity using the Cl^- influx fluorescence assay in HEK293 cells. A fluorescence signal decrease, corresponding to a decrease in NKCC1 transporter activity, was observed for all the cells transfected with NKCC1 mutants. Data are normalized and the average of the last 10 seconds of kinetics is plotted ($\Delta F/F0$). Data are presented as a percentage of the WT. Data represent mean ± SEM from 3–4 independent experiments (Kruskal-Wallis one way ANOVA, H=216, DF=6, followed by Dunn's *post hoc* test on multiple comparisons, *** P = 0.0002, **** P < 0.0001).

In our *in vitro* cellular assay, all mutations lead to a decrease in ion transport function, when compared to the wild-type (WT) *mouse* NKCC1 (**Figure 17.C**). In detail, the selected mutations were Ala490Trp (equivalent to *human* NKCC1 Ala497Trp at TM 6, alignment shown in **Appendix Figure SI 9**). This mutation introduces a bulky side chain that disrupts the formation of the Ser 679 – Pro 496 interaction at the TM 6 – TM 10 interface at the outer vestibule. Ala490Trp mutation led to reduced transport by a factor of 1.7 when compared to the WT NKCC1. We infer that by affecting TM 10's motion, the NKCC1's IO state is destabilized, therefore disrupting ion transport. Additionally, the mutations Leu664Ala, Asn665Ala and Ala668Trp (equivalent to *human* Leu671Ala, Asn672Ala and Ala675Trp, see **Appendix Figure SI 9** - all residues located in the extracellular tip of TM 10) also led to a reduction in ion transport by a factor of 1.4, 1.3, and 1.6, respectively, when compared to the wildtype NKCC1 (**Figure 17.C**). In this context, the Leu664Ala and Asn665Ala mutations on TM 10 remove the side chain that interacts with the Asn672 and Ile493 residues on TM 10 and TM 6, respectively. The mutation Ala675Trp introduces a bulky sidechain that disrupts the formation of the Pro 676 – Ala 492 interaction, weakening the TM 10 mobility (**Figure 17.A**).

Overall, our simulations and mutagenesis data support a rocking-bundle mechanism for NKCC1 conformational transitions, which critically relies on the TM 4 and TM 9's angular motion and dynamic contacts of residues at the TM 6 – TM 10 interface, with TM 10 that seems to also modulate the access of the solvent to the outer vestibule.

4.3.2. Free Energy simulations characterize the previously elusive NKCC1's occluded state

Then, we analyzed the free energy surface (FES) for IO ↔ OO conformational transitions of NKCC1 as revealed by the OPES Explore algorithm and collective variable (CVs) used to enhance the sampling of the complex dynamical transitions between open conformations of the inner and outer vestibules of the transporter (*see paragraph above and methods section*). Our simulations revealed four distinct free energy minima that correspond to conformational states of NKCC1. Notably, the IO state is located in the deepest minimum. We found that the IO state basin was centered on a value of -1.6 in the CV

dimension (**Figure 18** and **Appendix Figure SI 6**). Further equilibrium MD starting from snapshots extracted from this basin showed a stable IO model (**Appendix Figure SI 7.A**). On the other hand, the OO state was distributed into a shallow area located at ~2.6 in the CV dimension of the FES. However, we found this area to cover different hydration states of the transporter (OO^w and OO^d in **Figure 18**). That is, both OO^w and OO^d are stable OO state conformations that differ in the extent of their water hydration (**Appendix Figure SI 7.B**). Indeed, the outer vestibule in the OO^d minimum has a coordination number of waters of ~10.5, while the outer vestibule in OO^w showed a coordination number of ~20.5.

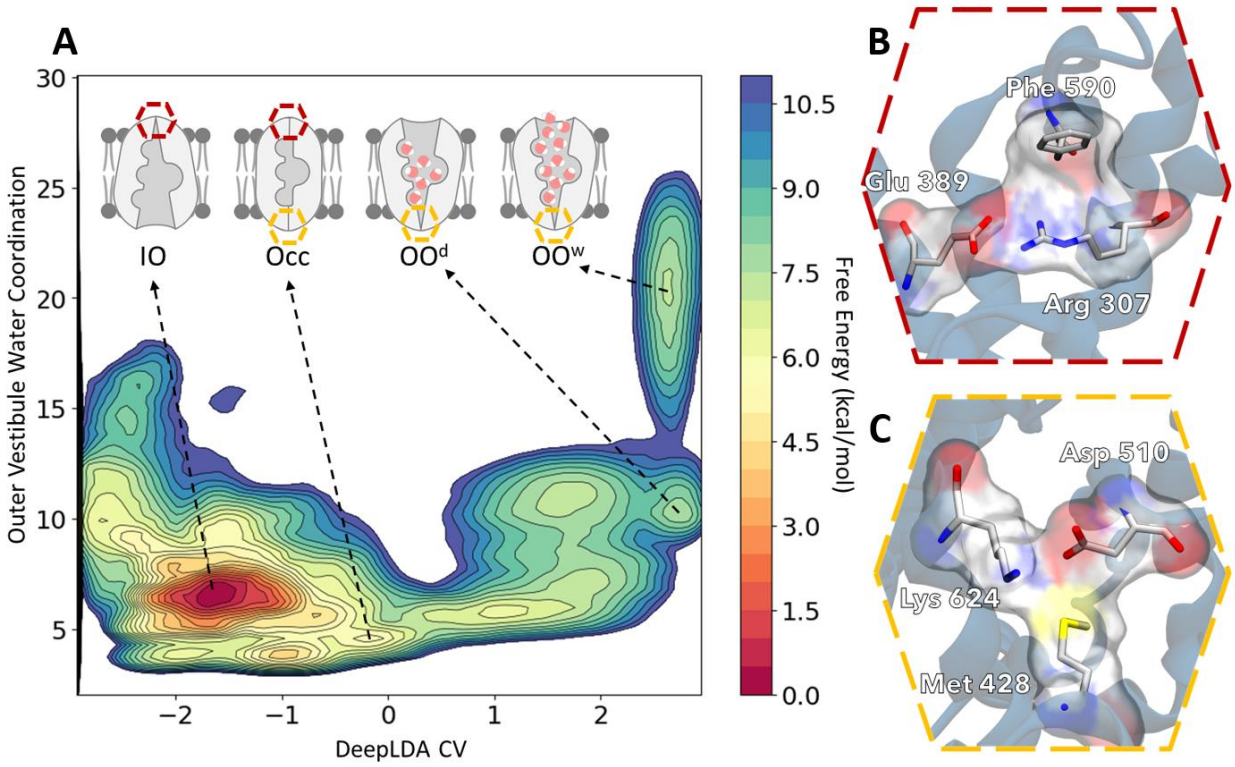

Figure 18. Free Energy Surface identifies relevant NKCC1 conformations for the Inward Open ↔ Outward Open transition. **(A)** Representation of the Free Energy Surface of the conformational transition between *human* NKCC1 IO and OO states computed by OPES Explore over the DeepLDA collective variable and the outer vestibule water coordination collective variable. Energetical basins are highlighted with a schematic representation of the conformation they identify. These are, namely: the IO state, the occluded state (labeled Occ), the OO^d state (outward open "dry" – lower outer vestibule hydration) and OO^w (outward open "wet" – higher outer vestibule hydration. **(B)** Higher magnification of the hexagon in A representing the main gating interactions that occlude the outer vestibule and block solvent access to the ionic binding sites. Relevant residues are shown as sticks with their atomic surfaces pictured in red (oxygen), blue (nitrogen), grey (carbon) and white (hydrogen). **(C)** Higher magnification of the hexagon in A representing of the main gating interactions that occlude the inner vestibule and block solvent access to the ionic binding sites. Relevant

residues are shown as sticks with their atomic surfaces pictured in red (oxygen), blue (nitrogen), yellow (sulfur), grey (carbon) and white (hydrogen).

Importantly, our exploration of the FES also captured NKCC1 in its occluded state (Occ, **Figure 18.A**). Notably, such NKCC1 occluded state had been only hypothesized to exist[261], as it has never been structurally determined, likely due to its transitory nature. This state was located at ~0 in the CV space, with an outer vestibule hydration coordination number of 4.8. Notably, such an occluded state emerged naturally from our deep learning-guided enhanced sampling simulations trained solely on the IO and OO state conformations.

In our simulations, the occluded state depicts NKCC1 with its ion binding sites inaccessible to the solvent, from either side of the membrane (Occ in **Figure 18.A**), and it is characterized by having both outer and inner vestibules occluded. The outer vestibule has in place an extensive intermolecular interaction hub. This was built up by Arg307, which formed a salt-bridge with Glu 389, and cation-π interactions with Phe 590 (**Figure 18.B**). Additionally, the interactions between Asn 672-Ile 493, Pro 676-Ala 492 and Ser 679-Pro 496 were fully formed in the NKCC1 occluded state, thus occluding access of the extracellular solvent to the outer vestibule. On the other side, the inner vestibule was occluded to the intracellular solvent due to several other interactions among residues. Those interactions were mostly conserved also in the OO state of the cryo-EM structure[44]. Primarily, these interface residues interactions are formed after the shifting of Met 428 and the consequent occlusion by the intracellular loop 1. Interestingly, the salt-bridge between Asp 510 and Lys 624, formed in the OO state where it occludes the inner vestibule (**Figure 18.C**), is not formed in the occluded state. Notably, the occluded state was maintained for over 100 ns in our equilibrium MD simulations, which started from configurations of the Occ basin visited during the enhanced sampling trajectories (**Appendix Figure SI 7.C**), with an RMSD of 1.00 ± 0.11 Å. In these simulations, all ion binding sites remained inaccessible to the solvent from either side of the membrane, as shown in the occluded basin pore profile in **Figure 19.B**. Notably, this differs greatly from the IO and OO state equilibrium MD pore profiles (**Figure 19.A** and **19.C**, respectively), confirming that such transitory state is structurally distinct from the IO and OO states. Ultimately, the occluded state is therefore the only transitory conformation that ensures solvent inaccessibility to the ion binding sites from both the intra and extracellular vestibules.

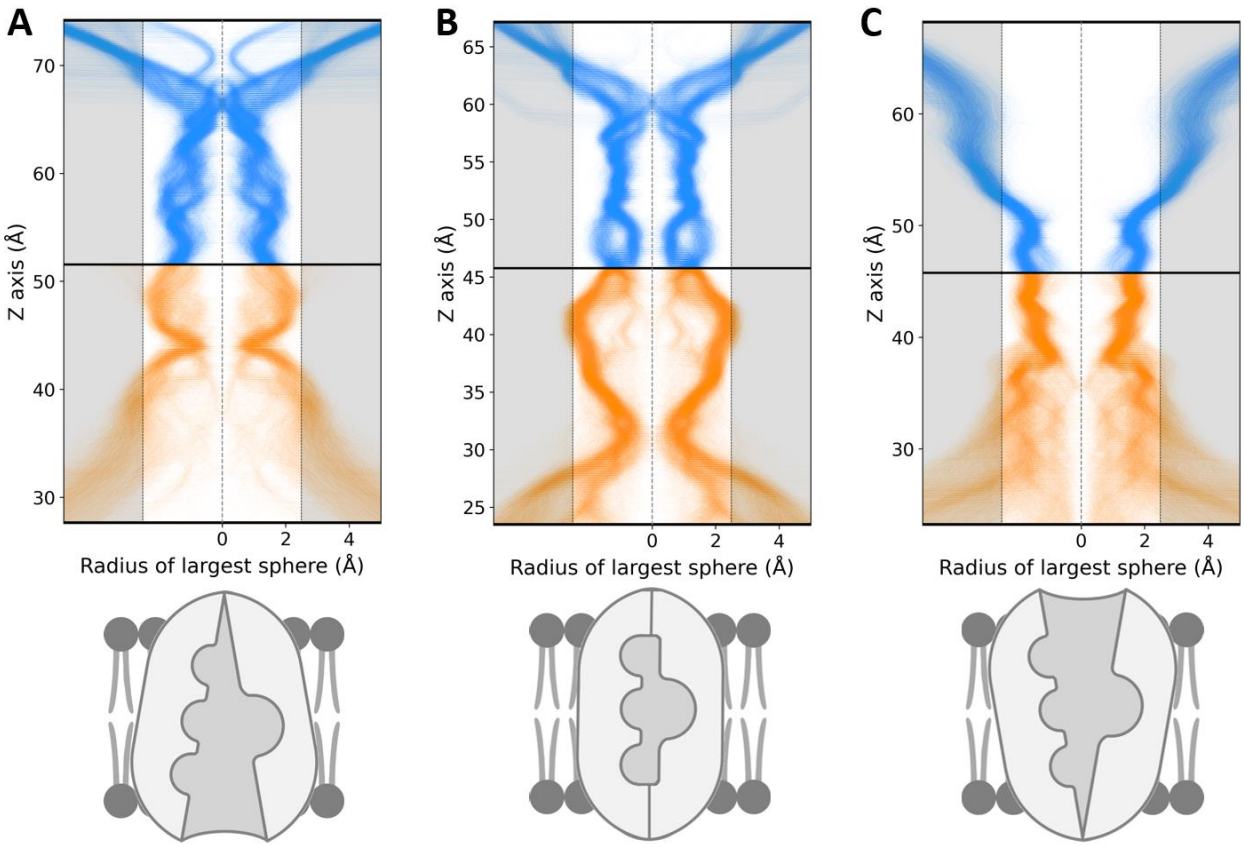

Figure 19. Pore profile confirms distinct binding-site accessibility of NKCC1 states along the Inward Open ↔ Outward Open transition. **(A-C)** Pore profile of the IO state **(A)**, the occluded state **(B)**, and OO state **(C)**, schematically represented at the bottom. These profiles were obtained by calculating the radius of the largest sphere along the Z-axis of the ion translocation cavity, and then plotting the pore profile of several snapshots from their corresponding equilibrium MD simulations, computed by the software HOLE. Pore profiles were mirrored around radius 0 for visual clarity. The blue lines represent the outer vestibule, and the orange lines represent the inner vestibule of NKCC1.

In our FES (**Figure 18.A**), the IO state transited to the occluded state with a barrier of ~5.5 kcal/mol. From this transitory occluded state, there is another barrier of ~5.5 kcal/mol to reach the OO^{w} state. Interestingly, the reverse transition appears less energetically costly, as the OO^{w} state transited to the occluded state with a barrier of ~3.5 kcal/mol, then followed by a ~0.5 kcal/mol barrier to reach the IO state. Therefore, the IO state was ~7 kcal/mol more stable compared to the OO^{w} state. Taken together, our simulations depict IO ↔ OO transitions passing though the occluded state, further corroborating the rocking-bundle mechanism for NKCC1 function.

Then, we determined the free energy associated with ion binding to the NKCC1 OO state. According to previously published kinetic data[21], ions bind to NKCC1 from the extracellular side of the membrane in the order Na^+, Cl^-, K^+, Cl^-. We first simulated Na^+ binding to an unloaded OO state

NKCC1 structure (**Appendix Figure SI 12.A**), and found a $\Delta G_{bind} \approx$ -7.5 kcal/mol, with a binding barrier of $\Delta G^{\ddagger}_{TS-unbound} \approx$ 5.0 kcal/mol and an unbinding barrier of $\Delta G^{\ddagger}_{TS-bound} \approx$ 12.5 kcal/mol. We then evaluated binding of the first Cl^- ion to a Na^+-bound OO state NKCC1 structure (**Appendix Figure SI 12.B**), which presented a $\Delta G_{bind} \approx$ 1.0 kcal/mol, with a binding barrier of $\Delta G^{\ddagger}_{TS-unbound} \approx$ 4.0 kcal/mol and an unbinding barrier of $\Delta G^{\ddagger}_{TS-bound} \approx$ 3.0 kcal/mol. Next, we evaluated K^+ binding to a Cl^--Na^+-bound OO state NKCC1 structure (**Appendix Figure SI 12.C**), and we obtained a $\Delta G_{bind} \approx$ 1.0 kcal/mol, with a binding barrier of $\Delta G^{\ddagger}_{TS-unbound} \approx$ 4.5 kcal/mol and an unbinding barrier of $\Delta G^{\ddagger}_{TS-bound} \approx$ 3.5 kcal/mol. After these ion binding simulations, we ran additional ~100 ns of equilibrium MD of each system and observed that all these partially/fully loaded states were stable, i.e., all ions remained stably coordinated to their binding site throughout the simulations time. Interestingly, within the first 5 ns of the K^+-Cl^--Na^+-bound OO NKCC1 state, we observed the spontaneous binding of the second Cl^- ion to its binding site, leading to the fully loaded OO state of NKCC1, which was stably maintained for over 1 μs.

We analyzed the ion binding sites and ion coordination to inspect possible effects of the conformational transition OO → IO to those ion binding sites. First, we observed that ion loading does not affect the overall secondary structure of NKCC1 (RMSD between loaded and unloaded states: IO = 1.71 Å, occluded = 1.97 Å, OO = 1.63 Å) and that the fully loaded occluded → IO state conformational transition is characterized by the same angular motion of TM 4 and TM 9 (**Appendix Figure SI 11**). Also, we noticed that all ions remained bound to their respective site throughout the conformational transition OO → Occluded → IO, although minor changes were detected. In detail, the Na^+ binding site is composed by residues: Leu 297, Trp 300, Ala 610, Ser 613, Ser 614. Na^+ maintains its interactions with most of its coordination sphere in the fully loaded OO, occluded and IO states (**Appendix Figure SI 13.A**). The only state-dependent modification are the interactions between Na^+ and Ala 610, which change during the conformational transition. This distance started at an average length of 2.7 ± 0.7 Å in the OO state (i.e., tightly bound), and increased in both occluded and IO states to respectively 4.4 ± 0.5 Å and 4.6 ± 0.4 Å (i.e., loosely bound). The interactions of the first Cl^- to its binding site (closest to the intracellular side), are with residues: Gly 500, Ile 501, Leu 502, Tyr 686. These remained unchanged between the fully loaded OO, occluded and IO states (**Appendix Figure SI 13.B**). Most of K^+ interactions with its binding site, which is composed by residues: Asn 298, Ile 299, Tyr 383, Pro 496, Thr 499, are stably maintained through NKCC1's conformational transition (**Appendix Figure SI 13.C**). The exceptions are the interaction between

the bound K^+ and residue Asn 298, which changes during the conformational transition. This K^+ is initially tightly bound in the OO state (average distance to Asn 298 = 2.9 ± 0.3 Å) to become loosely bound in the Occ and IO states (average distance to Asn 298 = 4.1 ± 0.8 Å and 4.4 ± 0.7 Å, respectively). The interaction with Thr 499 also changes during the conformational transition, although this occurs at a different stage of the process. In both OO and Occ states, K^+ remains tightly bound (average distance to Thr 499 = 2.7 ± 0.2 Å and 2.8 ± 0.2 Å, respectively) but becomes loosely bound in the IO state (average distance to Thr 499 = 4.3 ± 1.6 Å). On the other hand, the second Cl^- has a distinctive binding mode to its binding site (closest to the extracellular side), which is composed by residues: Val 302 and Met 303. In the OO state, it can be found loosely bound to both Val 302 and Met 303 (average distance to each residue being 4.5 ± 1.7 Å and 5.2 ± 1.8 Å, respectively). Whereas it is tightly bound in the occluded (average distance to each residue being 2.4 ± 0.2 Å and 2.6 ± 0.2 Å, respectively) and IO state (average distance to each residue being 2.5 ± 0.3 Å and 2.7 ± 0.3 Å, respectively). These results further support that this second Cl^- has the propensity of spontaneously binding to the OO state.

4.3.3. NKCC1 permeability allows water transportation

To better understand the capabilities to transport water of NKCC1, we modeled two new additional conformational states. These were IO and OO, which we loaded with two Cl^-, a Na^+ and a K^+ ions in their respective binding sites. These two fully loaded models allowed us to evaluate water permeability and water transport in NKCC1 in the presence of ions (as opposed to the previous models that were studied in the absence of ions). Notably, we observed an average of 13 water molecules trapped in the ion binding cavity through 100 ns of equilibrium MD simulations of the occluded state without ions bound. This value would then represent an estimation of the maximum amount of water molecules transported per alternating access cycle. Interestingly, our simulations also showed that NKCC1 adopts water permeable states in the OO state (**Figure 20.A**), preferentially when unloaded (38.2% of the trajectory, **Figure 20.B**), while it does so only to a minor extent in the OO state with 4 ions bound (1.1%, **Figure 20.C**). Finally, NKCC1 is not permeable at all in the loaded and unloaded IO and Occluded states.

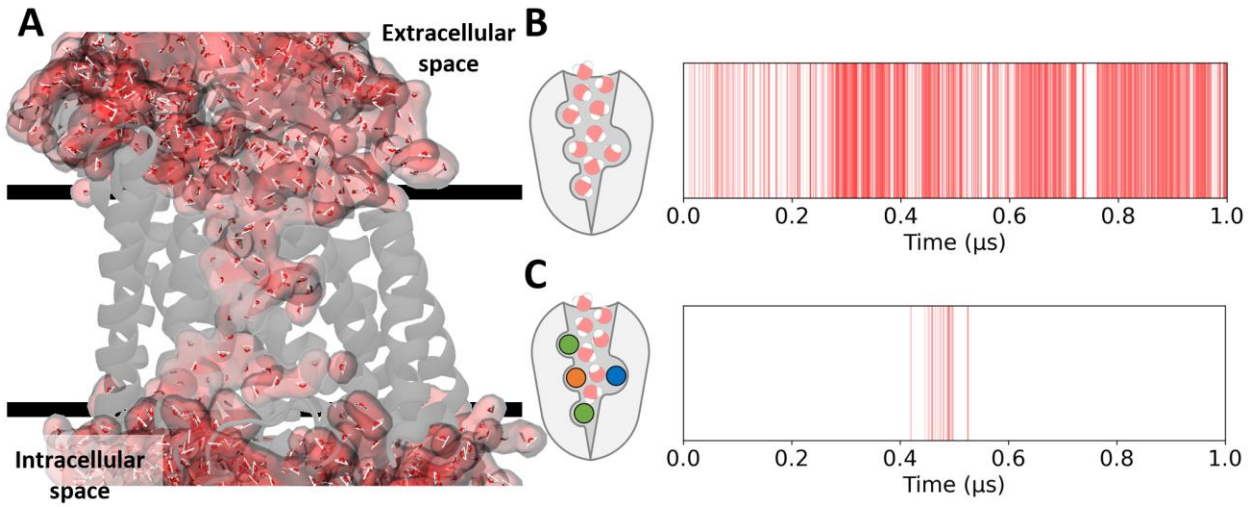

Figure 20. NKCC1's outward open conformations are permeable to water. **(A)** Representation of NKCC1 (grey cartoon) embedded in the membrane (black horizontal bars) in a water-permeable state. Water molecules are shown as red and white lines with a red atomic surface representation. A chain of water molecules whose oxygen atoms are within 4.0 Å of each other connecting the extracellular and intracellular solvent is present. **(B, C)** Schematic representation of both states that present permeability to water (outward-open without ions bound, **B**, or fully loaded, **C**), and their respective plot, which tracks the appearance of permeable states during each state's equilibrium MD simulation. Vertical red bars represent snapshots from the respective simulation where a chain of water molecules whose oxygen atoms are within 4.0 Å of each other connecting the extracellular and intracellular solvent through NKCC1 is observed.

Water-permeable states of NKCC1 have an average lifetime of 0.5 ± 0.5 ns, with a median of 0.2 ns and a maximum lifetime of 5.0 ns in the unloaded OO conformation. On the other hand, water permeable states in the OO fully loaded state have an average lifetime of 0.3 ± 0.2 ns, with a median of 0.2 ns and a maximum lifetime of 1.0 ns. This finding is in line with our mechanistic insights provided by the enhanced sampling simulations, which showed that in the IO states, TM 10 modulates the hydration of the outer vestibule. Ultimately, when NKCC1 adopts a permeable state, water molecules may diffuse across the membrane. During the 1 μs-long MD simulations of the OO state, we tracked 517 complete water molecule efflux events and 497 influx events (**Figure 21**). It is to be noted that these were pure diffusion events, as our MD simulations did not include any concentration gradient across the membrane. With this premise, we estimated the average water diffusion rate as 1.8 ± 2.5 ns and 2.0 ± 4.2 ns, in the outward and inward direction, respectively.

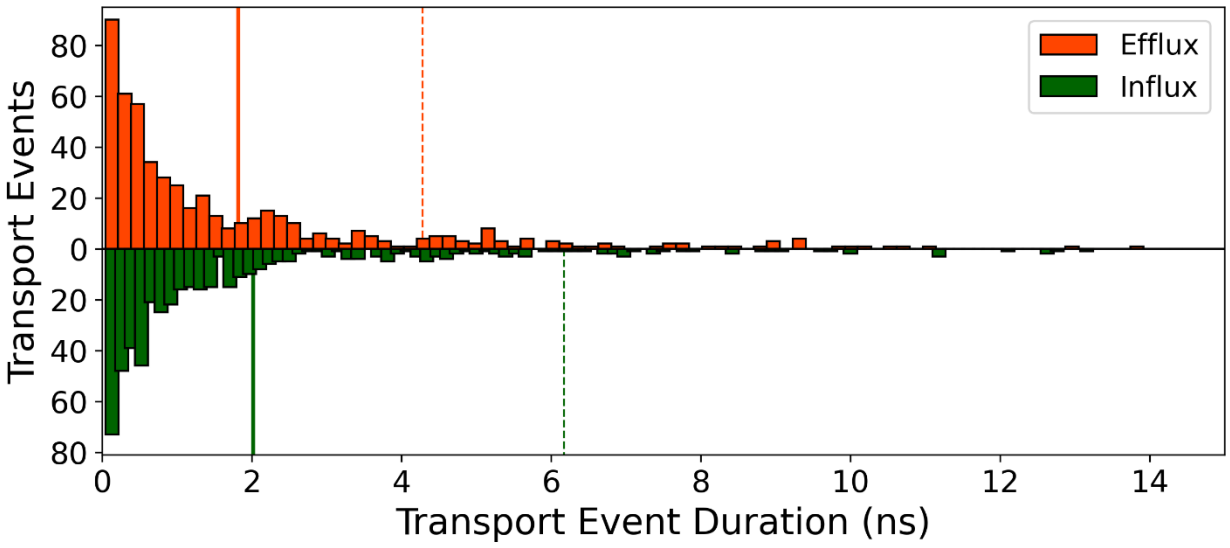

Figure 21. NKCC1 passively transports water. Histogram of all transport events detected in the state equilibrium MD simulation of NKCC1 outward open conformation with no ions bound, organized by the length of each transport event. Bars show the frequency of efflux/influx (orange/green) events per transport event duration. Vertical continuous lines show the mean, and discontinuous lines show the standard deviation (efflux, orange; influx, green). Some longer transport events were excluded from the histogram for clarity.

4.4. Discussion

The cation chloride cotransporter (CCC) NKCC1 plays a crucial role in cellular osmolarity by regulating ionic balance and water flux[262] , and it is currently targeted to treat a variety of related imbalance diseases, e.g. brain disorders including neurodevelopmental, neurodegenerative, neurological, disorders and hydrocephalus, as well as cancer[6,155,250–252]. Motivated by the recent structural data on NKCC1 in different conformations – inward open (IO) and outward open (OO) states – we built and simulated atomistic models of human NKCC1, where the transporter is embedded in the membrane. We used these models to run multiple μs-long MD equilibrium and enhanced sampling simulations of those key IO and OO states and capture the exact protein dynamics for IO ↔ OO transitions.

Notably, our investigation led to a grand total of 16 conformational transitions observed using the OPES algorithm for enhanced sampling simulations[216]. These simulations revealed a rocking-bundle mechanism for conformational transitions for the unloaded NKCC1 protein. Specifically, such a rocking-bundle mechanism shows alternate access to the NKCC1 ion binding sites through two concerted motions. First, helices TM 4 and TM 9, associated to each other by hydrophobic interactions, go through an angular motion of ~14° between the IO and OO state. This is then coupled by the motion of TM 10, linked by a short extracellular loop to TM 9. The latter alternatively affects the bending or straightening of TM 10, thus blocking/allowing solvent access to the ion binding sites from the extracellular side. Such motions were consistently observed in all our IO ↔ OO state transitions. We also observed these motions in our fully loaded NKCC1 model, suggesting that NKCC1 undergoes the rocking-bundle mechanism with and without ions bound. Remarkably, NKCC1's TM 4, TM 9 and TM 10 behavior is conserved in the LeuT-fold sodium-benzylhydantoin transporter Mhp1 from *Mycobacterium liquefaciens*[24], where the same TM helices may therefore carry out an analogous role for function.

Importantly, from our enhanced sampling simulations, we also identified the so-called 'occluded state' for NKCC1, where the ion binding sites are inaccessible from both sides of the transporter (i.e., both the inner and outer vestibules are closed). Notably, the occluded state was only hypothesized to exist based on previous structural studies[261], although it has never been experimentally observed in any of the CCCs. On the other hand, in our simulations, we like to emphasize that the deep learning-guided sampling of NKCC1 conformations detected such occluded state without any previous knowledge of

its existence. In other words, this previously uncharacterized occluded conformational state was not used to generate our dataset and identify proper collective variables (CVs) for deep-learning enhanced sampling simulations, which therefore have unexpectedly revealed such a minimum on the FES, with no external solicitation. In addition, the OO state shows two distinct conformations, distributed into a shallow area located at ~2.6 in the FES. These conformations (OO^w and OO^d in **Figure 18**) show a difference in the extent of their water hydration (**Appendix Figure SI 7.B**) at the vestibules, due to the modulatory motion of TM 10. Interestingly, the hydration level of the outer vestibule in the OO state was significantly affected by the Arg 307-Glu 389 salt bridge (**Appendix Figure SI 8**). It is also worth noting that the drug bumetanide is bound to the outer vestibule in all the available cryo-EM structures of NKCC1 in the OO state[44,253]. Ligand binding at the outer vestibule hampers the formation of the Arg 307-Glu 389 salt bridge, which is therefore proven to be crucial for the rocking bundle mechanism in NKCC1.

Overall, the IO state is found to be the lowest energy basin of the FES. From the IO state, the transporter transits to the OO state, passing through the occluded state. Our semiquantitative estimation of the energetic cost for the IO → OO transition is ~10.5 kcal/mol, whereas the estimated cost for the OO → IO transition is ~3.5 kcal/mol. Interestingly, these energetic estimates would also explain why all the so-far resolved NKCC1 apo structures have been captured in the lowest free energy IO state minimum.

Another interesting observation is related to the possibility of NKCC1 to transport water molecules. Here, we have observed and quantified the ability of water to passively permeate through NKCC1. Using additional simulations with four ions bound to the IO and OO states, we could compare the presence of water molecules in different models and observe that NKCC1 indeed adopts water permeable states exclusively in the unloaded OO state (38.2% of the trajectory, **Figure 20.B**). We found that NKCC1's water permeable states have an average lifetime of 0.5 ± 0.5 ns, with water molecules that can diffuse across the membrane. In our MD simulations of the OO state, we tracked 517 complete efflux events and 497 influx events (**Figure 21**), which occur through diffusion, as our MD simulations does not imply concentration gradient across the membrane. With this premise, we estimated the average water diffusion rate, which is 1.8 ± 2.5 ns and 2.0 ± 4.2 ns, in the outward and inward direction, respectively. Water transport may also take place via the alternating access cycle. During the simulation of the occluded state without bound ions, we observed about 13 water molecules trapped in the ion binding region. The latter can be therefore considered an estimation of

the maximum amount of water molecules transported per alternating access cycle. Interestingly, these semiquantitative observation enrich the current experimental evidence for water transport by NKCC1[263,264] and its functional implications in the context of cerebrospinal fluid accumulation recently demonstrated[42,265]. Indeed, water may cross the membrane *via* the formation of permeable states, as has been reported for a wide range of transporters; including Na^+/glucose transporter (SGLT), glutamate transporter (Glt_{ph}), glycerol-3-phosphate transporter (GlpT), sodium-benzylhydantoin transporter (Mhp1), and the maltose transporter[266], and more recently also shown for the sodium/proton antiporter PaNhaP[267].

One more mechanistic feature from our simulations is the inter-helical interface intrinsically associated to NKCC1's transport capabilities. This interface is formed by the extracellular tip of helices TM 10 and TM 6. In particular, the interatomic contacts at the TM 10-TM 6 interface are maintained in the IO state (**Figure 16**), allowing sealing the outer vestibule in the IO state. This interaction will then be broken to transit to the OO state, aided by the specific rocking-bundle mechanism and the associated helices motions (TM 4 and TM 9, **Figure 13**). To prove the relevance of such a critical protein interface, we also mutated a few residues located in it. From *mouse* NKCC1, we inserted the following mutations: Ala490Trp in TM 6, and Leu664Ala, Asn665Ala and Ala668Trp in TM 10 (equivalent to *human* NKCC1 Ala497Trp, Leu671Ala, Asn672Ala and Ala675Trp, respectively). All these mutations led to a significant reduction in ion transport (**Figure 17**). This is also in line with previous cross-linking experiments, which highlighted significant movement of TM 10 during NKCC1 ion transport[268]. This further validates the key modulatory motions reported here for TM 10. Notably, TM 4's functional importance is supported by mutational data showing that the Arg410Gln mutation – located at the extracellular extreme of TM 4 – leads to a loss of function[77]. Our computational evidence is therefore well supported by our and literature's mutagenesis data.

Additionally, we have characterized the energy profile of ion binding to the OO state of NKCC1. Crucially, we found that the Na^+ dissociation energy in the OO state is 12.5 kcal/mol, whilst its dissociation energy in the IO state has been previously reported to be 6.9 ± 0.8 kcal/mol[269]. We note that the free energy calculations for ion release that pertain the IO state[269] were performed via well-tempered metadynamics, whilst ours pertain the OO state for ion binding and unbinding using OPES Explore simulations. While qualitative, however, these results hint to a higher binding affinity of Na^+ to the OO state than to the IO state. Notably, this is congruent with NKCC1's use of Na^+ electrochemical gradient to import Cl^- and its overall functional cycle – where ions bind to the OO

state from the extracellular side of the membrane and are then released from the IO state into the intracellular side of the membrane.

Extension of our mechanistic implications to Na^+-dependent CCCs: Intriguingly, the results on the functional relevance of TM 4 and TM 9, along with TM 6 and TM 10, motivated our analysis of additional mutations of CCCs in this region, often linked to the insurgence of pathologies[41]. In doing so, we found a total of 38 mutations (including the new 4 mutations reported here), which are all located on the functionally relevant helices identified in our work, namely TM 4, TM 6, TM 9 and TM 10, highlighted in red in **Appendix Figure SI 9**. These four TM helices present an extremely high level of conservation (considering either identity and similarity) in Na^+-dependent CCCs – between 80% and 100% when compared to *human* NKCC1, as shown in **Appendix Figure SI 9**. On the other hand, these functionally relevant TM helices present a much lower degree of conservation in Na^+-independent CCCs, with values ranging from 40% to 73% when compared to *human* NKCC1. Therefore, the rocking-bundle mechanism seems to operate only to Na^+-dependent CCCs, to which NKCC1 belongs. Na^+-independent CCCs (KCCs) may operate through a different alternate access mechanism, where transitions seem driven by different TM helices, like TM 3 and TM 8 in the *human* KCC1[35]. In particular, we could only find 3 mutations in our region of interest in Na^+-independent CCCs that lead to transporter dysfunction, and all these are in TM 6. However, these three mutations are reported to have functional effects that seem unrelated to the rocking-bundle alternating access mechanism. Specifically, the *human* KCC2's Leu426Pro mutation leads to complete loss of protein function, with reduced expression and glycosylation[102]. The *human* KCC2's Met438Val mutation alters the Cl2 binding site (referenced on the cited article as Met415Val because mutated in KCC2b) and therefore leads to impaired Cl^- extrusion[102]. Finally, the Phe493CysfsX48 mutation in *human* KCC3 is associated to a frameshift mutation, which generally carries serious pathogenic consequences, like in this case with agenesis of the corpus callosum[116].

In summary, our computational simulations and free energy calculations, coupled to mutagenesis experiments, show that NKCC1 operates through the rocking-bundle mechanism, transiting from the unloaded inward open (IO) to the outward open (OO) states, and *vice versa*. We also found that the OO states are permeable to water, which can freely go through NKCC1 across the membrane. Importantly, we found that most functionally relevant TM helices involved in such a mechanism are highly conserved in Na^+-dependent CCCs. This overall evidence and critical mechanistic implications could open to new strategies for NKCC1 function modulation and novel modes of drug action.

4.5. Methods

4.5.1. Equilibrium MD

The IO state model was constructed based on the cryo-EM structure of apo *human* NKCC1[34], using the transmembrane domain of one monomer (comprising residues 288 to 753). The OO state model was built from the last snapshot from previous simulations[44], from which we removed bumetanide and bound ions and allowed water to flood the space previously occupied by the removed elements. For both states, NKCC1 monomer was embedded in a POPC bilayer. PropKa 3.0[239] was used to determine the ionization state of titratable residues, assuming pH 7. The simulation box included NKCC1 accompanied by 221/308 POPC molecules, 59/63 Cl^-, 29/31 Na^+ and 31/33 K^+ ions (in the bulk solution, corresponding to ~150 mM concentration) and ~19300/22000 water molecules. In total, ~95000/114000 atoms and a simulation cell of 87 Å × 96 Å × 110 Å and 100 Å × 115 Å × 97 Å dimensions, for the IO and OO state respectively. Initial configurations of each model were assembled using Packmol-Memgen[240], part of the AmberTools software package.

Equilibrium MD simulations were performed using the GPU version of the PMEMD code[241] of the AMBER package[242]. The protein was modeled using the ff14SB force field[243], Lipid17 for the POPC bilayer[244], TIP3P for water[270] and for the ions[245]. Periodic boundary conditions were employed, using the particle mesh Ewald method to calculate the long-range electrostatics[246]. The real part of the electrostatic and van der Waals interactions were computed with a 10 Å cut-off. The SHAKE algorithm[170] was used to constrain bonds involving hydrogen atoms, allowing an integration time step of 2 fs. Simulations were performed at constant temperature (310 K) and pressure (1 bar). The POPC bilayer and water solvent were allowed to equilibrate around the protein during 200 ns of MD simulation. After energy minimization, the system was gradually heated to 310 K, maintaining the protein backbone atoms close to their cryo-EM position by applying a harmonic restraint. Then, 1 μs of production equilibrium MD was performed for each IO and OO state NKCC1.

4.5.2. Conformational CV design

To guide the exploration of such complex systems and transitions, we applied the OPES Explore algorithm, which requires the use of effective CVs to accelerate a meaningful sampling of the free energy surface. By combining OPES Explore with the DeepLDA CV that we developed, our simulations could capture the complex dynamical transitions between open conformations of the inner and outer vestibules of the transporter. Using the IO and OO state equilibrium MD simulations,

we selected all Cα-Cα pairs from all 12 TM helices, totaling to ~75,000 Cα-Cα distances. These were then subsequently filtered, eliminating intra TM pairs and keeping pairs only from adjacent helices. Then, we kept Cα-Cα pairs whose average distance was deemed a contact (< 10 Å) in the IO state, and not a contact in the OO state (> 10 Å) and vice versa. Finally, we retained Cα-Cα distances that were significantly different between the IO and OO state, by eliminating those whose average was within 2 standard deviations between states. This resulted in a carefully curated selection of 90 Cα-Cα distances (see also **Appendix Figure SI 2**). From each 1 μs long equilibrium MD, 50,000 data points per distance and per state, were then fed to DeepLDA[256]. This produced a deep learning collective variable (CV)where the IO state was defined as -2.6 and the OO state was defined as 2.6.

4.5.3. Water CV design

The conformational CV was sufficient for enhanced sampling simulations to transit between the IO and the OO state, but we observed that these simulations were getting trapped in a state with the outer vestibule open and highly solvated. To aid water flushing from the outer vestibule, and reduce steric hindrance of water impeding structural rearrangements, we included a second water-focused CV.

This CV consisted of the coordination number between a virtual atom placed in the center of the outer vestibule (**Appendix Figure SI 3**) and the oxygen atoms of water molecules[271,272]. The coordination was calculated using a switching function (see Formula 1) with the following parameters: r_0=8.0 Å, d_0=0, n=2 and m=8. This collective variable characterizes the water content of the outer vestibule, and, when its fluctuations were enhanced though a bias potential, we were able to obtain 16 IO ↔ OO state transitions.

$$s(r) = \frac{1 - \left(\frac{r - d_0}{r_0}\right)^n}{1 - \left(\frac{r - d_0}{r_0}\right)^m}$$

Formula 1. Switching function for the Outer Vestibule virtual atom – water coordination number

4.5.4. OPES Explore

We performed bidimensional OPES Explore[216] on the DeepLDA CV and outer vestibule water coordination CV, through PLUMED 2.8[273]. We set an initial barrier value of 20 kcal/mol, a kernel deposition rate of 500 steps and a 310 K temperature. The initial sigma was set to 0.1 and 0.3, and the minimum sigma was set to 0.05 and 0.15, for the conformational and water CV, respectively.

4.5.5. Fully loaded NKCC1 conformations and ion binding simulations

Fully loaded IO *human* NKCC1 was obtained by placing ions in their binding sites in accordance to their position in the zebrafish NKCC1 structure[32], except for the Na^+ cation which was placed in the center of mass of the coordinating atoms of the known Na2 binding site also identified in human NKCC1[34]. This conformational state was then simulated for 1 μs.

Fully loaded occluded *human* NKCC1 was obtained by applying distance restrictions to each ion and all coordinating atoms, from each ion's respective binding site. The application of these restraints, for 100 ns, led to a NKCC1 state with all four ions bound and inaccessible to the solvent from both extracellular and intracellular side of the membrane – a fully loaded occluded state. After restrictions were lifted, this state was maintained for 120 ns of equilibrium MD, after which NKCC1 transited into a fully loaded IO state.

Fully loaded OO human NKCC1 was obtained by starting from previous simulations[44], where NKCC1 was bound to bCl^- (Cl^- anion closest to the intracellular side), K^+ and the inhibitor bumetanide. Bumetanide was removed, K^+ was exchanged for a Na^+ from the solvent, and the outer vestibule was allowed to be filled with water. After equilibration, we ran OPES Explore simulation biasing two collective variables (CVs). The first CV was the distance between the center of mass of the Na^+ site coordinating atoms and the Na^+ cation, currently bound to the K^+ site. The second CV was the coordination number between the Na^+ cation and the coordinating atoms of the Na^+ site. We then selected a snapshot where the Na^+ cation was within its binding site and ran 100 ns of equilibrium MD. We observed that bCl^- and Na^+ both stayed in their respective binding site through the 100 ns of simulation. We then selected the closest K^+ to the outer vestibule from the solvent and ran a second OPES Explore over two similar CVs, but instead considering the K^+ cation and the K^+ binding site coordinating atoms. Then, a snapshot where K^+ was bound to its site was selected and used for an equilibrium MD. After an initial run of 100 ns we observed that not only bCl^-, Na^+ and K^+ remained in their respective binding sites, but spontaneous binding of tCl^- to the top Cl^- binding site was observed very soon after the equilibrium MD started. Given that this last simulation was of NKCC1 in an OO fully loaded state we extended it to 1 μs.

Na^+ and Cl^- binding calculations were performed as described in the previous paragraph. OPES Explore simulations of Na^+ binding started from a snapshot from our unloaded OO state NKCC1 equilibrium MD simulation. A snapshot where a Na^+ ion was nearby the outer vestibule was selected,

and bias was applied to the distance between the ion and the center of mass of the coordinating atoms of Na^+ binding site, and to the coordination number between Na^+ and the coordinating atoms. OPES Explore simulations of Cl^- binding started from the previously equilibrated MD simulation of Na^+/Cl^--bound OO state NKCC1, using the same set of collective variables, considering Cl^- and its respective binding site. Ion binding order to the OO state of NKCC1 (Na^+, Cl^-, K^+, Cl^-) was determined from experimental evidence[21].

For the OPES Explore simulations of NKCC1 loading, the barrier was set to 5 kcal/mol, a kernel deposition rate of 500 steps and a 310 K temperature. Both initial and minimum sigma were set to adaptive for both collective variables. The coordination for all ions was calculated using a switching function (see Formula 1) with the following parameters: r_0=2.35 Å, d_0=0, n=2 and m=8.

4.5.6. Water permeability and transport

Water permeability was defined as the presence of a network of water molecules, connected by a distance of at most 4.00 Å between oxygen atoms from water molecules, that encompassed the whole ion translocation pathway, connecting the extracellular and intracellular solvent (**Figure 20**).

To determine water transport in our simulations we tracked each individual water molecule. An efflux event was determined to have happened when a water molecule crossed the inner membrane leaflet plane, the plane of the membrane bilayer, and then the outer membrane leaflet plane in this sequence specifically. An influx event was determined to have happened by a water molecule going through these planes in the reverse direction. Analysis were mostly performed with the MD analysis package[274].

4.5.7. Generation of NKCC1 mutants and Cl^- influx assay

Generation of mutants. Mutants of residues located in TM 6 and TM 10 in *mouse* NKCC1 (Ala490 (TM 6), Leu664 (TM 10), Asn665 (TM 10), Ala668 (TM 10), mutating to Ala or Trp) were designed based on MD simulations. NKCC1 mutants (Ala490Trp, Leu664Ala, Asn665Ala, Ala668Trp) were designed starting from the full-length mouse NKCC1 WT protein sequence cloned in the vector pRK5 (obtained from Medical Research Council and the University of Dundee). The mutants were prepared by GenScript. For each mutant, the lyophilized DNA was resuspended and used to transform E. Coli TOP10 competent cells, and a maxi prep was performed to purify the DNA of each mutant. The sequences were then confirmed by Sanger sequencing.

Cl influx assay. HEK293F cells were cultured in Dulbecco's modified Eagle medium (DMEM) supplemented with 10% fetal bovine serum, 1% L-glutamine, 100 U/mL penicillin, and 100µg/mL

streptomycin, and maintained at 37°C in a 5% CO2 humidified atmosphere. To assess WT and mutant NKCC1 activity, 3 million HEK cells were plated in a 10 cm cell-culture dish and transfected with a transfection mixture comprising 5mL of DMEM, 4mL Opti-MEM, 8µg of DNA plasmid (pRK5 vector) coding for NKCC1-WT, NKCC1-A490W, NKCC1-L664A, NKCC1-N665A, NKCC1-A668W, or mock control (empty vector), together with 8µg of a plasmid coding for the Cl -sensitive variant of the mbYFPQS (Addgene plasmid #80742), and 32µL of Lipofectamin 2000. After 4 h, the cells were collected and plated in 96-well black-walled, clear-bottomed plates at a density of 250,000 cells/well. After 48h, cells were used for the Cl influx assay. All reagents were purchased from Life Technologies, unless otherwise specified. The Cl-influx assay was performed in transfected cells treated with DMSO in 200 µL/well of a Cl -free-hypotonic solution (67.5mM Na Gluconate, 2.5mM K Gluconate, 15mM HEPES pH 7.4, 5mM Glucose, 1mM Na_2HPO_4, 1mM NaH_2PO_4, 1mM $MgSO_4$, 1mM $CaSO_4$). After 30 min of incubation, plates were loaded into a multi-plate reader (Tecan Spark) equipped with an automatic liquid injector system, and fluorescence of Cl-sensitive mbYFPQS was recorded with excitation at 485 nm and emission at 535 nm. For each well, fluorescence was first recorded for 20 sec of baseline and for 60 sec after delivery of a NaCl concentrated solution (74mM final concentration in assay well). Fluorescence of Cl-sensitive mbYFPQS is inversely correlated to the intracellular Cl^- concentration, therefore, Cl influx into the cells determined a decrease of mbYFPQS fluorescence. To quantify the average effects as represented by the bar plots, we expressed the decrease in fluorescence upon NaCl application as the average of the last 10 s of ΔF/F0 normalized traces. Moreover, for each experiment, to account for the contribution of Cl^- changes that were dependent on transporters/exchangers other than NKCC1, we subtracted the value of the last 10 s of ΔF/F0 normalized traces obtained from mock-transfected control cells from the respective ΔF/F0 value obtained from the cells transfected with WT or mutated NKCC1s. We then presented in the figure all the data as a percentage of the fluorescence decrease vs the value of the WT NKCC1-transfected cells.

Chapter 5:
Concluding Remarks

In this thesis, I delved deep into the significance of cation chloride cotransporters (CCCs), a pivotal family of transporters intricately linked with numerous neuropathologies. Our research aimed to contribute insights to the existing body of knowledge surrounding these captivating proteins. Yet, the vast expanse of the function and mechanism of CCCs still holds many enigmas.

Our primary focus was on deciphering the conformational transition mechanism of NKCC1. However, it is worth noting that our approach was based on a simplified model, employing monomeric NKCC1 within a pure POPC membrane. While our simulations led to conclusions that found resonance with experimental data, and even inspired mutagenesis studies, they remain, at their core, simplifications. A more intricate exploration could consider the effects of a heterogeneous membrane, mirroring the lipid composition found in the brain. Such an approach would allow us to discern the specific lipids crucial for the optimal function of NKCC1 and those that are inconsequential. Furthermore, the lipid binding sites nestled within the dimeric interface of NKCC1 beckon further investigation to shed light on their purpose. Our work, at the very least, provides a foundational model for future researchers to juxtapose their findings against, especially when introducing more complex variables.

By exclusively studying monomeric transporters, I sidestepped the potential implications of dimerization on CCC function and mechanisms. Questions abound: How does dimeric NKCC1 influence its angular motion and solvent accessibility? Are the motions of each monomer independent, or is there an interplay between them? Existing research indicates that the monomers in dimers appear to rotate between inward-open and outward-open conformational states. What triggers this rotation? Is it a recurring event within each transport cycle, or is it instigated by phosphorylation (or dephosphorylation in Na^+-independent CCCs) leading to a rotation that permits ion transport?

The realm of CCCs is replete with questions, and our time to explore them is finite. I remain hopeful that future research will unravel these mysteries, including those yet to be conceived. These unasked questions may very well prove to be the most enlightening. My journey through this topic has been nothing short of enthralling, and I am profoundly grateful for the opportunity to have dedicated these years to such a riveting subject. My aspiration has always been to make a meaningful contribution,

however modest. I extend my heartfelt gratitude to all who accompanied me on this enlightening journey.

Appendix

Chapter 4: Supporting information

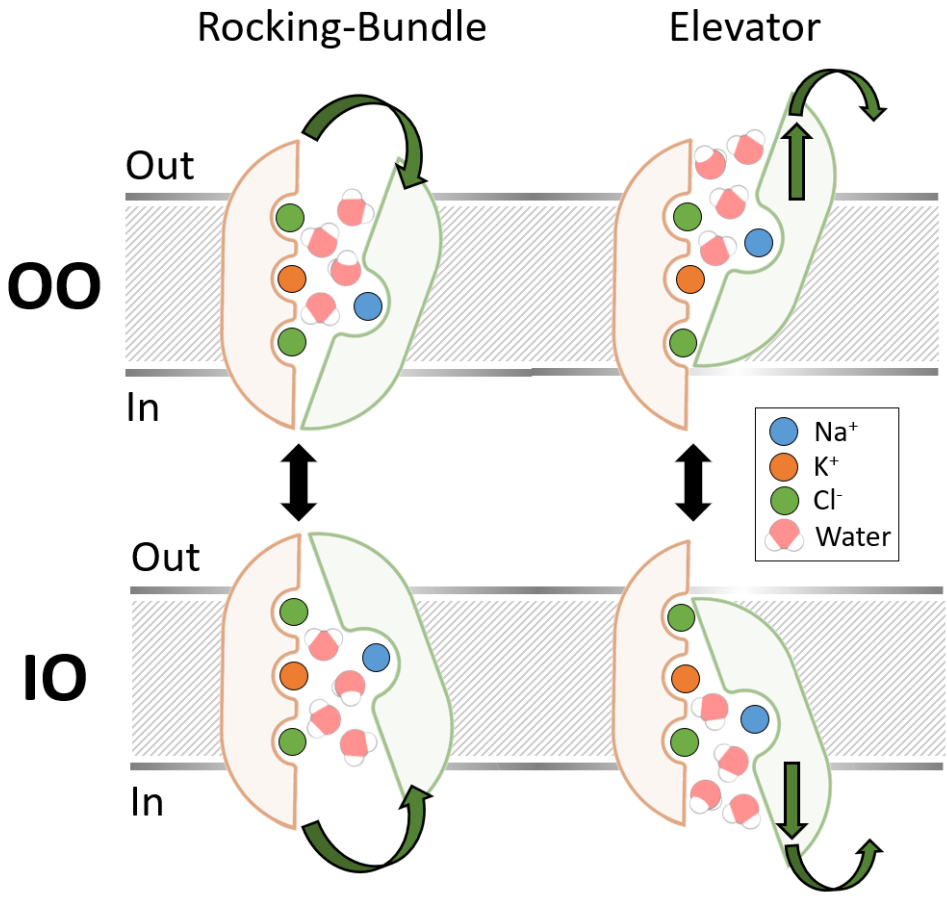

Figure SI 1: Different types of Alternating Access Mechanisms previously identified for the LeuT-fold transporters suggest possible conformational transition routes in NKCC1. On the left, the Rocking-Bundle Mechanism, where the mobile domain (light green) carries out an angular motion that alternates binding site accessibility to either side of the membrane. On the right, the Elevator Mechanism, where the mobile domain (light green) goes through vertical translation and an angular motion, to carry out alternation of binding-site accessibility.

A

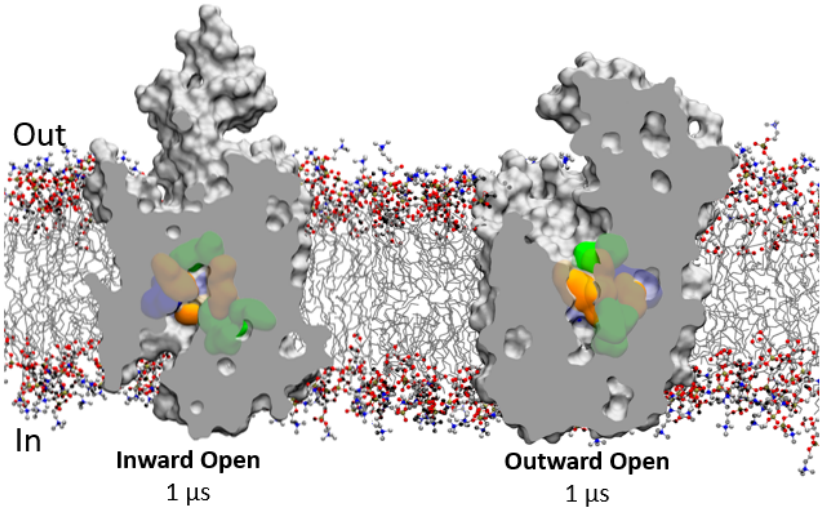

B

CV based on transmembrane helix Cα-Cα distances

75,000 Cα-Cα distances

Filters

1. No intra TM pairs
2. Only Cα-Cα pairs from neighboring TMs
3. Contacts in IO and not in OO, and vice versa
4. Cα-Cα distances are significantly different

90 Cα-Cα distances

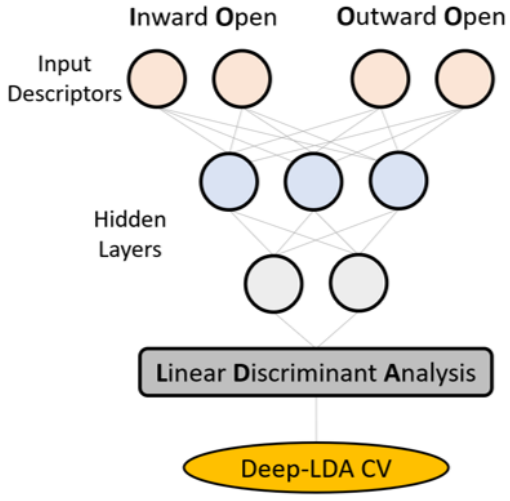

C

Filter 1.

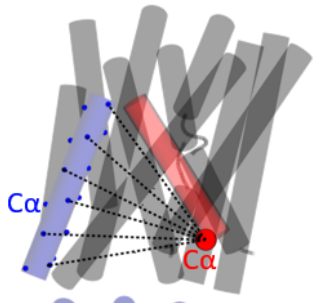

Filter 2.

Filter 3.

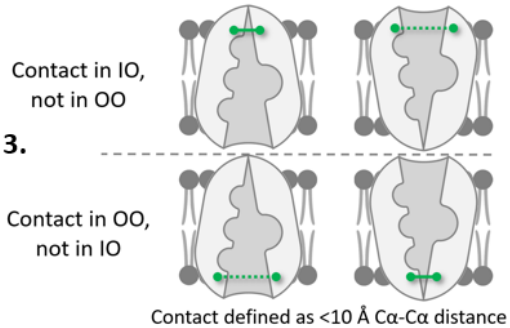

Filter 4.

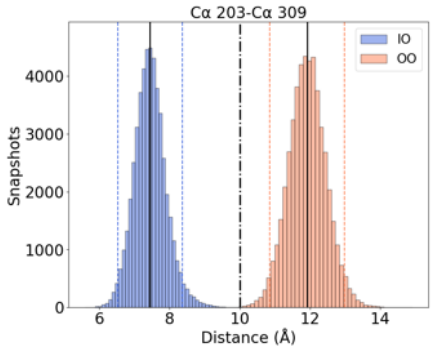

Figure SI 2: Collective variable design based on Deep Learning algorithms, which was essential for the elucidation of mechanism of NKCC1's conformational transitions. To explore the conformational transition between NKCC1's Inward Open and Outward Open states we looked for a collective variable with as little user input as possible. We used the Cα-Cα distances. We filtered and selected the Cα-Cα distances that had the capacity to pave the way for conformational exploration through OPES Explore. Our dataset was based on two independent equilibrium MD simulations of human NKCC1: 50,000 snapshots from 1 μs of Inward Open state, and other 50,000 snapshots from 1 μs of Outward Open state – (A) representation of both NKCC1 IO and OO states embedded in a membrane, coming from both our equilibrium MD simulations. (B) Diagram of the workflow to design the CV: From both states, we calculated all possible Cα-Cα distances from the 12 TM helices – in total ~75,000 pairs. We excluded from this initial step Cα-Cα pairs belonging to the same helix (e.g. residue 5 and residue 7 belong to TM 1, therefore their respective Cα was not calculated – C, Filter 1), and we excluded all pairs from non-neighboring helices (e.g. residue 5 and residue 55 belong to TM 4 and TM 11, who are too far apart to ever create or break bonds between them – C, Filter 2). We calculated the average distance for each Cα-Cα distance, and then kept for further analysis those whose average distance was defined as a contact (<10 Å) in one state, and not a contact (>10 Å) in the opposite state (C, Filter 3). Then, we kept only those Cα-Cα distances whose distribution was significantly different between the IO and OO state (C, Filter 4). This set of filters left us with 90 Cα-Cα distances that defined the conformational space between the NKCC1 IO and OO state. In this way, our dataset was constituted of 90 Cα-Cα distances over 100,000 equilibrium MD snapshots (50,000 from the IO state, and 50,000 from the OO state). This dataset was then fed into DeepLDA, which then generated a unidimensional collective variable. This variable describes as -2.6 the Cα-Cα distance distribution of the IO state and 2.6 the Cα-Cα distance distribution of the OO state.

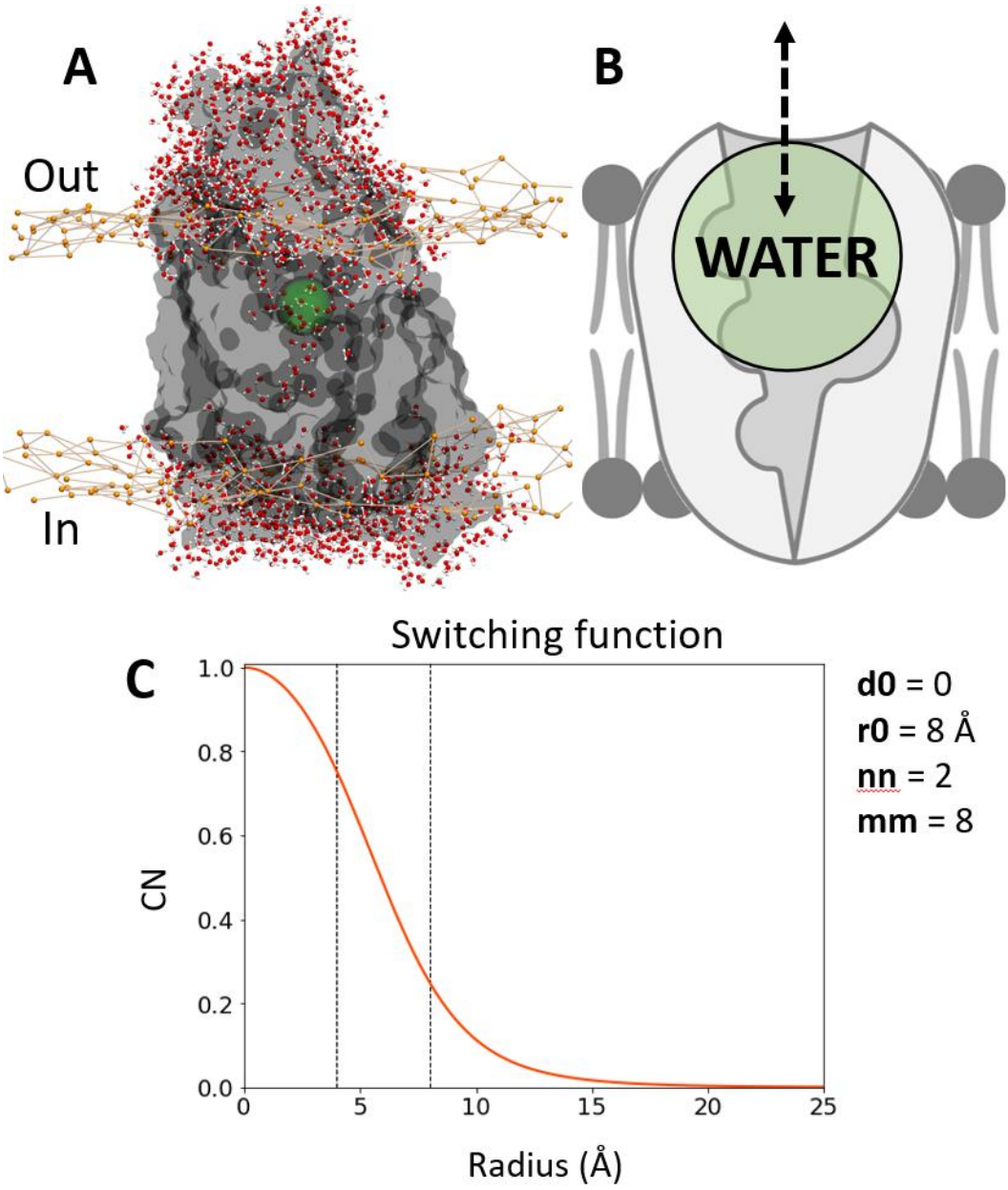

Figure SI 3: Collective variable design to account for water flow into the outer vestibule was necessary to efficiently sample the NKCC1 Inward Open ↔ Outward Open conformational transition. (A) Representation of human NKCC1, shown as a grey atomic surface, embedded in the cell membrane (orange wireframe with spheres), with a thick layer of water molecules (white sticks with a red sphere) around the protein and flooding the outer vestibule. The green sphere represents the location of where the virtual atom was positioned to calculate water oxygen coordination of the outer vestibule in all OPES Explore simulations. (B) Schematic representation of NKCC1 (light brown) embedded in the membrane , along with the virtual atom used to calculate water oxygen coordination (green circle). The dashed arrow showcases the direction of the water flow. (C) Plot of the switching function used to calculate water-oxygen coordination from the virtual atom placed in the outer vestibule. Dashed black lines highlight the coordination values of a water oxygen atom at 4 Å and 8 Å.

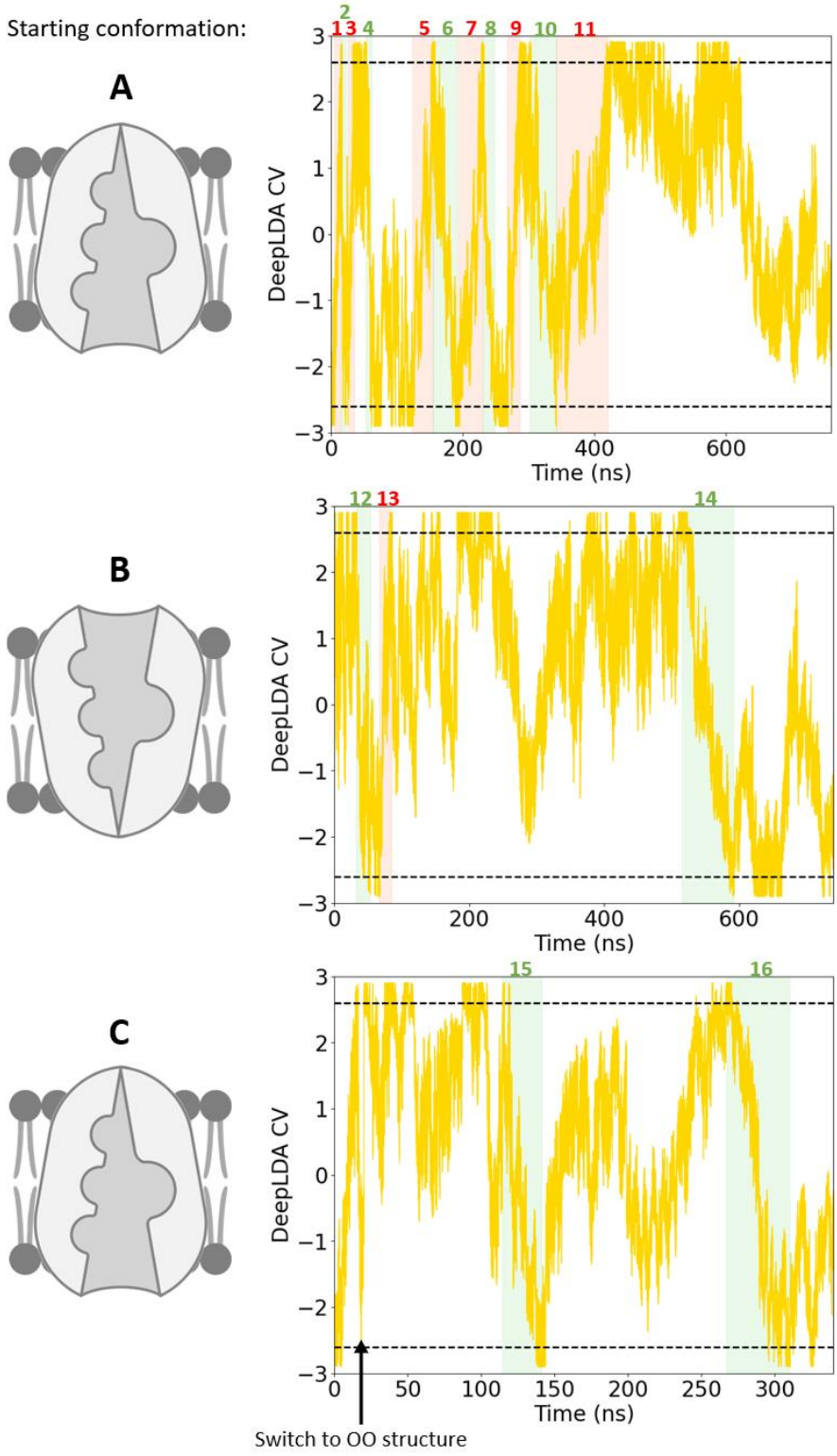

Figure SI 4: The DeepLDA CV and the coordination of water oxygens in the outer vestibule CV were succesfully used by OPES Explore to elucidate the Inward Open ↔ Outward Open NKCC1 conformational transition. (A-C) DeepLDA CV *vs* the simulation time of OPES Explore. IO → OO transitions are highlighted in red. OO → IO are highlighted in green. These simulations started from the IO

state (A) or the OO state (B) , (C) corresponds to the plot of the first 20 ns of the IO starting simulations, whose structure was then manually exchanged to the OO structure. The dashed lines indicates -2.6 and 2.6, the values assigned by DeepLDA to the IO and OO state, respectively. The black arrow indicates when the structure was exchanged.

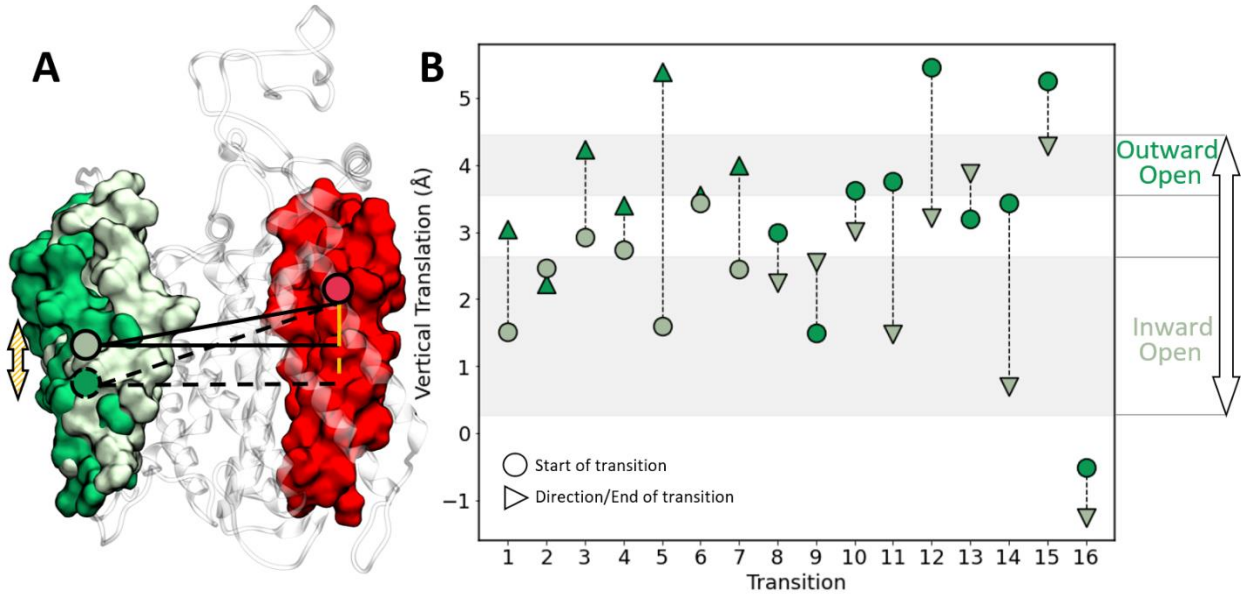

Figure SI 5: NKCC1 does not present vertical translation during its conformational transition between the Inward Open ↔ Outward Open conformations. (A) Schematic representation of NKCC1's vertical translation, defined as the difference between the Z coordinate of the center of mass of TM 4 and TM 9 (green surface for the TMs, green circles for the center of mass) *vs* the center of mass of TM 1, TM 2, TM 6 and TM 7 (the static domain, red surface for the TMs, red circle for the center of mass), between the OO and the IO state – bright and dim green, respectively. Black and dashed lines illustrate the relationship between centers of mass, yellow dashed line shows the quantified value in the Z coordinate. The striped arrow shows the expected vertical translation for the elevator mechanism. (B) Quantification of NKCC1's vertical translation of TM 4 and TM 9 with respect to TM 2 and TM 7 through 16 conformational transitions from OPES Explore simulations. The light brown horizontal bars represent the OO and IO average vertical translation ± 1SD from 1 μs of equilibrium molecular dynamic (MD) simulations. Circles represent the starting point of each transition, whereas the triangles represent the endpoint of the same transition and its direction. Circles and triangles are colored depending on the NKCC1 conformation they represent (bright green for OO and dim green for IO).

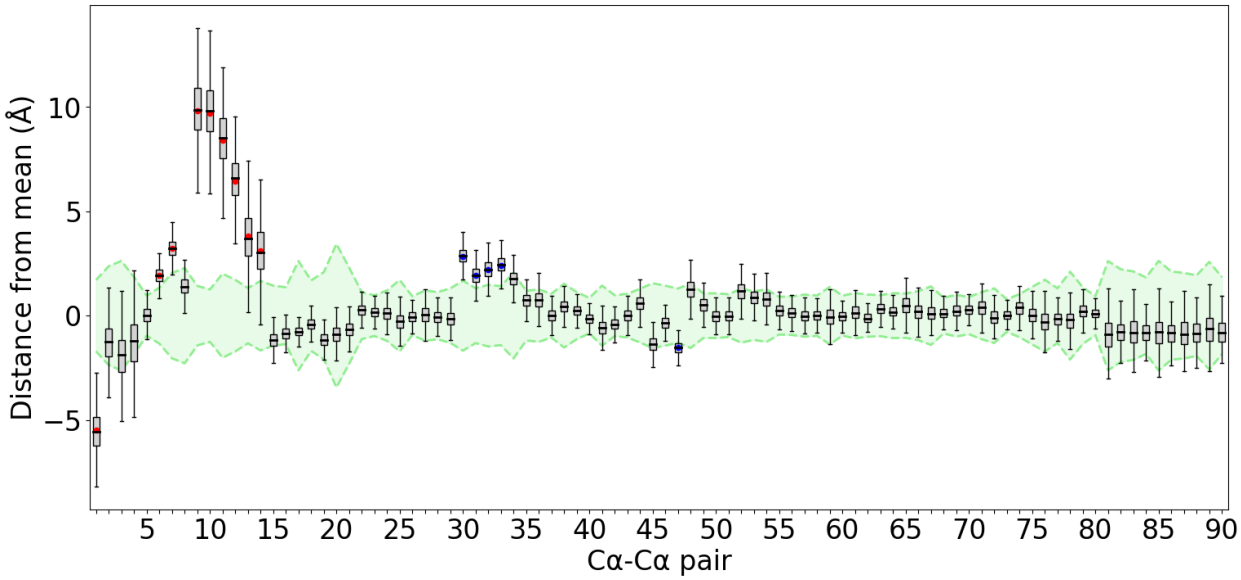

Figure SI 6: The shift from -2.6 of the DeepLDA CV value can be explained by the deviation of few Cα-Cα distances belonging to the first few residues of the NKCC1 model. Box plot distribution of the Cα -Cα pair distances from their respective MD mean in the IO state equilibrium. Those were calculated for all 90 distances that defined the DeepLDA CV. The 90 distances were measured from an equilibrium MD starting from a snapshot belonging to the IO basin in the FES. IO state equilibrium MD distance distribution is shown in green. Distances from residues belonging to the first bend of TM 1, far from their expected values, are highlighted in red. Distances highlighted in blue lay just outside their expected distribution, but did not lead to any structural determinant event.

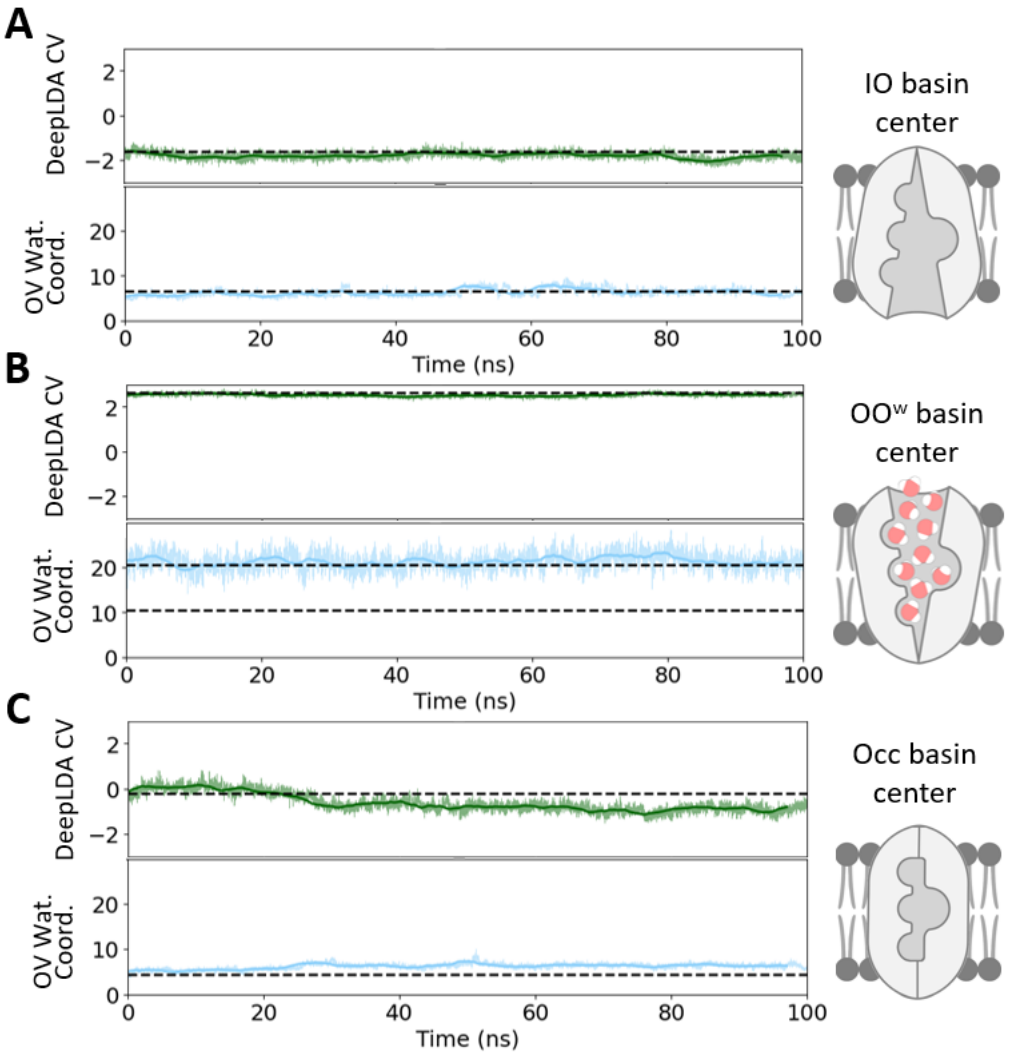

Figure SI 7: Equilibrium MD shows that snapshots from the FES's basins represent stable NKCC1 conformational states. (A-C) Plots of projections from equilibrium MDs of DeepLDA CV (top, green) and Water Coordination CV (bottom, blue). The equilibrium MD started from snapshots belonging to IO (A), OO^{w} (B) and Occ (C) basins in the FES shown in Figure 7. The respective schematic representation on the right shows NKCC1 conformations at the corresponding basins, represented by dotted lines in the plots.

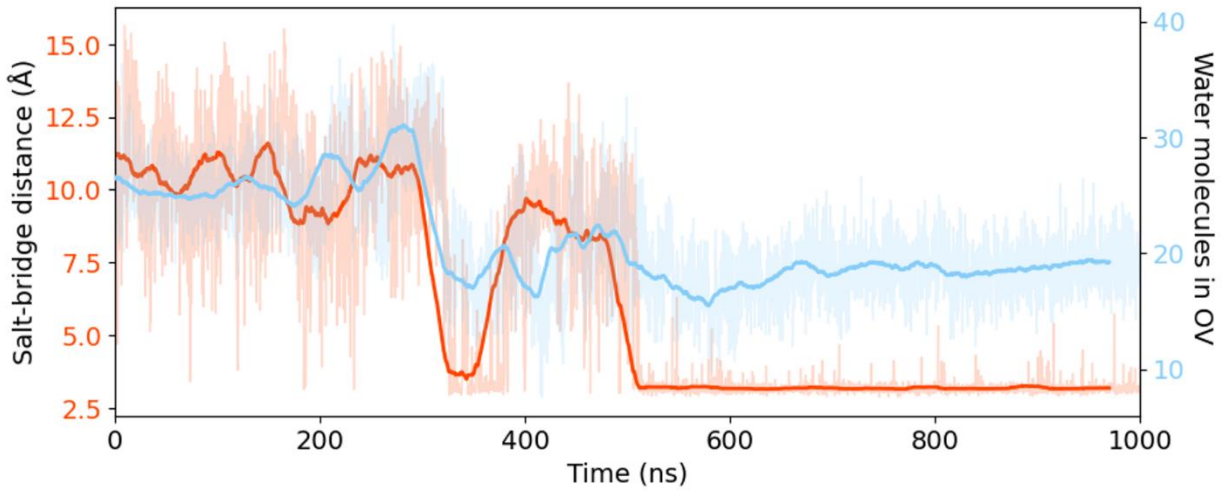

Figure SI 8: Decrease of outer vestibule hydration is correlated with the formation of a salt bridge in the Outward Open state equilibrium MD. Distance between charged atoms from the sidechains of salt-bridge forming residues Arg307 and Glu389 during the OO state equilibrium MD (orange), and the number of water molecules in the outer vestibule (OV, blue) during the same simulation.

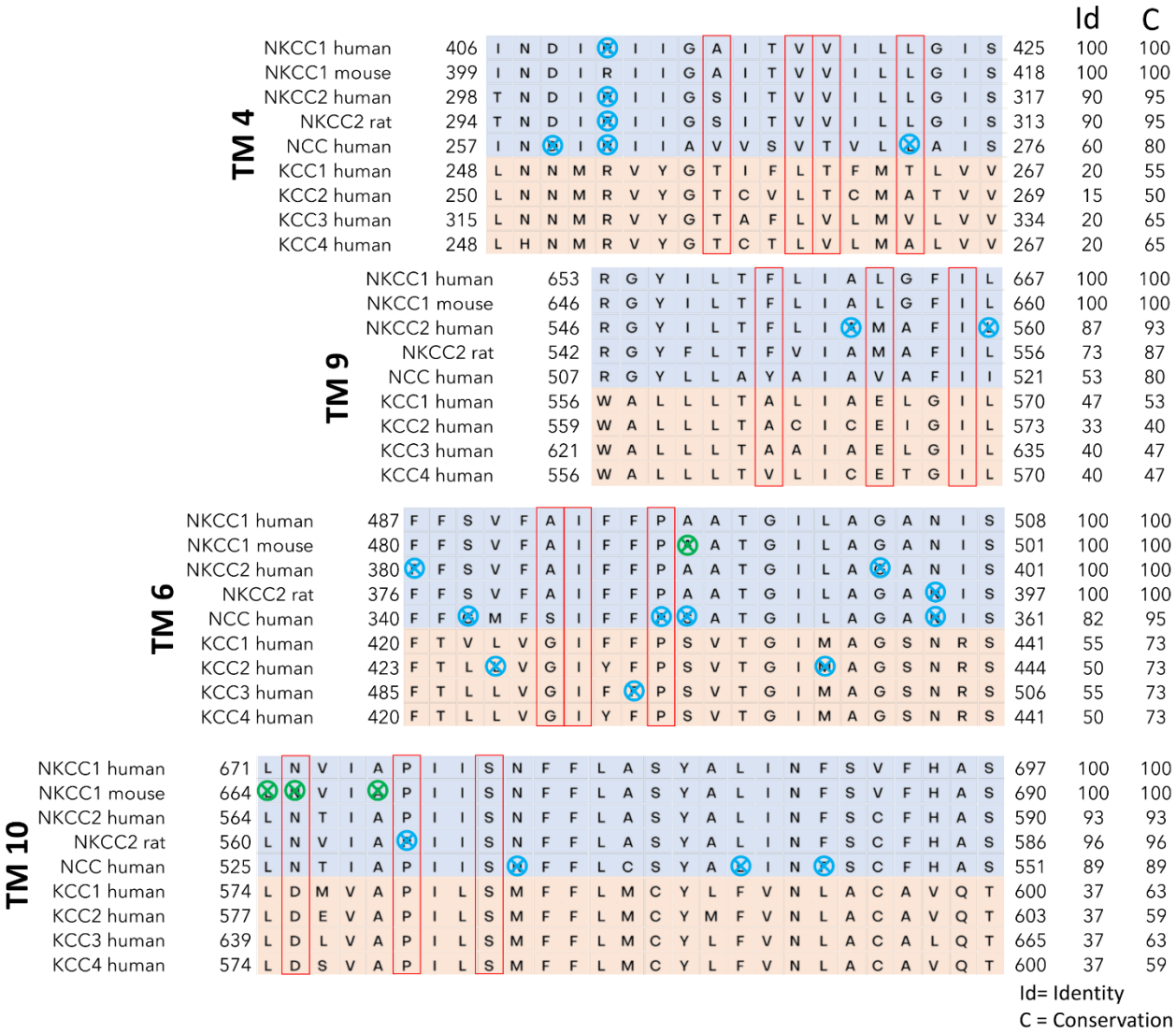

Figure SI 9: Alignment of NKCC1 with other CCC functionally relevant TMs show high conservation in Na^+-dependent transporters, low conservation in Na^+-independent transporters and prevalence of disease-associated mutation in only Na^+ dependent transporters. Multiple sequence alignment of CCC's TM 4, 9, 6 and 10. Red rectangles highlight residues that participate in TM interactions relevant for our proposed rocking-bundle alternating access mechanism. Green circles highlight mutations used for our *in vitro* Cl^- flux assay experiments performed on *mouse* NKCC1. Blue circles highlight mutations associated to human disease, as described in the literature[41].

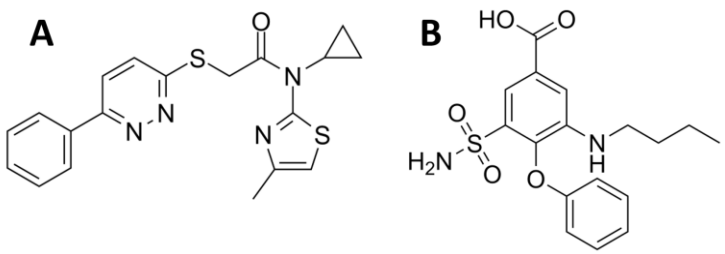

Figure SI 10: Chemical structure of CCC inhibitors. (A) Shows VU0463271, referenced in Chapter 1.1.5 and Chapter 3. (B) Shows bumetanide, also referenced in Chapter 1.1.5.

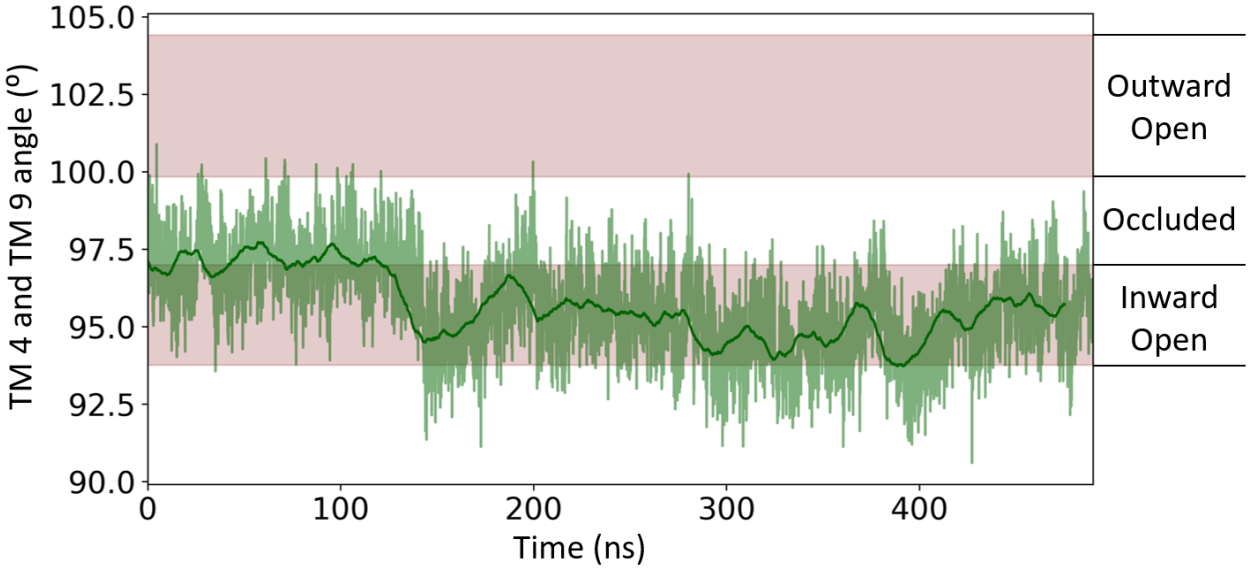

Figure SI 11: Fully loaded NKCC1 conformational transition undergoes the same molecular motions as unloaded NKCC1. Angular motion of TM 4 and TM 9 of fully loaded NKCC1 in the occluded conformational states. Equilibrium MD simulation of this state shows how the angular motions reflect an occluded state for the first 120ns, followed by a conformational transition into the fully loaded inward open state – where it stayed for the rest of the trajectory.

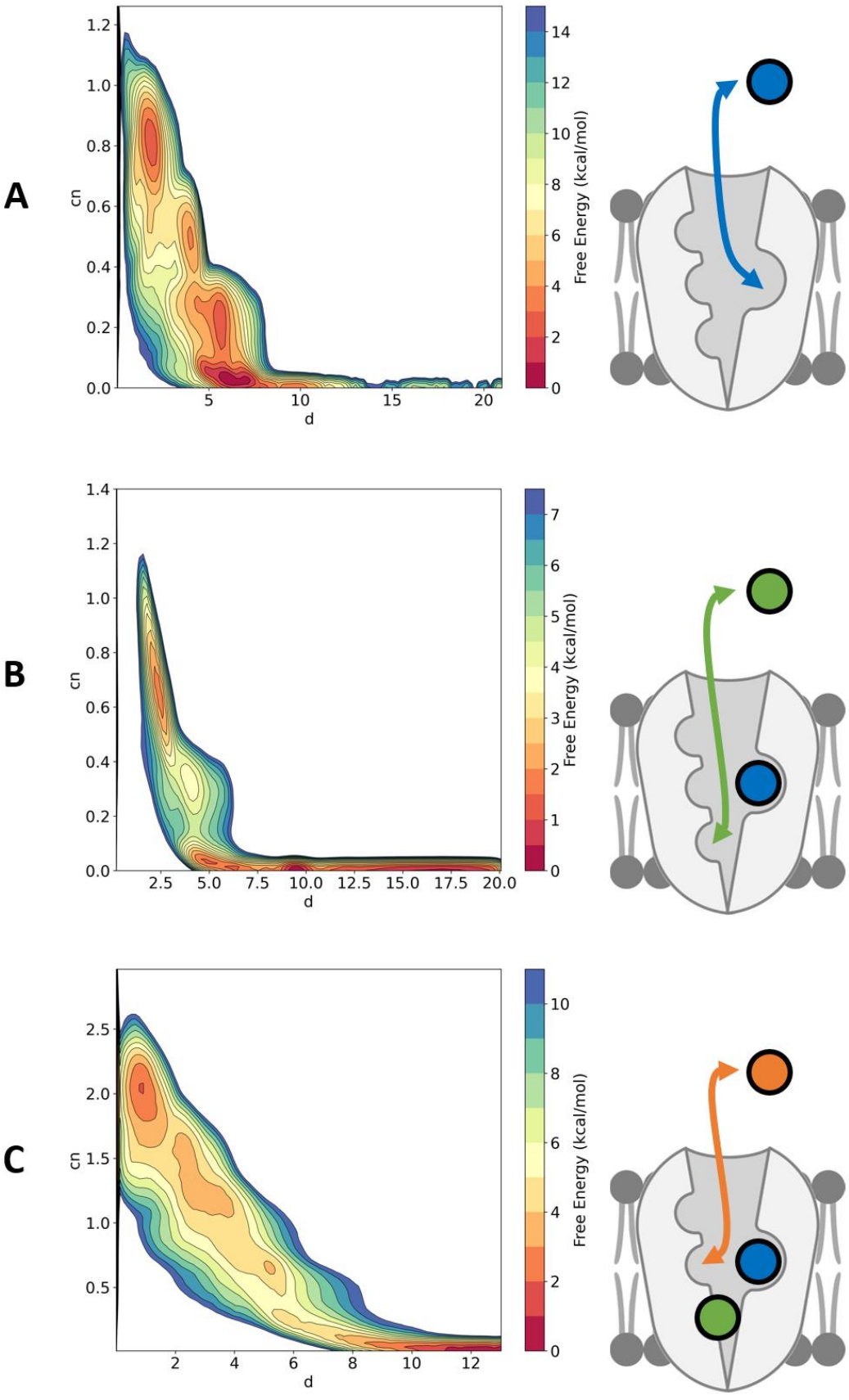
A
B
C
cn
d
Free Energy (kcal/mol)

Figure SI 12: Free Energy Surface of ion binding simulations. FES calculated by reweighting from OPES Explore simulations, biasing the distance between the relevant ion and the center of mass of the coordinating atoms and the coordination number of the coordinating atoms with respect to the ion. (A) FES for Na^+ binding in unloaded NKCC1. (B) FES for Cl^- binding in Na-loaded NKCC1. (C) FES for K^+ binding to Cl/Na-loaded NKCC1.

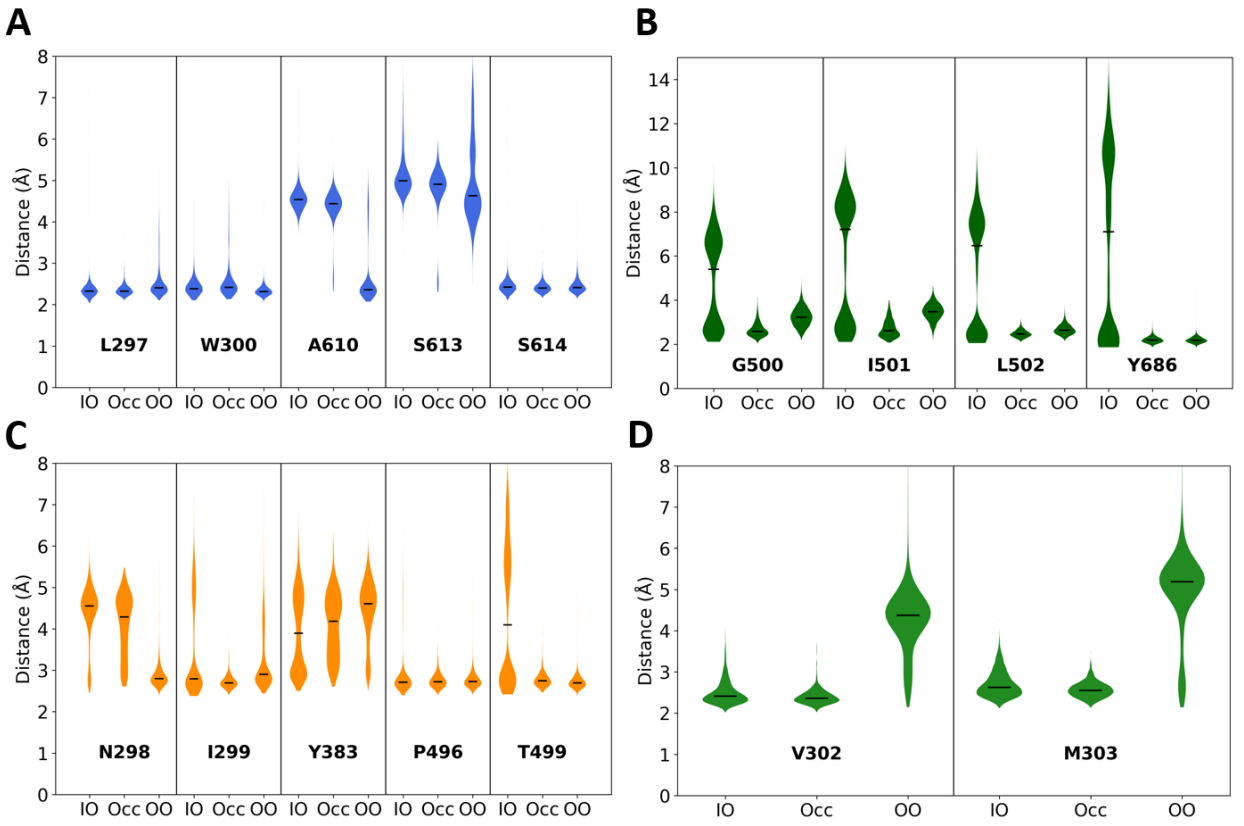

Figure SI 13: Binding mode of ions undergoes few changes during NKCC1's conformational transition. Violin plots represent the distribution of distances between the bound ion and the coordinating atoms from the respective binding site. (A) Distance distribution between Na^+ and its binding site, composed of oxygen atoms from residues: L297, W300, A610, S613, S614. In all fully loaded NKCC1 states, Na^+ remains tightly bound to L297, W300 and S614, and loosely bound to S613. On the other hand, interactions of Na^+ and A610 change during the conformational transition, starting tightly bound in the OO state, and loosely bound in both Occ and IO states. (B) Distance distribution between Cl^- and its binding site (closest to the intracellular side), composed by hydrogen atoms of residues: G500, I501, L502, Y686. bCl- remains tightly bound in all NKCC1 fully loaded states. We note that the distance distribution in the IO state is bimodal, where the lower distance mode represents a tightly bound Cl^-, and the higher distance mode represents states where bCl^- visits a secondary binding site. This site is in the vicinity of the intracellular gate (as identified by Janoš & Magistrato, 2021) and likely represents a state pre-ion release. (C) Distance distribution between K^+ and its binding site, composed of oxygen atoms of residues: N298, I299, Y383, P496, T499. In our fully loaded simulations K^+ remains tightly bound to I299 and P496, and loosely bound to Y383. Interactions between the bound K^+ and N298 change during the conformational transition, starting tightly bound in the OO state and becoming loosely bound in the Occ and IO states. Interactions with T499 also change during the conformational transition, although this change occurs at a different stage. In both OO and Occ states, K^+ remains tightly bound, but becomes loosely bound in the IO state. (D) Distance distribution between Cl^- and its binding site (closest to the extracellular side), composed by hydrogen atoms of residues: V302 and M303. Cl^- remains tightly bound to both residues in the Occ and IO state, and loosely bound to both residues in the OO state. This is consistent with the fact that Cl^- spontaneously binds and unbinds in the equilibrium MD of the OO state – but then having its interactions stabilized as NKCC1's conformationally transitions into the Occ state.

Bibliography

(1) Brodie III, E. D. Patterns, Process, and the Parable of the Coffeepot Incident: Arms Races between Newts and Snakes from Landscapes to Molecules. *Light Evol. Essays Lab. Field Roberts Co. Greenwood Village CO* **2011**, 93–120.

(2) Association, P. Doctors Fear Spread of "super-Gonorrhoea" across Britain. *The Guardian*. April 17, 2016. https://www.theguardian.com/society/2016/apr/17/gonorrhoea-will-spread-across-uk-doctors-fear (accessed 2023-10-04).

(3) Zarantonelli, L.; Borthagaray, G.; Lee, E.-H.; Shafer, W. M. Decreased Azithromycin Susceptibility of Neisseria Gonorrhoeae Due to mtrR Mutations. *Antimicrob. Agents Chemother.* **1999**, *43* (10), 2468–2472.

(4) Gamba, G. Molecular Physiology and Pathophysiology of Electroneutral Cation-Chloride Cotransporters. *Physiol. Rev.* **2005**, *85* (2), 423–493. https://doi.org/10.1152/physrev.00011.2004.

(5) Bazúa-Valenti, S.; Castañeda-Bueno, M.; Gamba, G. Physiological Role of SLC12 Family Members in the Kidney. *Am. J. Physiol.-Ren. Physiol.* **2016**, *311* (1), F131–F144. https://doi.org/10.1152/ajprenal.00071.2016.

(6) Kaila, K.; Price, T. J.; Payne, J. A.; Puskarjov, M.; Voipio, J. Cation-Chloride Cotransporters in Neuronal Development, Plasticity and Disease. *Nat. Rev. Neurosci.* **2014**, *15* (10), 637–654. https://doi.org/10.1038/nrn3819.

(7) Payne, J. A.; Rivera, C.; Voipio, J.; Kaila, K. Cation–Chloride Co-Transporters in Neuronal Communication, Development and Trauma. *Trends Neurosci.* **2003**, *26* (4), 199–206. https://doi.org/10.1016/S0166-2236(03)00068-7.

(8) Starremans, P. G. J. F.; Kersten, F. F. J.; van den Heuvel, L. P. W. J.; Knoers, N. V. A. M.; Bindels, R. J. M. Dimeric Architecture of the Human Bumetanide-Sensitive Na-K-Cl Co-Transporter. *J. Am. Soc. Nephrol.* **2003**, *14* (12), 3039. https://doi.org/10.1097/01.ASN.0000097370.29737.5B.

(9) Monette, M. Y.; Forbush, B. Regulatory Activation Is Accompanied by Movement in the C Terminus of the Na-K-Cl Cotransporter (NKCC1). *J. Biol. Chem.* **2012**, *287* (3), 2210–2220. https://doi.org/10.1074/jbc.M111.309211.

(10) Uvarov, P.; Ludwig, A.; Markkanen, M.; Soni, S.; Hübner, C. A.; Rivera, C.; Airaksinen, M. S. Coexpression and Heteromerization of Two Neuronal K-Cl Cotransporter Isoforms in Neonatal Brain. *J. Biol. Chem.* **2009**, *284* (20), 13696–13704. https://doi.org/10.1074/jbc.M807366200.

(11) Yamashita, A.; Singh, S. K.; Kawate, T.; Jin, Y.; Gouaux, E. Crystal Structure of a Bacterial Homologue of Na+/Cl--Dependent Neurotransmitter Transporters. *Nature* **2005**, *437* (7056), 215–223. https://doi.org/10.1038/nature03978.

(12) Kahle, K. T.; Rinehart, J.; Lifton, R. P. Phosphoregulation of the Na–K–2Cl and K–Cl Cotransporters by the WNK Kinases. *Biochim. Biophys. Acta BBA - Mol. Basis Dis.* **2010**, *1802* (12), 1150–1158. https://doi.org/10.1016/j.bbadis.2010.07.009.

(13) Morita, Y.; Callicott, J. H.; Testa, L. R.; Mighdoll, M. I.; Dickinson, D.; Chen, Q.; Tao, R.; Lipska, B. K.; Kolachana, B.; Law, A. J.; Ye, T.; Straub, R. E.; Weinberger, D. R.; Kleinman, J. E.; Hyde, T. M. Characteristics of the Cation Cotransporter NKCC1 in Human Brain: Alternate Transcripts, Expression in Development, and Potential Relationships to Brain Function and Schizophrenia. *J. Neurosci.* **2014**, *34* (14), 4929–4940. https://doi.org/10.1523/JNEUROSCI.1423-13.2014.

(14) Isenring, P.; Forbush, B. Ion Transport and Ligand Binding by the Na–K–Cl Cotransporter, Structure–Function Studies. *Comp. Biochem. Physiol. A. Mol. Integr. Physiol.* **2001**, *130* (3), 487–497. https://doi.org/10.1016/S1095-6433(01)00420-2.

(15) Delpire, E.; Wolfe, L.; Flores, B.; Koumangoye, R.; Schornak, C. C.; Omer, S.; Pusey, B.; Lau, C.; Markello, T.; Adams, D. R. A Patient with Multisystem Dysfunction Carries a Truncation Mutation

in Human SLC12A2, the Gene Encoding the Na-K-2Cl Cotransporter, NKCC1. *Mol. Case Stud.* **2016**, *2* (6), a001289. https://doi.org/10.1101/mcs.a001289.
(16) Somasekharan, S.; Tanis, J.; Forbush, B. Loop Diuretic and Ion-Binding Residues Revealed by Scanning Mutagenesis of Transmembrane Helix 3 (TM3) of Na-K-Cl Cotransporter (NKCC1). *J. Biol. Chem.* **2012**, *287* (21), 17308–17317. https://doi.org/10.1074/jbc.M112.356014.
(17) Warmuth, S.; Zimmermann, I.; Dutzler, R. X-Ray Structure of the C-Terminal Domain of a Prokaryotic Cation-Chloride Cotransporter. *Structure* **2009**, *17* (4), 538–546. https://doi.org/10.1016/j.str.2009.02.009.
(18) Agez, M.; Schultz, P.; Medina, I.; Baker, D. J.; Burnham, M. P.; Cardarelli, R. A.; Conway, L. C.; Garnier, K.; Geschwindner, S.; Gunnarsson, A.; McCall, E. J.; Frechard, A.; Audebert, S.; Deeb, T. Z.; Moss, S. J.; Brandon, N. J.; Wang, Q.; Dekker, N.; Jawhari, A. Molecular Architecture of Potassium Chloride Co-Transporter KCC2. *Sci. Rep.* **2017**, *7* (1), 16452. https://doi.org/10.1038/s41598-017-15739-1.
(19) De Jong, J. C.; Willems, P. H. G. M.; Mooren, F. J. M.; Van Den Heuvel, L. P. W. J.; Knoers, N. V. A. M.; Bindels, R. J. M. The Structural Unit of the Thiazide-Sensitive NaCl Cotransporter Is a Homodimer. *J. Biol. Chem.* **2003**, *278* (27), 24302–24307. https://doi.org/10.1074/jbc.M303101200.
(20) Bai, X.; Moraes, T. F.; Reithmeier, R. A. F. Structural Biology of Solute Carrier (SLC) Membrane Transport Proteins. *Mol. Membr. Biol.* **2017**, *34* (1–2), 1–32. https://doi.org/10.1080/09687688.2018.1448123.
(21) Lytle, C.; McManus, T. J.; Haas, M. A Model of Na-K-2Cl Cotransport Based on Ordered Ion Binding and Glide Symmetry. *Am. J. Physiol.-Cell Physiol.* **1998**, *274* (2), C299–C309. https://doi.org/10.1152/ajpcell.1998.274.2.C299.
(22) Krishnamurthy, H.; Piscitelli, C. L.; Gouaux, E. Unlocking the Molecular Secrets of Sodium-Coupled Transporters. *Nature* **2009**, *459* (7245), 347–355. https://doi.org/10.1038/nature08143.
(23) Krishnamurthy, H.; Gouaux, E. X-Ray Structures of LeuT in Substrate-Free Outward-Open and Apo Inward-Open States. *Nature* **2012**, *481* (7382), 469–474. https://doi.org/10.1038/nature10737.
(24) Shimamura, T.; Weyand, S.; Beckstein, O.; Rutherford, N. G.; Hadden, J. M.; Sharples, D.; Sansom, M. S. P.; Iwata, S.; Henderson, P. J. F.; Cameron, A. D. Molecular Basis of Alternating Access Membrane Transport by the Sodium-Hydantoin Transporter Mhp1. *Science* **2010**, *328* (5977), 470–473. https://doi.org/10.1126/science.1186303.
(25) Fang, Y.; Jayaram, H.; Shane, T.; Kolmakova-Partensky, L.; Wu, F.; Williams, C.; Xiong, Y.; Miller, C. Structure of a Prokaryotic Virtual Proton Pump at 3.2 Å Resolution. *Nature* **2009**, *460* (7258), 1040–1043. https://doi.org/10.1038/nature08201.
(26) Perez, C.; Koshy, C.; Yildiz, Ö.; Ziegler, C. Alternating-Access Mechanism in Conformationally Asymmetric Trimers of the Betaine Transporter BetP. *Nature* **2012**, *490* (7418), 126–130. https://doi.org/10.1038/nature11403.
(27) Shaffer, P. L.; Goehring, A.; Shankaranarayanan, A.; Gouaux, E. Structure and Mechanism of a Na+-Independent Amino Acid Transporter. *Science* **2009**, *325* (5943), 1010–1014. https://doi.org/10.1126/science.1176088.
(28) Faham, S.; Watanabe, A.; Besserer, G. M.; Cascio, D.; Specht, A.; Hirayama, B. A.; Wright, E. M.; Abramson, J. The Crystal Structure of a Sodium Galactose Transporter Reveals Mechanistic Insights into Na+/Sugar Symport. *Science* **2008**, *321* (5890), 810–814. https://doi.org/10.1126/science.1160406.
(29) Tang, L.; Bai, L.; Wang, W.; Jiang, T. Crystal Structure of the Carnitine Transporter and Insights into the Antiport Mechanism. *Nat. Struct. Mol. Biol.* **2010**, *17* (4), 492–496. https://doi.org/10.1038/nsmb.1788.

(30) Wahlgren, W. Y.; Dunevall, E.; North, R. A.; Paz, A.; Scalise, M.; Bisignano, P.; Bengtsson-Palme, J.; Goyal, P.; Claesson, E.; Caing-Carlsson, R.; Andersson, R.; Beis, K.; Nilsson, U. J.; Farewell, A.; Pochini, L.; Indiveri, C.; Grabe, M.; Dobson, R. C. J.; Abramson, J.; Ramaswamy, S.; Friemann, R. Substrate-Bound Outward-Open Structure of a Na+-Coupled Sialic Acid Symporter Reveals a New Na+ Site. *Nat. Commun.* **2018**, *9* (1), 1753. https://doi.org/10.1038/s41467-018-04045-7.

(31) Shi, Y. Common Folds and Transport Mechanisms of Secondary Active Transporters. *Annu. Rev. Biophys.* **2013**, *42* (1), 51–72. https://doi.org/10.1146/annurev-biophys-083012-130429.

(32) Chew, T. A.; Orlando, B. J.; Zhang, J.; Latorraca, N. R.; Wang, A.; Hollingsworth, S. A.; Chen, D.-H.; Dror, R. O.; Liao, M.; Feng, L. Structure and Mechanism of the Cation–Chloride Cotransporter NKCC1. *Nature* **2019**, *572* (7770), 488–492. https://doi.org/10.1038/s41586-019-1438-2.

(33) Liu, S.; Chang, S.; Han, B.; Xu, L.; Zhang, M.; Zhao, C.; Yang, W.; Wang, F.; Li, J.; Delpire, E.; Ye, S.; Bai, X.; Guo, J. Cryo-EM Structures of the Human Cation-Chloride Cotransporter KCC1. *Science* **2019**, *366* (6464), 505–508. https://doi.org/10.1126/science.aay3129.

(34) Yang, X.; Wang, Q.; Cao, E. Structure of the Human Cation–Chloride Cotransporter NKCC1 Determined by Single-Particle Electron Cryo-Microscopy. *Nat. Commun.* **2020**, *11* (1), 1016. https://doi.org/10.1038/s41467-020-14790-3.

(35) Zhao, Y.; Shen, J.; Wang, Q.; Ruiz Munevar, M. J.; Vidossich, P.; De Vivo, M.; Zhou, M.; Cao, E. Structure of the Human Cation–Chloride Cotransport KCC1 in an Outward-Open State. *Proc. Natl. Acad. Sci.* **2022**, *119* (27), e2109083119. https://doi.org/10.1073/pnas.2109083119.

(36) Xie, Y.; Chang, S.; Zhao, C.; Wang, F.; Liu, S.; Wang, J.; Delpire, E.; Ye, S.; Guo, J. Structures and an Activation Mechanism of Human Potassium-Chloride Cotransporters. *Sci. Adv.* **2020**, *6* (50), eabc5883. https://doi.org/10.1126/sciadv.abc5883.

(37) Chi, X.; Li, X.; Chen, Y.; Zhang, Y.; Su, Q.; Zhou, Q. Cryo-EM Structures of the Full-Length Human KCC2 and KCC3 Cation-Chloride Cotransporters. *Cell Res.* **2021**, *31* (4), 482–484. https://doi.org/10.1038/s41422-020-00437-x.

(38) Zhang, S.; Zhou, J.; Zhang, Y.; Liu, T.; Friedel, P.; Zhuo, W.; Somasekharan, S.; Roy, K.; Zhang, L.; Liu, Y.; Meng, X.; Deng, H.; Zeng, W.; Li, G.; Forbush, B.; Yang, M. The Structural Basis of Function and Regulation of Neuronal Cotransporters NKCC1 and KCC2. *Commun. Biol.* **2021**, *4* (1), 226. https://doi.org/10.1038/s42003-021-01750-w.

(39) Fan, M.; Zhang, J.; Lee, C.-L.; Zhang, J.; Feng, L. Structure and Thiazide Inhibition Mechanism of the Human Na–Cl Cotransporter. *Nature* **2023**, *614* (7949), 788–793. https://doi.org/10.1038/s41586-023-05718-0.

(40) Reid, M. S.; Kern, D. M.; Brohawn, S. G. Cryo-EM Structure of the Potassium-Chloride Cotransporter KCC4 in Lipid Nanodiscs. *eLife* **2020**, *9*, e52505. https://doi.org/10.7554/eLife.52505.

(41) Portioli, C.; Ruiz Munevar, M. J.; De Vivo, M.; Cancedda, L. Cation-Coupled Chloride Cotransporters: Chemical Insights and Disease Implications. *Trends Chem.* **2021**, *3* (10), 832–849. https://doi.org/10.1016/j.trechm.2021.05.004.

(42) Steffensen, A. B.; Oernbo, E. K.; Stoica, A.; Gerkau, N. J.; Barbuskaite, D.; Tritsaris, K.; Rose, C. R.; MacAulay, N. Cotransporter-Mediated Water Transport Underlying Cerebrospinal Fluid Formation. *Nat. Commun.* **2018**, *9* (1), 2167. https://doi.org/10.1038/s41467-018-04677-9.

(43) Monette, M. Y.; Rinehart, J.; Lifton, R. P.; Forbush, B. Rare Mutations in the Human Na-K-Cl Cotransporter (NKCC2) Associated with Lower Blood Pressure Exhibit Impaired Processing and Transport Function. *Am. J. Physiol.-Ren. Physiol.* **2011**, *300* (4), F840–F847. https://doi.org/10.1152/ajprenal.00552.2010.

(44) Zhao, Y.; Roy, K.; Vidossich, P.; Cancedda, L.; De Vivo, M.; Forbush, B.; Cao, E. Structural Basis for Inhibition of the Cation-Chloride Cotransporter NKCC1 by the Diuretic Drug Bumetanide. *Nat. Commun.* **2022**, *13* (1), 2747. https://doi.org/10.1038/s41467-022-30407-3.

(45) Delpire, E.; Days, E.; Lewis, L. M.; Mi, D.; Kim, K.; Lindsley, C. W.; Weaver, C. D. Small-Molecule Screen Identifies Inhibitors of the Neuronal K-Cl Cotransporter KCC2. *Proc. Natl. Acad. Sci.* **2009**, *106* (13), 5383–5388. https://doi.org/10.1073/pnas.0812756106.

(46) Dehaye, J. P.; Nagy, A.; Premkumar, A.; Turner, R. J. Identification of a Functionally Important Conformation-Sensitive Region of the Secretory Na+-K+-2Cl− Cotransporter (NKCC1). *J. Biol. Chem.* **2003**, *278* (14), 11811–11817. https://doi.org/10.1074/jbc.M213148200.

(47) Watanabe, M.; Wake, H.; Moorhouse, A. J.; Nabekura, J. Clustering of Neuronal K+-Cl− Cotransporters in Lipid Rafts by Tyrosine Phosphorylation. *J. Biol. Chem.* **2009**, *284* (41), 27980–27988. https://doi.org/10.1074/jbc.M109.043620.

(48) Rinehart, J.; Maksimova, Y. D.; Tanis, J. E.; Stone, K. L.; Hodson, C. A.; Zhang, J.; Risinger, M.; Pan, W.; Wu, D.; Colangelo, C. M.; Forbush, B.; Joiner, C. H.; Gulcicek, E. E.; Gallagher, P. G.; Lifton, R. P. Sites of Regulated Phosphorylation That Control K-Cl Cotransporter Activity. *Cell* **2009**, *138* (3), 525–536. https://doi.org/10.1016/j.cell.2009.05.031.

(49) Darman, R. B.; Forbush, B. A Regulatory Locus of Phosphorylation in the N Terminus of the Na-K-Cl Cotransporter, NKCC1. *J. Biol. Chem.* **2002**, *277* (40), 37542–37550. https://doi.org/10.1074/jbc.M206293200.

(50) Watanabe, M.; Zhang, J.; Mansuri, M. S.; Duan, J.; Karimy, J. K.; Delpire, E.; Alper, S. L.; Lifton, R. P.; Fukuda, A.; Kahle, K. T. Developmentally Regulated KCC2 Phosphorylation Is Essential for Dynamic GABA-Mediated Inhibition and Survival. *Sci. Signal.* **2019**, *12* (603), eaaw9315. https://doi.org/10.1126/scisignal.aaw9315.

(51) Lee, H. H. C.; Jurd, R.; Moss, S. J. Tyrosine Phosphorylation Regulates the Membrane Trafficking of the Potassium Chloride Co-Transporter KCC2. *Mol. Cell. Neurosci.* **2010**, *45* (2), 173–179. https://doi.org/10.1016/j.mcn.2010.06.008.

(52) Kahle, K. T.; Wilson, F. H.; Leng, Q.; Lalioti, M. D.; O'Connell, A. D.; Dong, K.; Rapson, A. K.; MacGregor, G. G.; Giebisch, G.; Hebert, S. C.; Lifton, R. P. WNK4 Regulates the Balance between Renal NaCl Reabsorption and K+ Secretion. *Nat. Genet.* **2003**, *35* (4), 372–376. https://doi.org/10.1038/ng1271.

(53) Wang, D.; Zhang, Y.; Han, J.; Pan, S.; Xu, N.; Feng, X.; Zhuang, Z.; Caroti, C.; Zhuang, J.; Hoover, R. S.; Gu, D.; Zeng, Q.; Cai, H. WNK3 Kinase Enhances the Sodium Chloride Cotransporter Expression via an ERK 1/2 Signaling Pathway. *Nephron* **2016**, *133* (4), 287–295. https://doi.org/10.1159/000447717.

(54) Cordshagen, A.; Busch, W.; Winklhofer, M.; Nothwang, H. G.; Hartmann, A.-M. Phosphoregulation of the Intracellular Termini of K+-Cl− Cotransporter 2 (KCC2) Enables Flexible Control of Its Activity. *J. Biol. Chem.* **2018**, *293* (44), 16984–16993. https://doi.org/10.1074/jbc.RA118.004349.

(55) Ponce-Coria, J.; San-Cristobal, P.; Kahle, K. T.; Vazquez, N.; Pacheco-Alvarez, D.; de los Heros, P.; Juárez, P.; Muñoz, E.; Michel, G.; Bobadilla, N. A.; Gimenez, I.; Lifton, R. P.; Hebert, S. C.; Gamba, G. Regulation of NKCC2 by a Chloride-Sensing Mechanism Involving the WNK3 and SPAK Kinases. *Proc. Natl. Acad. Sci.* **2008**, *105* (24), 8458–8463. https://doi.org/10.1073/pnas.0802966105.

(56) Richardson, C.; Sakamoto, K.; de los Heros, P.; Deak, M.; Campbell, D. G.; Prescott, A. R.; Alessi, D. R. Regulation of the NKCC2 Ion Cotransporter by SPAK-OSR1-Dependent and -Independent Pathways. *J. Cell Sci.* **2011**, *124* (5), 789–800. https://doi.org/10.1242/jcs.077230.

(57) Zhang, J.; Gao, G.; Begum, G.; Wang, J.; Khanna, A. R.; Shmukler, B. E.; Daubner, G. M.; de los Heros, P.; Davies, P.; Varghese, J.; Bhuiyan, M. I. H.; Duan, J.; Zhang, J.; Duran, D.; Alper, S. L.; Sun, D.; Elledge, S. J.; Alessi, D. R.; Kahle, K. T. Functional Kinomics Establishes a Critical Node of Volume-Sensitive Cation-Cl− Cotransporter Regulation in the Mammalian Brain. *Sci. Rep.* **2016**, *6* (1), 35986. https://doi.org/10.1038/srep35986.

(58) de los Heros, P.; Alessi, D. R.; Gourlay, R.; Campbell, D. G.; Deak, M.; Macartney, T. J.; Kahle, K. T.; Zhang, J. The WNK-Regulated SPAK/OSR1 Kinases Directly Phosphorylate and Inhibit the K+–Cl– Co-Transporters. *Biochem. J.* **2014**, *458* (3), 559–573. https://doi.org/10.1042/BJ20131478.
(59) Gagnon, K. B.; Delpire, E. Multiple Pathways for Protein Phosphatase 1 (PP1) Regulation of Na-K-2Cl Cotransporter (NKCC1) Function. *J. Biol. Chem.* **2010**, *285* (19), 14115–14121. https://doi.org/10.1074/jbc.M110.112672.
(60) Vitari, A. C.; Thastrup, J.; Rafiqi, F. H.; Deak, M.; Morrice, N. A.; Karlsson, H. K. R.; Alessi, D. R. Functional Interactions of the SPAK/OSR1 Kinases with Their Upstream Activator WNK1 and Downstream Substrate NKCC1. *Biochem. J.* **2006**, *397* (1), 223–231. https://doi.org/10.1042/BJ20060220.
(61) Darman, R. B.; Flemmer, A.; Forbush, B. Modulation of Ion Transport by Direct Targeting of Protein Phosphatase Type 1 to the Na-K-Cl Cotransporter. *J. Biol. Chem.* **2001**, *276* (37), 34359–34362. https://doi.org/10.1074/jbc.C100368200.
(62) Fukuda, A.; Watanabe, M. Pathogenic Potential of Human SLC12A5 Variants Causing KCC2 Dysfunction. *Brain Res.* **2019**, *1710*, 1–7. https://doi.org/10.1016/j.brainres.2018.12.025.
(63) Weng, T.-Y.; Chiu, W.-T.; Liu, H.-S.; Cheng, H.-C.; Shen, M.-R.; Mount, D. B.; Chou, C.-Y. Glycosylation Regulates the Function and Membrane Localization of KCC4. *Biochim. Biophys. Acta BBA - Mol. Cell Res.* **2013**, *1833* (5), 1133–1146. https://doi.org/10.1016/j.bbamcr.2013.01.018.
(64) Wang, L.; Dong, C.; Xi, Y.-G.; Su, X. Thiazide-Sensitive Na⁺–Cl[−] Cotransporter: Genetic Polymorphisms and Human Diseases. *Acta Biochim. Biophys. Sin.* **2015**, *47* (5), 325–334. https://doi.org/10.1093/abbs/gmv020.
(65) Hoover, R. S.; Poch, E.; Monroy, A.; Vázquez, N.; Nishio, T.; Gamba, G.; Hebert, S. C. N-Glycosylation at Two Sites Critically Alters Thiazide Binding and Activity of the Rat Thiazide-Sensitive Na+: Cl: −: Cotransporter. *J. Am. Soc. Nephrol.* **2003**, *14* (2), 271. https://doi.org/10.1097/01.ASN.0000043903.93452.D0.
(66) Stödberg, T.; McTague, A.; Ruiz, A. J.; Hirata, H.; Zhen, J.; Long, P.; Farabella, I.; Meyer, E.; Kawahara, A.; Vassallo, G.; Stivaros, S. M.; Bjursell, M. K.; Stranneheim, H.; Tigerschiöld, S.; Persson, B.; Bangash, I.; Das, K.; Hughes, D.; Lesko, N.; Lundeberg, J.; Scott, R. C.; Poduri, A.; Scheffer, I. E.; Smith, H.; Gissen, P.; Schorge, S.; Reith, M. E. A.; Topf, M.; Kullmann, D. M.; Harvey, R. J.; Wedell, A.; Kurian, M. A. Mutations in SLC12A5 in Epilepsy of Infancy with Migrating Focal Seizures. *Nat. Commun.* **2015**, *6* (1), 8038. https://doi.org/10.1038/ncomms9038.
(67) Rosenbaek, L. L.; Rizzo, F.; Wu, Q.; Rojas-Vega, L.; Gamba, G.; MacAulay, N.; Staub, O.; Fenton, R. A. The Thiazide Sensitive Sodium Chloride Co-Transporter NCC Is Modulated by Site-Specific Ubiquitylation. *Sci. Rep.* **2017**, *7* (1), 12981. https://doi.org/10.1038/s41598-017-12819-0.
(68) Zeng, Y.; Li, P.; Fang, S.; Wu, C.; Zhang, Y.; Lin, X.; Guan, M. Genetic Analysis of SLC12A3 Gene in Chinese Patients with Gitelman Syndrome. *Med. Sci. Monit.* **2019**, *25*, 5942–5952. https://doi.org/10.12659/MSM.916069.
(69) Fanis, P.; Efstathiou, E.; Neocleous, V.; Phylactou, L. A.; Hadjipanayis, A. A Novel Heterozygous Duplication of the SLC12A3 Gene in Two Gitelman Syndrome Pedigrees: Indicating a Founder Effect. *J. Genet.* **2019**, *98* (1), 5. https://doi.org/10.1007/s12041-019-1056-7.
(70) De la Cruz-Cano, E.; Jiménez-González, C. del C.; Morales-García, V.; Pineda-Pérez, C.; Tejas-Juárez, J. G.; Rendón-Gandarilla, F. J.; Jiménez-Morales, S.; Díaz-Gandarilla, J. A. Arg913Gln Variation of SLC12A3 Gene Is Associated with Diabetic Nephropathy in Type 2 Diabetes and Gitelman Syndrome: A Systematic Review. *BMC Nephrol.* **2019**, *20* (1), 393. https://doi.org/10.1186/s12882-019-1590-9.
(71) Glaudemans, B.; Yntema, H. G.; San-Cristobal, P.; Schoots, J.; Pfundt, R.; Kamsteeg, E.-J.; Bindels, R. J.; Knoers, N. V.; Hoenderop, J. G.; Hoefsloot, L. H. Novel NCC Mutants and Functional Analysis

in a New Cohort of Patients with Gitelman Syndrome. *Eur. J. Hum. Genet.* **2012**, *20* (3), 263–270. https://doi.org/10.1038/ejhg.2011.189.

(72) Tang, W.; Huang, X.; Liu, Y.; Lv, Q.; Li, T.; Song, Y.; Zhang, X.; Chen, X.; Shi, Y. A Novel Homozygous Mutation (p.N958K) of SLC12A3 in Gitelman Syndrome Is Associated with Endoplasmic Reticulum Stress. *J. Endocrinol. Invest.* **2021**, *44* (3), 471–480. https://doi.org/10.1007/s40618-020-01329-y.

(73) Tseng, M.-H.; Yang, S.-S.; Hsu, Y.-J.; Fang, Y.-W.; Wu, C.-J.; Tsai, J.-D.; Hwang, D.-Y.; Lin, S.-H. Genotype, Phenotype, and Follow-Up in Taiwanese Patients with Salt-Losing Tubulopathy Associated with SLC12A3 Mutation. *J. Clin. Endocrinol. Metab.* **2012**, *97* (8), E1478–E1482. https://doi.org/10.1210/jc.2012-1707.

(74) Acuña, R.; Martínez-de-la-Maza, L.; Ponce-Coria, J.; Vázquez, N.; Ortal-Vite, P.; Pacheco-Alvarez, D.; Bobadilla, N. A.; Gamba, G. Rare Mutations in SLC12A1 and SLC12A3 Protect against Hypertension by Reducing the Activity of Renal Salt Cotransporters. *J. Hypertens.* **2011**, *29* (3), 475. https://doi.org/10.1097/HJH.0b013e328341d0fd.

(75) Schultheis, P. J.; Lorenz, J. N.; Meneton, P.; Nieman, M. L.; Riddle, T. M.; Flagella, M.; Duffy, J. J.; Doetschman, T.; Miller, M. L.; Shull, G. E. Phenotype Resembling Gitelman's Syndrome in Mice Lacking the Apical Na+-Cl− Cotransporter of the Distal Convoluted Tubule. *J. Biol. Chem.* **1998**, *273* (44), 29150–29155. https://doi.org/10.1074/jbc.273.44.29150.

(76) Mutai, H.; Wasano, K.; Momozawa, Y.; Kamatani, Y.; Miya, F.; Masuda, S.; Morimoto, N.; Nara, K.; Takahashi, S.; Tsunoda, T.; Homma, K.; Kubo, M.; Matsunaga, T. Variants Encoding a Restricted Carboxy-Terminal Domain of SLC12A2 Cause Hereditary Hearing Loss in Humans. *PLOS Genet.* **2020**, *16* (4), e1008643. https://doi.org/10.1371/journal.pgen.1008643.

(77) McNeill, A.; Iovino, E.; Mansard, L.; Vache, C.; Baux, D.; Bedoukian, E.; Cox, H.; Dean, J.; Goudie, D.; Kumar, A.; Newbury-Ecob, R.; Fallerini, C.; Renieri, A.; Lopergolo, D.; Mari, F.; Blanchet, C.; Willems, M.; Roux, A.-F.; Pippucci, T.; Delpire, E. SLC12A2 Variants Cause a Neurodevelopmental Disorder or Cochleovestibular Defect. *Brain* **2020**, *143* (8), 2380–2387. https://doi.org/10.1093/brain/awaa176.

(78) Merner, N. D.; Mercado, A.; Khanna, A. R.; Hodgkinson, A.; Bruat, V.; Awadalla, P.; Gamba, G.; Rouleau, G. A.; Kahle, K. T. Gain-of-Function Missense Variant in SLC12A2, Encoding the Bumetanide-Sensitive NKCC1 Cotransporter, Identified in Human Schizophrenia. *J. Psychiatr. Res.* **2016**, *77*, 22–26. https://doi.org/10.1016/j.jpsychires.2016.02.016.

(79) Macnamara, E. F.; Koehler, A. E.; D'Souza, P.; Estwick, T.; Lee, P.; Vezina, G.; Network, U. D.; Fauni, H.; Braddock, S. R.; Torti, E.; Holt, J. M.; Sharma, P.; Malicdan, M. C. V.; Tifft, C. J. Kilquist Syndrome: A Novel Syndromic Hearing Loss Disorder Caused by Homozygous Deletion of SLC12A2. *Hum. Mutat.* **2019**, *40* (5), 532–538. https://doi.org/10.1002/humu.23722.

(80) Koumangoye, R.; Omer, S.; Kabeer, M. H.; Delpire, E. Novel Human NKCC1 Mutations Cause Defects in Goblet Cell Mucus Secretion and Chronic Inflammation. *Cell. Mol. Gastroenterol. Hepatol.* **2020**, *9* (2), 239–255. https://doi.org/10.1016/j.jcmgh.2019.10.006.

(81) Flagella, M.; Clarke, L. L.; Miller, M. L.; Erway, L. C.; Giannella, R. A.; Andringa, A.; Gawenis, L. R.; Kramer, J.; Duffy, J. J.; Doetschman, T.; Lorenz, J. N.; Yamoah, E. N.; Cardell, E. L.; Shull, G. E. Mice Lacking the Basolateral Na-K-2Cl Cotransporter Have Impaired Epithelial Chloride Secretion and Are Profoundly Deaf. *J. Biol. Chem.* **1999**, *274* (38), 26946–26955. https://doi.org/10.1074/jbc.274.38.26946.

(82) Delpire, E.; Lu, J.; England, R.; Dull, C.; Thorne, T. Deafness and Imbalance Associated with Inactivation of the Secretory Na-K-2Cl Co-Transporter. *Nat. Genet.* **1999**, *22* (2), 192–195. https://doi.org/10.1038/9713.

(83) Gagnon, K. B.; Delpire, E. Physiology of SLC12 Transporters: Lessons from Inherited Human Genetic Mutations and Genetically Engineered Mouse Knockouts. *Am. J. Physiol.-Cell Physiol.* **2013**, *304* (8), C693–C714. https://doi.org/10.1152/ajpcell.00350.2012.

(84) Deidda, G.; Parrini, M.; Naskar, S.; Bozarth, I. F.; Contestabile, A.; Cancedda, L. Reversing Excitatory GABAAR Signaling Restores Synaptic Plasticity and Memory in a Mouse Model of Down Syndrome. *Nat. Med.* **2015**, *21* (4), 318–326. https://doi.org/10.1038/nm.3827.
(85) Han, Y.; Zhao, X.; Wang, S.; Wang, C.; Tian, D.; Lang, Y.; Bottillo, I.; Wang, X.; Shao, L. Eleven Novel SLC12A1 Variants and an Exonic Mutation Cause Exon Skipping in Bartter Syndrome Type I. *Endocrine* **2019**, *64* (3), 708–718. https://doi.org/10.1007/s12020-019-01856-6.
(86) Sun, M.; Ning, J.; Xu, W.; Zhang, H.; Zhao, K.; Li, W.; Li, G.; Li, S. Genetic Heterogeneity in Patients with Bartter Syndrome Type 1. *Mol. Med. Rep.* **2017**, *15* (2), 581–590. https://doi.org/10.3892/mmr.2016.6063.
(87) Ji, W.; Foo, J. N.; O'Roak, B. J.; Zhao, H.; Larson, M. G.; Simon, D. B.; Newton-Cheh, C.; State, M. W.; Levy, D.; Lifton, R. P. Rare Independent Mutations in Renal Salt Handling Genes Contribute to Blood Pressure Variation. *Nat. Genet.* **2008**, *40* (5), 592–599. https://doi.org/10.1038/ng.118.
(88) Halperin, D.; Dolgin, V.; Geylis, M.; Drabkin, M.; Yogev, Y.; Wormser, O.; Schreiber, R.; Shalev, H.; Landau, D.; Birk, O. S. A Novel SLC12A1 Mutation in Bedouin Kindred with Antenatal Bartter Syndrome Type I. *Ann. Hum. Genet.* **2019**, *83* (5), 361–366. https://doi.org/10.1111/ahg.12317.
(89) Brochard, K.; Boyer, O.; Blanchard, A.; Loirat, C.; Niaudet, P.; Macher, M.-A.; Deschenes, G.; Bensman, A.; Decramer, S.; Cochat, P.; Morin, D.; Broux, F.; Caillez, M.; Guyot, C.; Novo, R.; Jeunemaître, X.; Vargas-Poussou, R. Phenotype–Genotype Correlation in Antenatal and Neonatal Variants of Bartter Syndrome. *Nephrol. Dial. Transplant.* **2009**, *24* (5), 1455–1464. https://doi.org/10.1093/ndt/gfn689.
(90) Pressler, C. A.; Heinzinger, J.; Jeck, N.; Waldegger, P.; Pechmann, U.; Reinalter, S.; Konrad, M.; Beetz, R.; Seyberth, H. D. W.; Waldegger, S. Late-Onset Manifestation of Antenatal Bartter Syndrome as a Result of Residual Function of the Mutated Renal Na+-K+-2Cl− Co-Transporter. *J. Am. Soc. Nephrol.* **2006**, *17* (8), 2136. https://doi.org/10.1681/ASN.2005101071.
(91) Wongsaengsak, S.; Vidmar, A. P.; Addala, A.; Kamil, E. S.; Sequeira, P.; Fass, B.; Pitukcheewanont, P. A Novel SLC12A1 Gene Mutation Associated with Hyperparathyroidism, Hypercalcemia, Nephrogenic Diabetes Insipidus, and Nephrocalcinosis in Four Patients. *Bone* **2017**, *97*, 121–125. https://doi.org/10.1016/j.bone.2017.01.011.
(92) Breinbjerg, A.; Siggaard Rittig, C.; Gregersen, N.; Rittig, S.; Hvarregaard Christensen, J. A Novel Variant in the SLC12A1 Gene in Two Families with Antenatal Bartter Syndrome. *Acta Paediatr.* **2017**, *106* (1), 161–167. https://doi.org/10.1111/apa.13635.
(93) Starremans, P. G. J. F.; Kersten, F. F. J.; Knoers, N. V. A. M.; van den Heuvel, L. P. W. J.; Bindels, R. J. M. Mutations in the Human Na-K-2Cl Cotransporter (NKCC2) Identified in Bartter Syndrome Type I Consistently Result in Nonfunctional Transporters. *J. Am. Soc. Nephrol.* **2003**, *14* (6), 1419. https://doi.org/10.1097/01.ASN.0000064948.39199.A0.
(94) Nozu, K.; Iijima, K.; Kanda, K.; Nakanishi, K.; Yoshikawa, N.; Satomura, K.; Kaito, H.; Hashimura, Y.; Ninchoji, T.; Komatsu, H.; Kamei, K.; Miyashita, R.; Kugo, M.; Ohashi, H.; Yamazaki, H.; Mabe, H.; Otsubo, A.; Igarashi, T.; Matsuo, M. The Pharmacological Characteristics of Molecular-Based Inherited Salt-Losing Tubulopathies. *J. Clin. Endocrinol. Metab.* **2010**, *95* (12), E511–E518. https://doi.org/10.1210/jc.2010-0392.
(95) Colussi, G.; Bettinelli, A.; Tedeschi, S.; De Ferrari, M. E.; Syre[Combining Acute Accent]n, M. L.; Borsa, N. G. A.; Mattiello, C.; Casari, G.; Bianchetti, M. G. A Thiazide Test for the Diagnosis of Renal Tubular Hypokalemic Disorders. *Clin. J. Am. Soc. Nephrol.* **2007**, *2* (3), 454. https://doi.org/10.2215/CJN.02950906.
(96) Takahashi, N.; Chernavvsky, D. R.; Gomez, R. A.; Igarashi, P.; Gitelman, H. J.; Smithies, O. Uncompensated Polyuria in a Mouse Model of Bartter's Syndrome. *Proc. Natl. Acad. Sci.* **2000**, *97* (10), 5434–5439. https://doi.org/10.1073/pnas.090091297.

(97) Garneau, A. P.; Slimani, S.; Tremblay, L. E.; Fiola, M. J.; Marcoux, A. A.; Isenring, P. K+-Cl− Cotransporter 1 (KCC1): A Housekeeping Membrane Protein That Plays Key Supplemental Roles in Hematopoietic and Cancer Cells. *J. Hematol. Oncol.J Hematol Oncol* **2019**, *12* (1), 74. https://doi.org/10.1186/s13045-019-0766-x.

(98) Rust, M. B.; Faulhaber, J.; Budack, M. K.; Pfeffer, C.; Maritzen, T.; Didié, M.; Beck, F.-X.; Boettger, T.; Schubert, R.; Ehmke, H.; Jentsch, T. J.; Hübner, C. A. Neurogenic Mechanisms Contribute to Hypertension in Mice With Disruption of the K-Cl Cotransporter KCC3. *Circ. Res.* **2006**, *98* (4), 549–556. https://doi.org/10.1161/01.RES.0000204449.83861.22.

(99) Kahle, K. T.; Flores, B.; Bharucha-Goebel, D.; Zhang, J.; Donkervoort, S.; Hegde, M.; Begum, G.; Duran, D.; Liang, B.; Sun, D.; Bönnemann, C. G.; Delpire, E. Peripheral Motor Neuropathy Is Associated with Defective Kinase Regulation of the KCC3 Cotransporter. *Sci. Signal.* **2016**, *9* (439), ra77–ra77. https://doi.org/10.1126/scisignal.aae0546.

(100) Puskarjov, M.; Seja, P.; Heron, S. E.; Williams, T. C.; Ahmad, F.; Iona, X.; Oliver, K. L.; Grinton, B. E.; Vutskits, L.; Scheffer, I. E.; Petrou, S.; Blaesse, P.; Dibbens, L. M.; Berkovic, S. F.; Kaila, K. A Variant of KCC2 from Patients with Febrile Seizures Impairs Neuronal Cl− Extrusion and Dendritic Spine Formation. *EMBO Rep.* **2014**, *15* (6), 723–729. https://doi.org/10.1002/embr.201438749.

(101) Saito, T.; Ishii, A.; Sugai, K.; Sasaki, M.; Hirose, S. A de Novo Missense Mutation in SLC12A5 Found in a Compound Heterozygote Patient with Epilepsy of Infancy with Migrating Focal Seizures. *Clin. Genet.* **2017**, *92* (6), 654–658. https://doi.org/10.1111/cge.13049.

(102) Saitsu, H.; Watanabe, M.; Akita, T.; Ohba, C.; Sugai, K.; Ong, W. P.; Shiraishi, H.; Yuasa, S.; Matsumoto, H.; Beng, K. T.; Saitoh, S.; Miyatake, S.; Nakashima, M.; Miyake, N.; Kato, M.; Fukuda, A.; Matsumoto, N. Impaired Neuronal KCC2 Function by Biallelic SLC12A5 Mutations in Migrating Focal Seizures and Severe Developmental Delay. *Sci. Rep.* **2016**, *6* (1), 30072. https://doi.org/10.1038/srep30072.

(103) Till, Á.; Szalai, R.; Hegyi, M.; Kövesdi, E.; Büki, G.; Hadzsiev, K.; Melegh, B. Generalizált epilepszia hátterében azonosított ioncsatorna-génmutáció ritka formája. *Orv. Hetil.* **2019**, *160* (21), 835–838. https://doi.org/10.1556/650.2019.31404.

(104) Kahle, K. T.; Merner, N. D.; Friedel, P.; Silayeva, L.; Liang, B.; Khanna, A.; Shang, Y.; Lachance-Touchette, P.; Bourassa, C.; Levert, A.; Dion, P. A.; Walcott, B.; Spiegelman, D.; Dionne-Laporte, A.; Hodgkinson, A.; Awadalla, P.; Nikbakht, H.; Majewski, J.; Cossette, P.; Deeb, T. Z.; Moss, S. J.; Medina, I.; Rouleau, G. A. Genetically Encoded Impairment of Neuronal KCC2 Cotransporter Function in Human Idiopathic Generalized Epilepsy. *EMBO Rep.* **2014**, *15* (7), 766–774. https://doi.org/10.15252/embr.201438840.

(105) Merner, N. D.; Chandler, M. R.; Bourassa, C.; Liang, B.; Khanna, A. R.; Dion, P.; Rouleau, G. A.; Kahle, K. T. Regulatory Domain or CpG Site Variation in SLC12A5, Encoding the Chloride Transporter KCC2, in Human Autism and Schizophrenia. *Front. Cell. Neurosci.* **2015**, *9*.

(106) Hübner, C. A.; Stein, V.; Hermans-Borgmeyer, I.; Meyer, T.; Ballanyi, K.; Jentsch, T. J. Disruption of KCC2 Reveals an Essential Role of K-Cl Cotransport Already in Early Synaptic Inhibition. *Neuron* **2001**, *30* (2), 515–524. https://doi.org/10.1016/S0896-6273(01)00297-5.

(107) Woo, N.-S.; Lu, J.; England, R.; McClellan, R.; Dufour, S.; Mount, D. B.; Deutch, A. Y.; Lovinger, D. M.; Delpire, E. Hyperexcitability and Epilepsy Associated with Disruption of the Mouse Neuronal-Specific K–Cl Cotransporter Gene. *Hippocampus* **2002**, *12* (2), 258–268. https://doi.org/10.1002/hipo.10014.

(108) Blaesse, P.; Airaksinen, M. S.; Rivera, C.; Kaila, K. Cation-Chloride Cotransporters and Neuronal Function. *Neuron* **2009**, *61* (6), 820–838. https://doi.org/10.1016/j.neuron.2009.03.003.

(109) Moore, Y. E.; Conway, L. C.; Wobst, H. J.; Brandon, N. J.; Deeb, T. Z.; Moss, S. J. Developmental Regulation of KCC2 Phosphorylation Has Long-Term Impacts on Cognitive Function. *Front. Mol. Neurosci.* **2019**, *12*.

(110) Kelley, M. R.; Deeb, T. Z.; Brandon, N. J.; Dunlop, J.; Davies, P. A.; Moss, S. J. Compromising KCC2 Transporter Activity Enhances the Development of Continuous Seizure Activity. *Neuropharmacology* **2016**, *108*, 103–110. https://doi.org/10.1016/j.neuropharm.2016.04.029.
(111) Silayeva, L.; Deeb, T. Z.; Hines, R. M.; Kelley, M. R.; Munoz, M. B.; Lee, H. H. C.; Brandon, N. J.; Dunlop, J.; Maguire, J.; Davies, P. A.; Moss, S. J. KCC2 Activity Is Critical in Limiting the Onset and Severity of Status Epilepticus. *Proc. Natl. Acad. Sci.* **2015**, *112* (11), 3523–3528. https://doi.org/10.1073/pnas.1415126112.
(112) Pisella, L. I.; Gaiarsa, J.-L.; Diabira, D.; Zhang, J.; Khalilov, I.; Duan, J.; Kahle, K. T.; Medina, I. Impaired Regulation of KCC2 Phosphorylation Leads to Neuronal Network Dysfunction and Neurodevelopmental Pathology. *Sci. Signal.* **2019**, *12* (603), eaay0300. https://doi.org/10.1126/scisignal.aay0300.
(113) Dargaei, Z.; Bang, J. Y.; Mahadevan, V.; Khademullah, C. S.; Bedard, S.; Parfitt, G. M.; Kim, J. C.; Woodin, M. A. Restoring GABAergic Inhibition Rescues Memory Deficits in a Huntington's Disease Mouse Model. *Proc. Natl. Acad. Sci.* **2018**, *115* (7), E1618–E1626. https://doi.org/10.1073/pnas.1716871115.
(114) Flores, B.; Schornak, C. C.; Delpire, E. A Role for KCC3 in Maintaining Cell Volume of Peripheral Nerve Fibers. *Neurochem. Int.* **2019**, *123*, 114–124. https://doi.org/10.1016/j.neuint.2018.01.009.
(115) Lourenço, C. M.; Dupré, N.; Rivière, J.-B.; Rouleau, G. A.; Marques, V. D.; Genari, A. B.; Santos, A. C.; Barreira, A. A.; Marques Jr, W. Expanding the Differential Diagnosis of Inherited Neuropathies with Non-Uniform Conduction: Andermann Syndrome. *J. Peripher. Nerv. Syst.* **2012**, *17* (1), 123–127. https://doi.org/10.1111/j.1529-8027.2012.00374.x.
(116) Uyanik, G.; Elcioglu, N.; Penzien, J.; Gross, C.; Yilmaz, Y.; Olmez, A.; Demir, E.; Wahl, D.; Scheglmann, K.; Winner, B.; Bogdahn, U.; Topaloglu, H.; Hehr, U.; Winkler, J. Novel Truncating and Missense Mutations of the KCC3 Gene Associated with Andermann Syndrome. *Neurology* **2006**, *67* (8), 1528. https://doi.org/10.1212/01.wnl.0000250608.09509.ed.
(117) Howard, H. C.; Mount, D. B.; Rochefort, D.; Byun, N.; Dupré, N.; Lu, J.; Fan, X.; Song, L.; Rivière, J.-B.; Prévost, C.; Horst, J.; Simonati, A.; Lemcke, B.; Welch, R.; England, R.; Zhan, F. Q.; Mercado, A.; Siesser, W. B.; George, A. L.; McDonald, M. P.; Bouchard, J.-P.; Mathieu, J.; Delpire, E.; Rouleau, G. A. The K–Cl Cotransporter KCC3 Is Mutant in a Severe Peripheral Neuropathy Associated with Agenesis of the Corpus Callosum. *Nat. Genet.* **2002**, *32* (3), 384–392. https://doi.org/10.1038/ng1002.
(118) Jin, S. C.; Furey, C. G.; Zeng, X.; Allocco, A.; Nelson-Williams, C.; Dong, W.; Karimy, J. K.; Wang, K.; Ma, S.; Delpire, E.; Kahle, K. T. SLC12A Ion Transporter Mutations in Sporadic and Familial Human Congenital Hydrocephalus. *Mol. Genet. Genomic Med.* **2019**, *7* (9), e892. https://doi.org/10.1002/mgg3.892.
(119) Boettger, T.; Rust, M. B.; Maier, H.; Seidenbecher, T.; Schweizer, M.; Keating, D. J.; Faulhaber, J.; Ehmke, H.; Pfeffer, C.; Scheel, O.; Lemcke, B.; Horst, J.; Leuwer, R.; Pape, H.-C.; Völkl, H.; Hübner, C. A.; Jentsch, T. J. Loss of K-Cl Co-Transporter KCC3 Causes Deafness, Neurodegeneration and Reduced Seizure Threshold. *EMBO J.* **2003**, *22* (20), 5422–5434. https://doi.org/10.1093/emboj/cdg519.
(120) Lun, M. P.; Monuki, E. S.; Lehtinen, M. K. Development and Functions of the Choroid Plexus–Cerebrospinal Fluid System. *Nat. Rev. Neurosci.* **2015**, *16* (8), 445–457. https://doi.org/10.1038/nrn3921.
(121) Liddelow, S. A. Development of the Choroid Plexus and Blood-CSF Barrier. *Front. Neurosci.* **2015**, *9*.
(122) Zhan, C.; Xiao, G.; Zhang, X.; Chen, X.; Zhang, Z.; Liu, J. Decreased MiR-30a Promotes TGF-B1-Mediated Arachnoid Fibrosis in Post-Hemorrhagic Hydrocephalus. *Transl. Neurosci.* **2020**, *11* (1), 60–74. https://doi.org/10.1515/tnsci-2020-0010.

(123) Carmosino, M.; Valenti, G.; Caplan, M.; Svelto, M. Polarized Traffic towards the Cell Surface: How to Find the Route. *Biol. Cell* **2010**, *102* (2), 75–91. https://doi.org/10.1042/BC20090134.
(124) Bothwell, S. W.; Omileke, D.; Patabendige, A.; Spratt, N. J. CSF Secretion Is Not Altered by NKCC1 Nor TRPV4 Antagonism in Healthy Rats. *Brain Sci.* **2021**, *11* (9), 1117. https://doi.org/10.3390/brainsci11091117.
(125) Damkier, H. H.; Brown, P. D.; Praetorius, J. Cerebrospinal Fluid Secretion by the Choroid Plexus. *Physiol Rev* **2013**, *93*.
(126) Brinker, T.; Stopa, E.; Morrison, J.; Klinge, P. A New Look at Cerebrospinal Fluid Circulation. *Fluids Barriers CNS* **2014**, *11* (1), 10. https://doi.org/10.1186/2045-8118-11-10.
(127) Karimy, J. K.; Duran, D.; Hu, J. K.; Gavankar, C.; Gaillard, J. R.; Bayri, Y.; Rice, H.; DiLuna, M. L.; Gerzanich, V.; Marc Simard, J.; Kahle, K. T. Cerebrospinal Fluid Hypersecretion in Pediatric Hydrocephalus. *Neurosurg. Focus* **2016**, *41* (5), E10. https://doi.org/10.3171/2016.8.FOCUS16278.
(128) MacAulay, N.; Keep, R. F.; Zeuthen, T. Cerebrospinal Fluid Production by the Choroid Plexus: A Century of Barrier Research Revisited. *Fluids Barriers CNS* **2022**, *19* (1), 26. https://doi.org/10.1186/s12987-022-00323-1.
(129) Silverberg, G. D.; Mayo, M.; Saul, T.; Rubenstein, E.; McGuire, D. Alzheimer's Disease, Normal-pressure Hydrocephalus, and Senescent Changes in CSF Circulatory Physiology: A Hypothesis. *Lancet Neurol.* **2003**, *2* (8), 506–511. https://doi.org/10.1016/S1474-4422(03)00487-3.
(130) Karimy, J. K.; Zhang, J.; Kurland, D. B.; Theriault, B. C.; Duran, D.; Stokum, J. A.; Furey, C. G.; Zhou, X.; Mansuri, M. S.; Montejo, J.; Vera, A.; DiLuna, M. L.; Delpire, E.; Alper, S. L.; Gunel, M.; Gerzanich, V.; Medzhitov, R.; Simard, J. M.; Kahle, K. T. Inflammation-Dependent Cerebrospinal Fluid Hypersecretion by the Choroid Plexus Epithelium in Posthemorrhagic Hydrocephalus. *Nat. Med.* **2017**, *23* (8), 997–1003. https://doi.org/10.1038/nm.4361.
(131) Rayasam, A.; Faustino, J.; Lecuyer, M.; Vexler, Z. S. Neonatal Stroke and TLR1/2 Ligand Recruit Myeloid Cells through the Choroid Plexus in a CX3CR1-CCR2- and Context-Specific Manner. *J. Neurosci.* **2020**, *40* (19), 3849. https://doi.org/10.1523/JNEUROSCI.2149-19.2020.
(132) Vercellino, M.; Votta, B.; Condello, C.; Piacentino, C.; Romagnolo, A.; Merola, A.; Capello, E.; Mancardi, G. L.; Mutani, R.; Giordana, M. T.; Cavalla, P. Involvement of the Choroid Plexus in Multiple Sclerosis Autoimmune Inflammation: A Neuropathological Study. *J. Neuroimmunol.* **2008**, *199* (1), 133–141. https://doi.org/10.1016/j.jneuroim.2008.04.035.
(133) Kaur, C.; Rathnasamy, G.; Ling, E.-A. The Choroid Plexus in Healthy and Diseased Brain. *J. Neuropathol. Exp. Neurol.* **2016**, *75* (3), 198–213. https://doi.org/10.1093/jnen/nlv030.
(134) Llovera, G.; Benakis, C.; Enzmann, G.; Cai, R.; Arzberger, T.; Ghasemigharagoz, A.; Mao, X.; Malik, R.; Lazarevic, I.; Liebscher, S.; Ertürk, A.; Meissner, L.; Vivien, D.; Haffner, C.; Plesnila, N.; Montaner, J.; Engelhardt, B.; Liesz, A. The Choroid Plexus Is a Key Cerebral Invasion Route for T Cells after Stroke. *Acta Neuropathol. (Berl.)* **2017**, *134* (6), 851–868. https://doi.org/10.1007/s00401-017-1758-y.
(135) Bothwell, S. W.; Janigro, D.; Patabendige, A. Cerebrospinal Fluid Dynamics and Intracranial Pressure Elevation in Neurological Diseases. *Fluids Barriers CNS* **2019**, *16* (1), 9. https://doi.org/10.1186/s12987-019-0129-6.
(136) Liu, H.; Hua, Y.; Keep, R. F.; Xi, G. Brain Ceruloplasmin Expression After Experimental Intracerebral Hemorrhage and Protection Against Iron-Induced Brain Injury. *Transl. Stroke Res.* **2019**, *10* (1), 112–119. https://doi.org/10.1007/s12975-018-0669-0.
(137) Kahle, K. T.; Kulkarni, A. V.; Limbrick, D. D.; Warf, B. C. Hydrocephalus in Children. *The Lancet* **2016**, *387* (10020), 788–799. https://doi.org/10.1016/S0140-6736(15)60694-8.
(138) McAllister, J. P.; Williams, M. A.; Walker, M. L.; Kestle, J. R. W.; Relkin, N. R.; Anderson, A. M.; Gross, P. H.; Browd, S. R. An Update on Research Priorities in Hydrocephalus: Overview of the

Third National Institutes of Health-Sponsored Symposium “Opportunities for Hydrocephalus Research: Pathways to Better Outcomes.” *J. Neurosurg.* **2015**, *123* (6), 1427–1438. https://doi.org/10.3171/2014.12.JNS132352.

(139) Yang, Y.; He, J.; Wang, Y.; Wang, C.; Tan, C.; Liao, J.; Tong, L.; Xiao, G. Targeting Choroid Plexus Epithelium as a Novel Therapeutic Strategy for Hydrocephalus. *J. Neuroinflammation* **2022**, *19* (1), 156. https://doi.org/10.1186/s12974-022-02500-3.

(140) Gregoriades, J. M. C.; Madaris, A.; Alvarez, F. J.; Alvarez-Leefmans, F. J. Genetic and Pharmacological Inactivation of Apical Na+-K+-2Cl− Cotransporter 1 in Choroid Plexus Epithelial Cells Reveals the Physiological Function of the Cotransporter. *Am. J. Physiol. - Cell Physiol.* **2019**, *316* (4), C525–C544. https://doi.org/10.1152/ajpcell.00026.2018.

(141) Bairamian, D.; Johanson, C. E.; Parmelee, J. T.; Epstein, M. H. Potassium Cotransport with Sodium and Chloride in the Choroid Plexus. *J. Neurochem.* **1991**, *56* (5), 1623–1629. https://doi.org/10.1111/j.1471-4159.1991.tb02060.x.

(142) O’Donnell, M. E.; Tran, L.; Lam, T. I.; Liu, X. B.; Anderson, S. E. Bumetanide Inhibition of the Blood-Brain Barrier Na-K-Cl Cotransporter Reduces Edema Formation in the Rat Middle Cerebral Artery Occlusion Model of Stroke. *J. Cereb. Blood Flow Metab.* **2004**, *24* (9), 1046–1056. https://doi.org/10.1097/01.WCB.0000130867.32663.90.

(143) Begum, G.; Yuan, H.; Kahle, K. T.; Li, L.; Wang, S.; Shi, Y.; Shmukler, B. E.; Yang, S.-S.; Lin, S.-H.; Alper, S. L.; Sun, D. Inhibition of WNK3 Kinase Signaling Reduces Brain Damage and Accelerates Neurological Recovery After Stroke. *Stroke* **2015**, *46* (7), 1956–1965. https://doi.org/10.1161/STROKEAHA.115.008939.

(144) Wang, J.; Liu, R.; Hasan, M. N.; Fischer, S.; Chen, Y.; Como, M.; Fiesler, V. M.; Bhuiyan, M. I. H.; Dong, S.; Li, E.; Kahle, K. T.; Zhang, J.; Deng, X.; Subramanya, A. R.; Begum, G.; Yin, Y.; Sun, D. Role of SPAK–NKCC1 Signaling Cascade in the Choroid Plexus Blood–CSF Barrier Damage after Stroke. *J. Neuroinflammation* **2022**, *19* (1), 91. https://doi.org/10.1186/s12974-022-02456-4.

(145) Zhang, J.; Pu, H.; Zhang, H.; Wei, Z.; Jiang, X.; Xu, M.; Zhang, L.; Zhang, W.; Liu, J.; Meng, H.; Stetler, R. A.; Sun, D.; Chen, J.; Gao, Y.; Chen, L. Inhibition of Na+-K+-2Cl− Cotransporter Attenuates Blood-Brain-Barrier Disruption in a Mouse Model of Traumatic Brain Injury. *Neurochem. Int.* **2017**, *111*, 23–31. https://doi.org/10.1016/j.neuint.2017.05.020.

(146) Zhang, Z.; Tan, Q.; Guo, P.; Huang, S.; Jia, Z.; Liu, X.; Feng, H.; Chen, Y. NLRP3 Inflammasome-Mediated Choroid Plexus Hypersecretion Contributes to Hydrocephalus after Intraventricular Hemorrhage via Phosphorylated NKCC1 Channels. *J. Neuroinflammation* **2022**, *19* (1), 163. https://doi.org/10.1186/s12974-022-02530-x.

(147) Zhou, Y.; Sun, W.; Chen, N.; Xu, C.; Wang, X.; Dong, K.; Zhang, B.; Zhang, J.; Hao, N.; Sun, A.; Wei, H.; He, F.; Jiang, Y. Discovery of NKCC1 as a Potential Therapeutic Target to Inhibit Hepatocellular Carcinoma Cell Growth and Metastasis. *Oncotarget* **2017**, *8* (39), 66328–66342. https://doi.org/10.18632/oncotarget.20240.

(148) Kharod, S. C.; Kang, S. K.; Kadam, S. D. Off-Label Use of Bumetanide for Brain Disorders: An Overview. *Front. Neurosci.* **2019**, *13*, 310. https://doi.org/10.3389/fnins.2019.00310.

(149) Lemonnier, E.; Degrez, C.; Phelep, M.; Tyzio, R.; Josse, F.; Grandgeorge, M.; Hadjikhani, N.; Ben-Ari, Y. A Randomised Controlled Trial of Bumetanide in the Treatment of Autism in Children. *Transl. Psychiatry* **2012**, *2* (12), e202–e202. https://doi.org/10.1038/tp.2012.124.

(150) Savardi, A.; Borgogno, M.; Narducci, R.; La Sala, G.; Ortega, J. A.; Summa, M.; Armirotti, A.; Bertorelli, R.; Contestabile, A.; De Vivo, M.; Cancedda, L. Discovery of a Small Molecule Drug Candidate for Selective NKCC1 Inhibition in Brain Disorders. *Chem* **2020**, *6* (8), 2073–2096. https://doi.org/10.1016/j.chempr.2020.06.017.

(151) Superti-Furga, G.; Lackner, D.; Wiedmer, T.; Ingles-Prieto, A.; Barbosa, B.; Girardi, E.; Goldmann, U.; Gürtl, B.; Klavins, K.; Klimek, C.; Lindinger, S.; Liñeiro-Retes, E.; Müller, A. C.; Onstein, S.;

Redinger, G.; Reil, D.; Sedlyarov, V.; Wolf, G.; Crawford, M.; Everley, R.; Hepworth, D.; Liu, S.; Noell, S.; Piotrowski, M.; Stanton, R.; Zhang, H.; Corallino, S.; Faedo, A.; Insidioso, M.; Maresca, G.; Redaelli, L.; Sassone, F.; Scarabottolo, L.; Stucchi, M.; Tarroni, P.; Tremolada, S.; Batoulis, H.; Becker, A.; Bender, E.; Chang, Y.-N.; Ehrmann, A.; Müller-Fahrnow, A.; Pütter, V.; Zindel, D.; Hamilton, B.; Lenter, M.; Santacruz, D.; Viollet, C.; Whitehurst, C.; Johnsson, K.; Leippe, P.; Baumgarten, B.; Chang, L.; Ibig, Y.; Pfeifer, M.; Reinhardt, J.; Schönbett, J.; Selzer, P.; Seuwen, K.; Bettembourg, C.; Biton, B.; Czech, J.; de Foucauld, H.; Didier, M.; Licher, T.; Mikol, V.; Pommereau, A.; Puech, F.; Yaligara, V.; Edwards, A.; Bongers, B. J.; Heitman, L. H.; IJzerman, A. P.; Sijben, H. J.; van Westen, G. J. P.; Grixti, J.; Kell, D. B.; Mughal, F.; Swainston, N.; Wright-Muelas, M.; Bohstedt, T.; Burgess-Brown, N.; Carpenter, L.; Dürr, K.; Hansen, J.; Scacioc, A.; Banci, G.; Colas, C.; Digles, D.; Ecker, G.; Füzi, B.; Gamsjäger, V.; Grandits, M.; Martini, R.; Troger, F.; Altermatt, P.; Doucerain, C.; Dürrenberger, F.; Manolova, V.; Steck, A.-L.; Sundström, H.; Wilhelm, M.; Steppan, C. M. The RESOLUTE Consortium: Unlocking SLC Transporters for Drug Discovery. *Nat. Rev. Drug Discov.* **2020**, *19* (7), 429–430. https://doi.org/10.1038/d41573-020-00056-6.

(152) Czuba, L. C.; Hillgren, K. M.; Swaan, P. W. Post-Translational Modifications of Transporters. *Pharmacol. Ther.* **2018**, *192*, 88–99. https://doi.org/10.1016/j.pharmthera.2018.06.013.

(153) Bensimon, A.; Pizzagalli, M. D.; Kartnig, F.; Dvorak, V.; Essletzbichler, P.; Winter, G. E.; Superti-Furga, G. Targeted Degradation of SLC Transporters Reveals Amenability of Multi-Pass Transmembrane Proteins to Ligand-Induced Proteolysis. *Cell Chem. Biol.* **2020**, *27* (6), 728-739.e9. https://doi.org/10.1016/j.chembiol.2020.04.003.

(154) Hanna, J.; Guerra-Moreno, A.; Ang, J.; Micoogullari, Y. Protein Degradation and the Pathologic Basis of Disease. *Am. J. Pathol.* **2019**, *189* (1), 94–103. https://doi.org/10.1016/j.ajpath.2018.09.004.

(155) Savardi, A.; Borgogno, M.; De Vivo, M.; Cancedda, L. Pharmacological Tools to Target NKCC1 in Brain Disorders. *Trends Pharmacol. Sci.* **2021**, *42* (12), 1009–1034. https://doi.org/10.1016/j.tips.2021.09.005.

(156) Karplus, M.; McCammon, J. A. Molecular Dynamics Simulations of Biomolecules. *Nat. Struct. Biol.* **2002**, *9* (9), 646–652. https://doi.org/10.1038/nsb0902-646.

(157) Hollingsworth, S. A.; Dror, R. O. Molecular Dynamics Simulation for All. *Neuron* **2018**, *99* (6), 1129–1143. https://doi.org/10.1016/j.neuron.2018.08.011.

(158) Alder, B. J.; Wainwright, T. E. Phase Transition for a Hard Sphere System. *J. Chem. Phys.* **1957**, *27* (5), 1208–1209. https://doi.org/10.1063/1.1743957.

(159) McCammon, J. A.; Gelin, B. R.; Karplus, M. Dynamics of Folded Proteins. *Nature* **1977**, *267* (5612), 585–590. https://doi.org/10.1038/267585a0.

(160) Abraham, M.; Alekseenko, A.; Bergh, C.; Blau, C.; Briand, E.; Doijade, M.; Fleischmann, S.; Gapsys, V.; Garg, G.; Gorelov, S.; Gouaillardet, G.; Gray, A.; Irrgang, M. E.; Jalalypour, F.; Jordan, J.; Junghans, C.; Kanduri, P.; Keller, S.; Kutzner, C.; Lemkul, J. A.; Lundborg, M.; Merz, P.; Miletić, V.; Morozov, D.; Páll, S.; Schulz, R.; Shirts, M.; Shvetsov, A.; Soproni, B.; Spoel, D. van der; Turner, P.; Uphoff, C.; Villa, A.; Wingbermühle, S.; Zhmurov, A.; Bauer, P.; Hess, B.; Lindahl, E. GROMACS 2023.2 Manual. **2023**. https://doi.org/10.5281/zenodo.8134388.

(161) Jumper, J.; Evans, R.; Pritzel, A.; Green, T.; Figurnov, M.; Ronneberger, O.; Tunyasuvunakool, K.; Bates, R.; Žídek, A.; Potapenko, A.; Bridgland, A.; Meyer, C.; Kohl, S. A. A.; Ballard, A. J.; Cowie, A.; Romera-Paredes, B.; Nikolov, S.; Jain, R.; Adler, J.; Back, T.; Petersen, S.; Reiman, D.; Clancy, E.; Zielinski, M.; Steinegger, M.; Pacholska, M.; Berghammer, T.; Bodenstein, S.; Silver, D.; Vinyals, O.; Senior, A. W.; Kavukcuoglu, K.; Kohli, P.; Hassabis, D. Highly Accurate Protein Structure Prediction with AlphaFold. *Nature* **2021**, *596* (7873), 583–589. https://doi.org/10.1038/s41586-021-03819-2.

(162) Webb, B.; Sali, A. Comparative Protein Structure Modeling Using MODELLER. *Curr. Protoc. Bioinforma.* **2016**, *54* (1), 5.6.1-5.6.37. https://doi.org/10.1002/cpbi.3.
(163) Frenkel, D.; Smit, B. *Understanding Molecular Simulation: From Algorithms to Applications*, 2nd ed.; Computational science (San Diego, Calif.); Academic Press: San Diego, 2002.
(164) Cornell, W. D.; Cieplak, P.; Bayly, C. I.; Gould, I. R.; Merz, K. M.; Ferguson, D. M.; Spellmeyer, D. C.; Fox, T.; Caldwell, J. W.; Kollman, P. A. A Second Generation Force Field for the Simulation of Proteins, Nucleic Acids, and Organic Molecules. *J. Am. Chem. Soc.* **1995**, *117* (19), 5179–5197. https://doi.org/10.1021/ja00124a002.
(165) Leach, A. R. *Molecular Modelling: Principles and Applications*; Pearson Education, 2001.
(166) Slater, J. C. A Simplification of the Hartree-Fock Method. *Phys. Rev.* **1951**, *81* (3), 385–390. https://doi.org/10.1103/PhysRev.81.385.
(167) Burke, K. Perspective on Density Functional Theory. *J. Chem. Phys.* **2012**, *136* (15), 150901. https://doi.org/10.1063/1.4704546.
(168) Mulliken, R. S. Electronic Population Analysis on LCAO–MO Molecular Wave Functions. I. *J. Chem. Phys.* **1955**, *23* (10), 1833–1840. https://doi.org/10.1063/1.1740588.
(169) Wang, J.; Cieplak, P.; Kollman, P. A. How well does a restrained electrostatic potential (RESP) model perform in calculating conformational energies of organic and biological molecules? *J. Comput. Chem.* **2000**, *21* (12), 1049–1074. https://doi.org/10.1002/1096-987X(200009)21:12<1049::AID-JCC3>3.0.CO;2-F.
(170) Ryckaert, J.-P.; Ciccotti, G.; Berendsen, H. J. C. Numerical Integration of the Cartesian Equations of Motion of a System with Constraints: Molecular Dynamics of n-Alkanes. *J. Comput. Phys.* **1977**, *23* (3), 327–341. https://doi.org/10.1016/0021-9991(77)90098-5.
(171) Berendsen, H. J. C.; Postma, J. P. M.; Van Gunsteren, W. F.; DiNola, A.; Haak, J. R. Molecular Dynamics with Coupling to an External Bath. *J. Chem. Phys.* **1984**, *81* (8), 3684–3690. https://doi.org/10.1063/1.448118.
(172) Nosé, S. A Unified Formulation of the Constant Temperature Molecular Dynamics Methods. *J. Chem. Phys.* **1984**, *81* (1), 511–519. https://doi.org/10.1063/1.447334.
(173) Hoover, W. G. Canonical Dynamics: Equilibrium Phase-Space Distributions. *Phys. Rev. A* **1985**, *31* (3), 1695–1697. https://doi.org/10.1103/PhysRevA.31.1695.
(174) Andersen, H. C. Molecular Dynamics Simulations at Constant Pressure and/or Temperature. *J. Chem. Phys.* **1980**, *72* (4), 2384–2393. https://doi.org/10.1063/1.439486.
(175) Parrinello, M.; Rahman, A. Polymorphic Transitions in Single Crystals: A New Molecular Dynamics Method. *J. Appl. Phys.* **1981**, *52* (12), 7182–7190. https://doi.org/10.1063/1.328693.
(176) Kollman, P. A.; Massova, I.; Reyes, C.; Kuhn, B.; Huo, S.; Chong, L.; Lee, M.; Lee, T.; Duan, Y.; Wang, W.; Donini, O.; Cieplak, P.; Srinivasan, J.; Case, D. A.; Cheatham, T. E. Calculating Structures and Free Energies of Complex Molecules: Combining Molecular Mechanics and Continuum Models. *Acc. Chem. Res.* **2000**, *33* (12), 889–897. https://doi.org/10.1021/ar000033j.
(177) Saint-Martin, H.; Hess, B.; Berendsen, H. J. C. An Application of Flexible Constraints in Monte Carlo Simulations of the Isobaric–Isothermal Ensemble of Liquid Water and Ice Ih with the Polarizable and Flexible Mobile Charge Densities in Harmonic Oscillators Model. *J. Chem. Phys.* **2004**, *120* (23), 11133–11143. https://doi.org/10.1063/1.1747927.
(178) Berendsen, H. J. C.; Postma, J. P. M.; van Gunsteren, W. F.; Hermans, J. Interaction Models for Water in Relation to Protein Hydration. In *Intermolecular Forces: Proceedings of the Fourteenth Jerusalem Symposium on Quantum Chemistry and Biochemistry Held in Jerusalem, Israel, April 13–16, 1981*; Pullman, B., Ed.; The Jerusalem Symposia on Quantum Chemistry and Biochemistry; Springer Netherlands: Dordrecht, 1981; pp 331–342. https://doi.org/10.1007/978-94-015-7658-1_21.

(179) Jorgensen, W. L.; Chandrasekhar, J.; Madura, J. D.; Impey, R. W.; Klein, M. L. Comparison of Simple Potential Functions for Simulating Liquid Water. *J. Chem. Phys.* **1983**, *79* (2), 926–935. https://doi.org/10.1063/1.445869.
(180) Mahoney, M. W.; Jorgensen, W. L. A Five-Site Model for Liquid Water and the Reproduction of the Density Anomaly by Rigid, Nonpolarizable Potential Functions. *J. Chem. Phys.* **2000**, *112* (20), 8910–8922. https://doi.org/10.1063/1.481505.
(181) Ahmad, M.; Gu, W.; Geyer, T.; Helms, V. Adhesive Water Networks Facilitate Binding of Protein Interfaces. *Nat. Commun.* **2011**, *2* (1), 261. https://doi.org/10.1038/ncomms1258.
(182) Rudling, A.; Orro, A.; Carlsson, J. Prediction of Ordered Water Molecules in Protein Binding Sites from Molecular Dynamics Simulations: The Impact of Ligand Binding on Hydration Networks. *J. Chem. Inf. Model.* **2018**, *58* (2), 350–361. https://doi.org/10.1021/acs.jcim.7b00520.
(183) Donati, E.; Genna, V.; De Vivo, M. Recruiting Mechanism and Functional Role of a Third Metal Ion in the Enzymatic Activity of 5′ Structure-Specific Nucleases. *J. Am. Chem. Soc.* **2020**, *142* (6), 2823–2834. https://doi.org/10.1021/jacs.9b10656.
(184) Bedrov, D.; Piquemal, J.-P.; Borodin, O.; MacKerell, A. D. Jr.; Roux, B.; Schröder, C. Molecular Dynamics Simulations of Ionic Liquids and Electrolytes Using Polarizable Force Fields. *Chem. Rev.* **2019**, *119* (13), 7940–7995. https://doi.org/10.1021/acs.chemrev.8b00763.
(185) Riniker, S. Fixed-Charge Atomistic Force Fields for Molecular Dynamics Simulations in the Condensed Phase: An Overview. *J. Chem. Inf. Model.* **2018**, *58* (3), 565–578. https://doi.org/10.1021/acs.jcim.8b00042.
(186) Lemkul, J. A.; Huang, J.; Roux, B.; MacKerell, A. D. Jr. An Empirical Polarizable Force Field Based on the Classical Drude Oscillator Model: Development History and Recent Applications. *Chem. Rev.* **2016**, *116* (9), 4983–5013. https://doi.org/10.1021/acs.chemrev.5b00505.
(187) Frank, H. S.; Wen, W.-Y. Ion-Solvent Interaction. Structural Aspects of Ion-Solvent Interaction in Aqueous Solutions: A Suggested Picture of Water Structure. *Discuss. Faraday Soc.* **1957**, *24* (0), 133–140. https://doi.org/10.1039/DF9572400133.
(188) Śmiechowski, M. Anion–Water Interactions of Weakly Hydrated Anions: Molecular Dynamics Simulations of Aqueous NaBF4 and NaPF6. *Mol. Phys.* **2016**, *114* (12), 1831–1846. https://doi.org/10.1080/00268976.2016.1157219.
(189) Lecce, S. D.; Albrecht, T.; Bresme, F. The Role of Ion–Water Interactions in Determining the Soret Coefficient of LiCl Aqueous Solutions. *Phys. Chem. Chem. Phys.* **2017**, *19* (14), 9575–9583. https://doi.org/10.1039/C7CP01241A.
(190) Schwidetzky, R.; Lukas, M.; YazdanYar, A.; Kunert, A. T.; Pöschl, U.; Domke, K. F.; Fröhlich-Nowoisky, J.; Bonn, M.; Koop, T.; Nagata, Y.; Meister, K. Specific Ion–Protein Interactions Influence Bacterial Ice Nucleation. *Chem. – Eur. J.* **2021**, *27* (26), 7402–7407. https://doi.org/10.1002/chem.202004630.
(191) Matsarskaia, O.; Roosen-Runge, F.; Schreiber, F. Multivalent Ions and Biomolecules: Attempting a Comprehensive Perspective. *ChemPhysChem* **2020**, *21* (16), 1742–1767. https://doi.org/10.1002/cphc.202000162.
(192) Yu, H.; Noskov, S. Yu.; Roux, B. Two Mechanisms of Ion Selectivity in Protein Binding Sites. *Proc. Natl. Acad. Sci.* **2010**, *107* (47), 20329–20334. https://doi.org/10.1073/pnas.1007150107.
(193) Giudici, A. M.; Renart, M. L.; Coutinho, A.; Morales, A.; González-Ros, J. M.; Poveda, J. A. Molecular Events behind the Selectivity and Inactivation Properties of Model NaK-Derived Ion Channels. *Int. J. Mol. Sci.* **2022**, *23* (16), 9246. https://doi.org/10.3390/ijms23169246.
(194) Bučević-Popović, V.; Pavela-Vrančič, M.; Dieckmann, R. Metal-Ion Induced Conformational Changes in Alkaline Phosphatase from E. Coli Assessed by Limited Proteolysis. *Biochimie* **2004**, *86* (6), 403–409. https://doi.org/10.1016/j.biochi.2004.05.001.

(195) Ramis, R.; Ballesteros, Ó. R.; Muguruza-Montero, A.; M-Alicante, S.; Núñez, E.; Villarroel, Á.; Leonardo, A.; Bergara, A. Molecular Dynamics Simulations of the Calmodulin-Induced α-Helix in the SK2 Calcium-Gated Potassium Ion Channel. *J. Biol. Chem.* **2023**, *299* (2), 102850. https://doi.org/10.1016/j.jbc.2022.102850.
(196) Sun, Y.; Song, L. Accurate Determination of Electrical Potential on Ion Exchange Membranes in Reverse Electrodialysis. *Separations* **2021**, *8* (10), 170. https://doi.org/10.3390/separations8100170.
(197) Kawaguchi, K.; Ito, S.; Saito, H.; Nagao, H. Molecular Dynamics Study of Lipid Bilayer Asymmetry Induced by Ion Concentration Gradient and Electronic Polarizability. *Mol. Simul.* **2022**, *48* (6), 477–483. https://doi.org/10.1080/08927022.2022.2025798.
(198) Ludewig, U.; Frommer, W. B. Genes and Proteins for Solute Transport and Sensing. *Arab. Book* **2002**, *2002* (1). https://doi.org/10.1199/tab.0092.
(199) Simons, K.; Ehehalt, R. Cholesterol, Lipid Rafts, and Disease. *J. Clin. Invest.* **2002**, *110* (5), 597–603. https://doi.org/10.1172/JCI16390.
(200) *Coarse-Graining of Condensed Phase and Biomolecular Systems*; Voth, G. A., Ed.; CRC Press: Boca Raton, 2008. https://doi.org/10.1201/9781420059564.
(201) Enkavi, G.; Javanainen, M.; Kulig, W.; Róg, T.; Vattulainen, I. Multiscale Simulations of Biological Membranes: The Challenge To Understand Biological Phenomena in a Living Substance. *Chem. Rev.* **2019**, *119* (9), 5607–5774. https://doi.org/10.1021/acs.chemrev.8b00538.
(202) Skjevik, Å. A.; Madej, B. D.; Walker, R. C.; Teigen, K. LIPID11: A Modular Framework for Lipid Simulations Using Amber. *J. Phys. Chem. B* **2012**, *116* (36), 11124–11136. https://doi.org/10.1021/jp3059992.
(203) Dickson, C. J.; Walker, R. C.; Gould, I. R. Lipid21: Complex Lipid Membrane Simulations with AMBER. *J. Chem. Theory Comput.* **2022**, *18* (3), 1726–1736. https://doi.org/10.1021/acs.jctc.1c01217.
(204) Chakraborty, S.; Doktorova, M.; Molugu, T. R.; Heberle, F. A.; Scott, H. L.; Dzikovski, B.; Nagao, M.; Stingaciu, L.-R.; Standaert, R. F.; Barrera, F. N.; Katsaras, J.; Khelashvili, G.; Brown, M. F.; Ashkar, R. How Cholesterol Stiffens Unsaturated Lipid Membranes. *Proc. Natl. Acad. Sci.* **2020**, *117* (36), 21896–21905. https://doi.org/10.1073/pnas.2004807117.
(205) Straub, J. E.; Thirumalai, D. Membrane–Protein Interactions Are Key to Understanding Amyloid Formation. *J. Phys. Chem. Lett.* **2014**, *5* (3), 633–635. https://doi.org/10.1021/jz500054d.
(206) Weigle, A. T.; Carr, M.; Shukla, D. Impact of Increased Membrane Realism on Conformational Sampling of Proteins. *J. Chem. Theory Comput.* **2021**, *17* (8), 5342–5357. https://doi.org/10.1021/acs.jctc.1c00276.
(207) Abrams, C.; Bussi, G. Enhanced Sampling in Molecular Dynamics Using Metadynamics, Replica-Exchange, and Temperature-Acceleration. *Entropy* **2014**, *16* (1), 163–199. https://doi.org/10.3390/e16010163.
(208) De Vivo, M.; Masetti, M.; Bottegoni, G.; Cavalli, A. Role of Molecular Dynamics and Related Methods in Drug Discovery. *J. Med. Chem.* **2016**, *59* (9), 4035–4061. https://doi.org/10.1021/acs.jmedchem.5b01684.
(209) Isralewitz, B.; Gao, M.; Schulten, K. Steered Molecular Dynamics and Mechanical Functions of Proteins. *Curr. Opin. Struct. Biol.* **2001**, *11* (2), 224–230. https://doi.org/10.1016/S0959-440X(00)00194-9.
(210) Yu, T.-Q.; Lu, J.; Abrams, C. F.; Vanden-Eijnden, E. Multiscale Implementation of Infinite-Swap Replica Exchange Molecular Dynamics. *Proc. Natl. Acad. Sci.* **2016**, *113* (42), 11744–11749. https://doi.org/10.1073/pnas.1605089113.
(211) Sugita, Y.; Okamoto, Y. Replica-Exchange Molecular Dynamics Method for Protein Folding. *Chem. Phys. Lett.* **1999**, *314* (1–2), 141–151. https://doi.org/10.1016/S0009-2614(99)01123-9.

(212) Laio, A.; Parrinello, M. Escaping Free-Energy Minima. *Proc. Natl. Acad. Sci.* **2002**, *99* (20), 12562–12566. https://doi.org/10.1073/pnas.202427399.
(213) Invernizzi, M.; Parrinello, M. Rethinking Metadynamics: From Bias Potentials to Probability Distributions. *J. Phys. Chem. Lett.* **2020**, *11* (7), 2731–2736. https://doi.org/10.1021/acs.jpclett.0c00497.
(214) Ensing, B.; De Vivo, M.; Liu, Z.; Moore, P.; Klein, M. L. Metadynamics as a Tool for Exploring Free Energy Landscapes of Chemical Reactions. *Acc. Chem. Res.* **2006**, *39* (2), 73–81. https://doi.org/10.1021/ar040198i.
(215) Invernizzi, M.; Piaggi, P. M.; Parrinello, M. Unified Approach to Enhanced Sampling. *Phys. Rev. X* **2020**, *10* (4), 041034. https://doi.org/10.1103/PhysRevX.10.041034.
(216) Invernizzi, M.; Parrinello, M. Exploration vs Convergence Speed in Adaptive-Bias Enhanced Sampling. *J. Chem. Theory Comput.* **2022**, *18* (6), 3988–3996. https://doi.org/10.1021/acs.jctc.2c00152.
(217) Markadieu, N.; Delpire, E. Physiology and Pathophysiology of SLC12A1/2 Transporters. *Pflugers Arch.* **2014**, *466* (1), 10.1007/s00424-013-1370–1375. https://doi.org/10.1007/s00424-013-1370-5.
(218) Gagnon, K. B.; Delpire, E. Physiology of SLC12 Transporters: Lessons from Inherited Human Genetic Mutations and Genetically Engineered Mouse Knockouts. *Am. J. Physiol. - Cell Physiol.* **2013**, *304* (8), C693–C714. https://doi.org/10.1152/ajpcell.00350.2012.
(219) Kahle, K. T.; Staley, K. J.; Nahed, B. V.; Gamba, G.; Hebert, S. C.; Lifton, R. P.; Mount, D. B. Roles of the Cation-Chloride Cotransporters in Neurological Disease. *Nat. Clin. Pract. Neurol.* **2008**, *4* (9), 490–503. https://doi.org/10.1038/ncpneuro0883.
(220) Kahle, K. T.; Khanna, A. R.; Alper, S. L.; Adragna, N. C.; Lauf, P. K.; Sun, D.; Delpire, E. K-Cl Cotransporters, Cell Volume Homeostasis, and Neurological Disease. *Trends Mol. Med.* **2015**, *21* (8), 513–523. https://doi.org/10.1016/j.molmed.2015.05.008.
(221) Russell, J. M. Sodium-Potassium-Chloride Cotransport. *Physiol. Rev.* **2000**, *80* (1), 211–276. https://doi.org/10.1152/physrev.2000.80.1.211.
(222) Lauf, P. K.; Adragna, N. C. K-Cl Cotransport: Properties and Molecular Mechanism. *Cell. Physiol. Biochem. Int. J. Exp. Cell. Physiol. Biochem. Pharmacol.* **2000**, *10* (5–6), 341–354. https://doi.org/10.1159/000016357.
(223) Lauf, P. K.; Bauer, J.; Adragna, N. C.; Fujise, H.; Zade-Oppen, A. M.; Ryu, K. H.; Delpire, E. Erythrocyte K-Cl Cotransport: Properties and Regulation. *Am. J. Physiol.-Cell Physiol.* **1992**, *263* (5), C917–C932. https://doi.org/10.1152/ajpcell.1992.263.5.C917.
(224) Glykys, J.; Dzhala, V.; Egawa, K.; Kahle, K. T.; Delpire, E.; Staley, K. Chloride Dysregulation, Seizures, and Cerebral Edema: A Relationship with Therapeutic Potential. *Trends Neurosci.* **2017**, *40* (5), 276–294. https://doi.org/10.1016/j.tins.2017.03.006.
(225) Park, J.; Flores, B. R.; Scherer, K.; Kuepper, H.; Rossi, M.; Rupprich, K.; Rautenberg, M.; Deininger, N.; Weichselbaum, A.; Grimm, A.; Sturm, M.; Grasshoff, U.; Delpire, E.; Haack, T. B. *De Novo* Variants in *SLC12A6* Cause Sporadic Early-Onset Progressive Sensorimotor Neuropathy. *J. Med. Genet.* **2020**, *57* (4), 283–288. https://doi.org/10.1136/jmedgenet-2019-106273.
(226) Löscher, W.; Puskarjov, M.; Kaila, K. Cation-Chloride Cotransporters NKCC1 and KCC2 as Potential Targets for Novel Antiepileptic and Antiepileptogenic Treatments. *Neuropharmacology* **2013**, *69*, 62–74. https://doi.org/10.1016/j.neuropharm.2012.05.045.
(227) Delpire, E.; Kahle, K. T. The KCC3 Cotransporter as a Therapeutic Target for Peripheral Neuropathy. *Expert Opin. Ther. Targets* **2017**, *21* (2), 113–116. https://doi.org/10.1080/14728222.2017.1275569.
(228) Duy, P. Q.; David, W. B.; Kahle, K. T. Identification of KCC2 Mutations in Human Epilepsy Suggests Strategies for Therapeutic Transporter Modulation. *Front. Cell. Neurosci.* **2019**, *13*.

(229) Gagnon, M.; Bergeron, M. J.; Lavertu, G.; Castonguay, A.; Tripathy, S.; Bonin, R. P.; Perez-Sanchez, J.; Boudreau, D.; Wang, B.; Dumas, L.; Valade, I.; Bachand, K.; Jacob-Wagner, M.; Tardif, C.; Kianicka, I.; Isenring, P.; Attardo, G.; Coull, J. A. M.; De Koninck, Y. Chloride Extrusion Enhancers as Novel Therapeutics for Neurological Diseases. *Nat. Med.* **2013**, *19* (11), 1524–1528. https://doi.org/10.1038/nm.3356.

(230) Chen, B.; Li, Y.; Yu, B.; Zhang, Z.; Brommer, B.; Williams, P. R.; Liu, Y.; Hegarty, S. V.; Zhou, S.; Zhu, J.; Guo, H.; Lu, Y.; Gu, X.; He, Z. Reactivation of Dormant Relay Pathways in Injured Spinal Cord by KCC2 Manipulations. *Cell* **2018**, *174* (3), 521-535.e13. https://doi.org/10.1016/j.cell.2018.06.005.

(231) Brown, F. C.; Conway, A. J.; Cerruti, L.; Collinge, J. E.; McLean, C.; Wiley, J. S.; Kile, B. T.; Jane, S. M.; Curtis, D. J. Activation of the Erythroid K-Cl Cotransporter Kcc1 Enhances Sickle Cell Disease Pathology in a Humanized Mouse Model. *Blood* **2015**, *126* (26), 2863–2870. https://doi.org/10.1182/blood-2014-10-609362.

(232) Shmukler, B. E.; Rivera, A.; Bhargava, P.; Nishimura, K.; Kim, E. H.; Hsu, A.; Wohlgemuth, J. G.; Morton, J.; Snyder, L. M.; De Franceschi, L.; Rust, M. B.; Hubner, C. A.; Brugnara, C.; Alper, S. L. Genetic Disruption of KCC Cotransporters in a Mouse Model of Thalassemia Intermedia. *Blood Cells. Mol. Dis.* **2020**, *81*, 102389. https://doi.org/10.1016/j.bcmd.2019.102389.

(233) Malha, L.; Mann, S. J. Loop Diuretics in the Treatment of Hypertension. *Curr. Hypertens. Rep.* **2016**, *18* (4), 27. https://doi.org/10.1007/s11906-016-0636-7.

(234) Sinha, A. D.; Agarwal, R. Thiazide Diuretics in Chronic Kidney Disease. *Curr. Hypertens. Rep.* **2015**, *17* (3), 13. https://doi.org/10.1007/s11906-014-0525-x.

(235) Ward, A.; Heel, R. C. Bumetanide. *Drugs* **1984**, *28* (5), 426–464. https://doi.org/10.2165/00003495-198428050-00003.

(236) Rybak, L. P. Ototoxicity of Loop Diuretics. *Otolaryngol. Clin. North Am.* **1993**, *26* (5), 829–844.

(237) Delpire, E.; Baranczak, A.; Waterson, A. G.; Kim, K.; Kett, N.; Morrison, R. D.; Daniels, J. S.; Weaver, C. D.; Lindsley, C. W. Further Optimization of the K-Cl Cotransporter KCC2 Antagonist ML077: Development of a Highly Selective and More Potent in Vitro Probe. *Bioorg. Med. Chem. Lett.* **2012**, *22* (14), 4532–4535. https://doi.org/10.1016/j.bmcl.2012.05.126.

(238) Eswar, N.; Webb, B.; Marti-Renom, M. A.; Madhusudhan, M. S.; Eramian, D.; Shen, M.; Pieper, U.; Sali, A. Comparative Protein Structure Modeling Using Modeller. *Curr. Protoc. Bioinforma. Ed. Board Andreas Baxevanis Al* **2006**, *0 5*, Unit-5.6. https://doi.org/10.1002/0471250953.bi0506s15.

(239) Olsson, M. H. M.; Søndergaard, C. R.; Rostkowski, M.; Jensen, J. H. PROPKA3: Consistent Treatment of Internal and Surface Residues in Empirical p K_a Predictions. *J. Chem. Theory Comput.* **2011**, *7* (2), 525–537. https://doi.org/10.1021/ct100578z.

(240) Schott-Verdugo, S.; Gohlke, H. PACKMOL-Memgen: A Simple-To-Use, Generalized Workflow for Membrane-Protein–Lipid-Bilayer System Building. *J. Chem. Inf. Model.* **2019**, *59* (6), 2522–2528. https://doi.org/10.1021/acs.jcim.9b00269.

(241) Le Grand, S.; Götz, A. W.; Walker, R. C. SPFP: Speed without Compromise—A Mixed Precision Model for GPU Accelerated Molecular Dynamics Simulations. *Comput. Phys. Commun.* **2013**, *184* (2), 374–380. https://doi.org/10.1016/j.cpc.2012.09.022.

(242) Salomon-Ferrer, R.; Case, D. A.; Walker, R. C. An Overview of the Amber Biomolecular Simulation Package: Amber Biomolecular Simulation Package. *Wiley Interdiscip. Rev. Comput. Mol. Sci.* **2013**, *3* (2), 198–210. https://doi.org/10.1002/wcms.1121.

(243) Maier, J. A.; Martinez, C.; Kasavajhala, K.; Wickstrom, L.; Hauser, K. E.; Simmerling, C. ff14SB: Improving the Accuracy of Protein Side Chain and Backbone Parameters from ff99SB. *J. Chem. Theory Comput.* **2015**, *11* (8), 3696–3713. https://doi.org/10.1021/acs.jctc.5b00255.

(244) Dickson, C. J.; Madej, B. D.; Skjevik, Å. A.; Betz, R. M.; Teigen, K.; Gould, I. R.; Walker, R. C. Lipid14: The Amber Lipid Force Field. *J. Chem. Theory Comput.* **2014**, *10* (2), 865–879. https://doi.org/10.1021/ct4010307.

(245) Joung, I. S.; Cheatham, T. E. Determination of Alkali and Halide Monovalent Ion Parameters for Use in Explicitly Solvated Biomolecular Simulations. *J. Phys. Chem. B* **2008**, *112* (30), 9020–9041. https://doi.org/10.1021/jp8001614.
(246) Darden, T.; York, D.; Pedersen, L. Particle Mesh Ewald: An *N* ·log(*N*) Method for Ewald Sums in Large Systems. *J. Chem. Phys.* **1993**, *98* (12), 10089–10092. https://doi.org/10.1063/1.464397.
(247) Rodriguez, A.; Laio, A. Clustering by Fast Search and Find of Density Peaks. *Science* **2014**, *344* (6191), 1492–1496. https://doi.org/10.1126/science.1242072.
(248) Smart, O. S.; Neduvelil, J. G.; Wang, X.; Wallace, B. A.; Sansom, M. S. P. HOLE: A Program for the Analysis of the Pore Dimensions of Ion Channel Structural Models. *J. Mol. Graph.* **1996**, *14* (6), 354–360. https://doi.org/10.1016/S0263-7855(97)00009-X.
(249) Ruiz Munevar, M. J.; Rizzi, V.; Portioli, C.; Vidossich, P.; Cao, E.; Parrinello, M.; Cancedda, L.; De Vivo, M. Cation Chloride Cotransporter NKCC1 Operates through a Rocking-Bundle Mechanism. *J. Am. Chem. Soc.* **2024**, *146* (1), 552–566. https://doi.org/10.1021/jacs.3c10258.
(250) Ben-Ari, Y. NKCC1 Chloride Importer Antagonists Attenuate Many Neurological and Psychiatric Disorders. *Trends Neurosci.* **2017**, *40* (9), 536–554. https://doi.org/10.1016/j.tins.2017.07.001.
(251) Delpire, E.; Gagnon, K. B. Elusive Role of the Na-K-2Cl Cotransporter in the Choroid Plexus. *Am. J. Physiol.-Cell Physiol.* **2019**, *316* (4), C522–C524. https://doi.org/10.1152/ajpcell.00490.2018.
(252) Pressey, J. C.; de Saint-Rome, M.; Raveendran, V. A.; Woodin, M. A. Chloride Transporters Controlling Neuronal Excitability. *Physiol. Rev.* **2023**, *103* (2), 1095–1135. https://doi.org/10.1152/physrev.00025.2021.
(253) Moseng, M. A.; Su, C.-C.; Rios, K.; Cui, M.; Lyu, M.; Glaza, P.; Klenotic, P. A.; Delpire, E.; Yu, E. W. Inhibition Mechanism of NKCC1 Involves the Carboxyl Terminus and Long-Range Conformational Coupling. *Sci. Adv.* **2022**, *8* (43), eabq0952. https://doi.org/10.1126/sciadv.abq0952.
(254) Zhao, Y.; Cao, E. Structural Pharmacology of Cation-Chloride Cotransporters. *Membranes* **2022**, *12* (12), 1206. https://doi.org/10.3390/membranes12121206.
(255) del Alamo, D.; Meiler, J.; Mchaourab, H. S. Principles of Alternating Access in LeuT-Fold Transporters: Commonalities and Divergences. *J. Mol. Biol.* **2022**, *434* (19), 167746. https://doi.org/10.1016/j.jmb.2022.167746.
(256) Bonati, L.; Rizzi, V.; Parrinello, M. Data-Driven Collective Variables for Enhanced Sampling. *J. Phys. Chem. Lett.* **2020**, *11* (8), 2998–3004. https://doi.org/10.1021/acs.jpclett.0c00535.
(257) Forrest, L. R.; Rudnick, G. The Rocking Bundle: A Mechanism for Ion-Coupled Solute Flux by Symmetrical Transporters. *Physiology* **2009**, *24* (6), 377–386. https://doi.org/10.1152/physiol.00030.2009.
(258) Masrati, G.; Mondal, R.; Rimon, A.; Kessel, A.; Padan, E.; Lindahl, E.; Ben-Tal, N. An Angular Motion of a Conserved Four-Helix Bundle Facilitates Alternating Access Transport in the TtNapA and EcNhaA Transporters. *Proc. Natl. Acad. Sci.* **2020**, *117* (50), 31850–31860. https://doi.org/10.1073/pnas.2002710117.
(259) Borgogno, M.; Savardi, A.; Manigrasso, J.; Turci, A.; Portioli, C.; Ottonello, G.; Bertozzi, S. M.; Armirotti, A.; Contestabile, A.; Cancedda, L.; De Vivo, M. Design, Synthesis, *In Vitro* and *In Vivo* Characterization of Selective NKCC1 Inhibitors for the Treatment of Core Symptoms in Down Syndrome. *J. Med. Chem.* **2021**, *64* (14), 10203–10229. https://doi.org/10.1021/acs.jmedchem.1c00603.
(260) Savardi, A.; Patricelli Malizia, A.; De Vivo, M.; Cancedda, L.; Borgogno, M. Preclinical Development of the Na-K-2Cl Co-Transporter-1 (NKCC1) Inhibitor ARN23746 for the Treatment of Neurodevelopmental Disorders. *ACS Pharmacol. Transl. Sci.* **2023**, *6* (1), 1–11. https://doi.org/10.1021/acsptsci.2c00197.

(261) Chew, T. A.; Zhang, J.; Feng, L. High-Resolution Views and Transport Mechanisms of the NKCC1 and KCC Transporters. *J. Mol. Biol.* **2021**, *433* (16), 167056. https://doi.org/10.1016/j.jmb.2021.167056.
(262) Delpire, E.; Gagnon, K. B. Na^+-K^+-$2Cl^-$ Cotransporter (NKCC) Physiological Function in Nonpolarized Cells and Transporting Epithelia. In *Comprehensive Physiology*; Terjung, R., Ed.; Wiley, 2018; pp 871–901. https://doi.org/10.1002/cphy.c170018.
(263) Hamann, S.; Herrera-Perez, J. J.; Zeuthen, T.; Alvarez-Leefmans, F. J. Cotransport of Water by the Na^+-K^+-$2Cl^-$ Cotransporter NKCC1 in Mammalian Epithelial Cells: Cotransport of Water by NKCC1. *J. Physiol.* **2010**, *588* (21), 4089–4101. https://doi.org/10.1113/jphysiol.2010.194738.
(264) Zeuthen, T.; MacAulay, N. Cotransport of Water by Na^+-K^+-$2Cl^-$ Cotransporters Expressed in *Xenopus* Oocytes: NKCC1 *versus* NKCC2: Water Transport in NKCC. *J. Physiol.* **2012**, *590* (5), 1139–1154. https://doi.org/10.1113/jphysiol.2011.226316.
(265) Sadegh, C.; Xu, H.; Sutin, J.; Fatou, B.; Gupta, S.; Pragana, A.; Taylor, M.; Kalugin, P. N.; Zawadzki, M. E.; Alturkistani, O.; Shipley, F. B.; Dani, N.; Fame, R. M.; Wurie, Z.; Talati, P.; Schleicher, R. L.; Klein, E. M.; Zhang, Y.; Holtzman, M. J.; Moore, C. I.; Lin, P.-Y.; Patel, A. B.; Warf, B. C.; Kimberly, W. T.; Steen, H.; Andermann, M. L.; Lehtinen, M. K. Choroid Plexus-Targeted NKCC1 Overexpression to Treat Post-Hemorrhagic Hydrocephalus. *Neuron* **2023**, *111* (10), 1591-1608.e4. https://doi.org/10.1016/j.neuron.2023.02.020.
(266) Li, J.; Shaikh, S. A.; Enkavi, G.; Wen, P.-C.; Huang, Z.; Tajkhorshid, E. Transient Formation of Water-Conducting States in Membrane Transporters. *Proc. Natl. Acad. Sci.* **2013**, *110* (19), 7696–7701. https://doi.org/10.1073/pnas.1218986110.
(267) Okazaki, K.; Wöhlert, D.; Warnau, J.; Jung, H.; Yildiz, Ö.; Kühlbrandt, W.; Hummer, G. Mechanism of the Electroneutral Sodium/Proton Antiporter PaNhaP from Transition-Path Shooting. *Nat. Commun.* **2019**, *10* (1), 1742. https://doi.org/10.1038/s41467-019-09739-0.
(268) Monette, M. Y.; Somasekharan, S.; Forbush, B. Molecular Motions Involved in Na-K-Cl Cotransporter-Mediated Ion Transport and Transporter Activation Revealed by Internal Cross-Linking between Transmembrane Domains 10 and 11/12. *J. Biol. Chem.* **2014**, *289* (11), 7569–7579. https://doi.org/10.1074/jbc.M113.542258.
(269) Janoš, P.; Magistrato, A. All-Atom Simulations Uncover the Molecular Terms of the NKCC1 Transport Mechanism. *J. Chem. Inf. Model.* **2021**, *61* (7), 3649–3658. https://doi.org/10.1021/acs.jcim.1c00551.
(270) Jorgensen, W. L.; Chandrasekhar, J.; Madura, J. D.; Impey, R. W.; Klein, M. L. Comparison of Simple Potential Functions for Simulating Liquid Water. *J. Chem. Phys.* **1983**, *79* (2), 926–935. https://doi.org/10.1063/1.445869.
(271) Ansari, N.; Rizzi, V.; Parrinello, M. Water Regulates the Residence Time of Benzamidine in Trypsin. *Nat. Commun.* **2022**, *13* (1), 5438. https://doi.org/10.1038/s41467-022-33104-3.
(272) Rizzi, V.; Bonati, L.; Ansari, N.; Parrinello, M. The Role of Water in Host-Guest Interaction. *Nat. Commun.* **2021**, *12* (1), 93. https://doi.org/10.1038/s41467-020-20310-0.
(273) Tribello, G. A.; Bonomi, M.; Branduardi, D.; Camilloni, C.; Bussi, G. PLUMED 2: New Feathers for an Old Bird. *Comput. Phys. Commun.* **2014**, *185* (2), 604–613. https://doi.org/10.1016/j.cpc.2013.09.018.
(274) Michaud-Agrawal, N.; Denning, E. J.; Woolf, T. B.; Beckstein, O. MDAnalysis: A Toolkit for the Analysis of Molecular Dynamics Simulations. *J. Comput. Chem.* **2011**, *32* (10), 2319–2327. https://doi.org/10.1002/jcc.21787.